



AFRL-RX-WP-TR-2013-0023

BIOTRONICS

**James G. Grote, Perry P. Yaney and Fahima Ouchen
AFRL/RXAS**

**Emily M. Heckman and Carrie M. Bartsch
AFRL/RYDP**

**Guru Subramanyam
AFRL/RYDD**

**Joshua A. Hagen
711 HPW/RHXBC**

**NOVEMBER 2012
Final Report**

Approved for public release; distribution unlimited.

See additional restrictions described on inside pages.

STINFO COPY

**AIR FORCE RESEARCH LABORATORY
MATERIALS AND MANUFACTURING DIRECTORATE
WRIGHT-PATTERSON AIR FORCE BASE, OH 45433-7750
AIR FORCE MATERIEL COMMAND
UNITED STATES AIR FORCE**

NOTICE AND SIGNATURE PAGE

Using Government drawings, specifications, or other data included in this document for any purpose other than Government procurement does not in any way obligate the U.S. Government. The fact that the Government formulated or supplied the drawings, specifications, or other data does not license the holder or any other person or corporation; or convey any rights or permission to manufacture, use, or sell any patented invention that may relate to them.

This report was cleared for public release by the USAF 88th Air Base Wing (88 ABW) Public Affairs Office (PAO) and is available to the general public, including foreign nationals. Copies may be obtained from the Defense Technical Information Center (DTIC) (<http://www.dtic.mil>).

AFRL-RX-WP-TR-2013-0023 HAS BEEN REVIEWED AND IS APPROVED FOR PUBLICATION IN ACCORDANCE WITH THE ASSIGNED DISTRIBUTION STATEMENT.

//signature//
JAMES G. GROTE
Soft Matter Materials Branch

//signature//
KATIE E. THORP, Chief
Soft Matter Materials Branch
Functional Materials Division

//signature//
KAREN R. OLSON, Deputy Chief
Functional Materials Division
Materials & Manufacturing Directorate

This report is published in the interest of scientific and technical information exchange, and its publication does not constitute the Government's approval or disapproval of its ideas or findings.

REPORT DOCUMENTATION PAGE				Form Approved OMB No. 0704-0188	
<p>The public reporting burden for this collection of information is estimated to average 1 hour per response, including the time for reviewing instructions, searching existing data sources, gathering and maintaining the data needed, and completing and reviewing the collection of information. Send comments regarding this burden estimate or any other aspect of this collection of information, including suggestions for reducing this burden, to Department of Defense, Washington Headquarters Services, Directorate for Information Operations and Reports (0704-0188), 1215 Jefferson Davis Highway, Suite 1204, Arlington, VA 22202-4302. Respondents should be aware that notwithstanding any other provision of law, no person shall be subject to any penalty for failing to comply with a collection of information if it does not display a currently valid OMB control number. PLEASE DO NOT RETURN YOUR FORM TO THE ABOVE ADDRESS.</p>					
1. REPORT DATE (DD-MM-YY) November 2012		2. REPORT TYPE Final		3. DATES COVERED (From - To) 1 September 2010 – 31 October 2012	
4. TITLE AND SUBTITLE BIOTRONICS				5a. CONTRACT NUMBER In-House	
				5b. GRANT NUMBER	
				5c. PROGRAM ELEMENT NUMBER 62102F	
6. AUTHOR(S) James G. Grote, Perry P. Yaney, and Fahima Ouchen (AFRL/RXAS) Emily M. Heckman and Carrie M. Bartsch (AFRL/RYPD) Guru Subramanyam (AFRL/RYPD) Joshua A. Hagen (711 HPW/RHXBC)				5d. PROJECT NUMBER 4348	
				5e. TASK NUMBER 00	
				5f. WORK UNIT NUMBER X0B5 (PS119100)	
7. PERFORMING ORGANIZATION NAME(S) AND ADDRESS(ES) AFRL/RXAS 3005 Hobson Way Wright-Patterson AFB, OH 45433				8. PERFORMING ORGANIZATION REPORT NUMBER	
9. SPONSORING/MONITORING AGENCY NAME(S) AND ADDRESS(ES) Air Force Research Laboratory Materials and Manufacturing Directorate Wright-Patterson Air Force Base, OH 45433-7750 Air Force Materiel Command United States Air Force				10. SPONSORING/MONITORING AGENCY ACRONYM(S) AFRL/RX	
				11. SPONSORING/MONITORING AGENCY REPORT NUMBER(S) AFRL-RX-WP-TR-2013-0023	
12. DISTRIBUTION/AVAILABILITY STATEMENT Approved for public release; distribution unlimited.					
13. SUPPLEMENTARY NOTES Approved by 88ABW Public Affairs Office: Case number 88ABW-2013-0337 on 24 January 2013. Report contains color.					
14. ABSTRACT This in-house effort processed deoxyribonucleic acid (DNA) and silk based bio polymer materials, aptamers and peptides into suitable electronic, photonic and chem/bio sensor materials. Blended nonlinear, metal, semiconductor, polymer, aptamer and peptide guests with biopolymers to enhance material properties taking advantage of self assembly/orientation and unique electromagnetic and optical properties. Fabricated and characterized test devices.					
15. SUBJECT TERMS Deoxyribonucleic Acid (DNA), Polymer Materials, Aptamers, Peptides, Electronic, Photonic, Nonlinear, Semiconductor					
16. SECURITY CLASSIFICATION OF:			17. LIMITATION OF ABSTRACT: SAR	18. NUMBER OF PAGES 105	19a. NAME OF RESPONSIBLE PERSON (Monitor) James G. Grote 19b. TELEPHONE NUMBER (Include Area Code) (937) 255-9776
a. REPORT Unclassified	b. ABSTRACT Unclassified	c. THIS PAGE Unclassified			

REPORT DOCUMENTATION PAGE Cont'd

7. PERFORMING ORGANIZATION NAME(S) AND ADDRESS(ES)

AFRL/RYP
2241 Avionics Circle
Wright-Patterson AFB, OH 45433

AFRL/RYP
2241 Avionics Circle
Wright-Patterson AFB, OH 45433

711 HPW/RHXBC
2947 Fifth Street, Bldg 840
Wright-Patterson AFB, OH 45433

TABLE OF CONTENTS

<u>Section</u>	<u>Page</u>
List of Figures	iii
List of Tables	vi
Introduction	1
1. DNA-SURFACTANT THIN FILM PROCESSING AND CHARACTERIZATION	5
1.1 INTRODUCTION.....	5
1.2 DNA PROCESSING	5
1.2.1 Molecular Weight	5
1.2.2 Precipitation with CTMA Surfactant	6
1.2.3 Preparation of DNA-CTMA Films	7
1.2.3.1 Noncrosslinked DNA-CTMA Films	7
1.2.3.2 Crosslinked DNA-CTMA Films	8
1.2.3.3 DNA-CTMA-Chromophore Films.....	9
1.2.3.4 DNA:PEDOT:CTMA.....	9
1.3 MATERIAL CHARACTERIZATION	10
1.3.1 DNA-CTMA Structure	10
1.3.2 Index of refraction.....	12
1.3.3 Optical loss.....	12
1.3.3.1 Absorption loss.....	12
1.3.3.2 Propagation loss	13
1.3.4 Thermal properties	14
1.4 RF ELECTRICAL CHARACTERIZATION	16
1.4.1 Capacitive Test Structure	16
1.4.1.1 Experimental Procedure	19
1.4.1.2 Results and Analysis	21
1.4.1.2.1 APC.....	21
1.4.1.2.2 DNA-CTMA.....	22
1.4.1.2.3 BST	25
1.4.1.3 Capacitance Measurements	26
1.4.2 Electric Force Microscopy	27
1.5 DC RESISTIVITY STUDIES.....	31
1.5.1. Introduction.....	31
1.5.2 Measurement Technique.....	31
1.5.3 Data Analysis	35
1.5.4. DATA	38

<u>Section</u>	<u>Page</u>
1.5.4.1 DNA compared to non-biopolymers	38
1.5.4.2 Silk.....	41
1.5.4.3 Effect of humidity and measurement accuracy	42
1.5.4.4 DNA with conductive dopants	44
1.5.4.5 Discussion	48
1.5.5 Summary	52
2. BIOPOLYMER-BASED BIO-ORGANIC DEVICES.....	54
2.1 ALL-DNA-BASED ELECTRO-OPTIC WAVEGUIDE MODULATOR.....	54
2.1.1 Fabrication	54
2.1.2 Electro-Optic Coefficient.....	55
2.1.3 Device testing and performance.....	57
2.1.4 Conclusions.....	60
2.2 FIELD EFFECT TRANSISTORS	60
2.2.1 Principles of Operation	60
2.2.2 Polymer FETs	61
2.2.3 DNA-biopolymer as the Semiconducting Layer.....	63
2.3 DEVELOPMENT OF A BIOLED: DNA AS AN ELECTRON BLOCKING LAYER IN ORGANIC LIGHT EMITTING DIODES	70
2.3.1 Materials Used for the Fabrication of BioLEDs	71
2.3.2 Fabrication of BioLEDs.....	74
2.3.3 Green (Alq3) Emitting BioLED Results.....	75
2.3.4 Comparison of DNA-CTMA to other Optoelectronic Polymers	79
2.3.5 Lifetime of BioLED and Baseline Devices	81
2.4 CONCLUSIONS	84
References	85
List of Abbreviations, Acronyms and Symbols.....	94

LIST OF FIGURES

Figure	Page
1 Molecular weight of DNA as a function of total sonication energy.....	6
2 CD spectra of DNA in water and DNA-CTMA in butanol at room temperature	10
3 Melting curves of DNA in water and complexed DNA-CTMA in butanol.	11
4 Index of refraction with Cauchy fit of DNA-CTMA for three different molecular weights.....	12
5 Absorption loss spectrum of a 356 μm thick film of noncrosslinked DNA-CTMA.....	13
6 TGA curves for DNA specimens.	15
7 DSC curves for DNA specimens The DNA-CTMA powder has a T_g of 148.17°C; however, a clear T_g could not be detected for the other materials.	15
8 A three dimensional representation of the capacitive test structure, showing the overlap of the signal conductor in the top-metal and the shunt line in the bottom metal which form the test capacitor.	17
9 A photograph of a capacitive test structure with the CPW probes in place to make microwave measurements.....	17
10 The electrical model for the capacitive test structure.	18
11 The microwave probe station pictured with the right probe on a capacitive test structure containing BSA-PVA and the left probe hovering above the sample.	20
12 An example of the AWR Microwave Office screen while matching circuit parameters with the measured S parameters.	21
13 The frequency response of S21 for a capacitive test structure of APC.	22
14 The frequency response of S21 for a capacitive test structure containing DNA-CTMA at room temperature for various applied biases from 0 to 20 V	23
15 The calculated relative dielectric constant as a function of applied voltage for DNA-CTMA using the measured S parameters from a capacitive test structure	24
16 The frequency response of S21 for a capacitive test structure containing DNA-CTMA at 100°C for various applied biases from 0 to 20 V.....	25
17 The frequency response of S21 for a capacitive test structure containing BST for applied biases from 0 to 3 V.	26
18 Capacitance as a function of frequency on a log scale for one capacitive test structure made with a DNA-CTMA thin film.	27
19 Tapping Mode Topography (left), Electric Force Microscopy (center) and Phase Images (right) with DC biases of (a) 5.5 V and (b) 6.0 V applied to the AFM tip.	29
20 Tapping Mode Topography (left), Electric Force Microscopy (center) and Phase Images (right) with DC biases of (a) 6.5 V, (b) 7.0 V and (c) 7.5 V applied to the AFM tip.	30

Figure	Page
21 Electrode patterns of 12 and 5 mm dia., and the schematic of the circuit used for volume resistivity measurements.	32
22 (a) Equivalent circuit for resistivity measurement, where V is the applied alternating potential, i_R is the dc leakage current due to the volume resistance R of the polymer specimen, i_C is the charging/discharging current through C with time constant $\tau_C = R_C C$ of the electrode- polymer- electrode sandwich connected to the measuring circuit and i_b is the polymer “background” current (b) Typical alternating polarity (± 5 V) data taken on a 3.52 μm -thick, cross-linked, water-insoluble DNA polymer film at 100°C.	33
23 Illustration of the corner temperature, T_c , using the APC data from Figure 24.	37
24 Resistivities of DNA-based films and selected non-DNA polymer films.	39
25 Resistivity of DNA (200kDa)-CTMA from continuously sonicated DNA in comparison to normal pulsed sonication.	41
26 Resistivities of silk films compared to DNA (300kDa)-CTMA.	42
27 As-received DNA with Na^+ counter ion and as-received DNA with CTMA^+ replacing the Na^+	43
28 Effect of long-term exposure to humidity and inadequate drying on the resistivity of a DNA-CTMA film.	44
29 Behavior of DNA (200kDa) complexed with dopant PCBM before adding CTMA in comparison to DNA(200kDa)-CTMA from Figure 24.	45
30 Behavior of DNA (500kDa) complexed with dopant BAYTRON P (from HCStarck-CLEVIOS) before adding CTMA in comparison to DNA (500kDa)-CTMA from Figure 24.	46
31 Behavior of DNA(300kDa) complexed with ammonium tetrachloroplatinate dopant before adding CTMA after curing at two temperatures in comparison to the fitted curve for the DNA(300kDa)-CTMA data in Figure 24.	47
32 Behavior of as-received DNA with dopant BAYTRON FE (from HCStarck-CLEVIOS).	48
33 Dependence of the dc conductivities of DNA (sonicated)-CTMA at 20°C on the inverse of the mean molecular weights.	51
34 Schematic of 3-layer DNA-based waveguide modulator.	55
35 Schematic of testing configuration for transverse EO polymer phase modulator.	58
36 Two beams propagating through three-layer poled DNA-based waveguide.	58
37 DC modulation of an all-DNA-based EO modulator, extended view.	59
38 Oscilloscope screen showing ac modulation of all-DNA-based EO modulator	60
39 The probe station setup used for measuring the DNA-based transistors.	64
40 A cross-section of the bottom gate BioFET structure.	65

<u>Figure</u>	<u>Page</u>
41 (a) Drain current as a function of drain voltage as measured on a bottom gate BioFET on a silicon wafer with a very thin silicon dioxide layer as the gate insulator. (b) Gate, drain and source current is plotted as a function of drain voltage for this device, verifying that the gate current is substantially lower than either the source or drain currents.	66
42 Saturation mobility as a function of drain voltage as calculated from the drain current vs. drain voltage data on a bottom gate BioFET with a very thin layer of native silicon dioxide as the gate insulator.	68
43 Output characteristics of DNA:PEDOT:CTMA based blends	69
44 Output characteristics of FETs using P3HT as a semiconducting film	70
45 Energy level diagram of fluorescent type OLED with HTLs.....	71
46 Energy level diagram of fluorescent type OLED with HTLs and HBL.....	72
47 Energy level diagram of OLED with HTLs, HBL and ETL	73
48 Energy level diagram of Alq3 emitting BioLED	73
49 Photograph of finished device	75
50 Luminance Current Voltage characteristics for green emitting Baseline device.....	76
51 Luminance Current Voltage characteristics for green emitting BioLED device.....	76
52 Luminance versus current density for BioLED and Baseline devices	77
53 Photographs of green emitting fluorescent type BioLED and Baseline devices in operation.....	78
54 Efficiency versus voltage for green emitting fluorescent type BioLED and Baseline devices	79
55 Current density vs. voltage in green Alq3 LEDs: baseline device, DNA EBL, PVK EBL, PMMA EBL. Inset shows a simple equivalent circuit for the DNA EBL device.	80
56 Luminous efficiency vs. luminance in Alq3 EL devices: baseline device, DNA EBL, PVK EBL, PMMA EBL.	80
57 Lifetime curves for Baseline green device: luminance and current density.....	81
58 Lifetime curves for BioLED green device: luminance and current density	82
59 Lifetime efficiency curves: BioLED and Baseline.....	82
60 a) Energy level diagram of Iridium complexed emitting BioLED; Photographs of b) Green emitting phosphorescent type BioLED and c) Green emitting inorganic LED in operation	84

LIST OF TABLES

<u>Table</u>	<u>Page</u>
1 Film thickness of spin-coated DNA-CTMA films at 800 rpm for 10s.	8
2 Waveguide loss for varying concentrations of PPIF crosslinker in DNA-CTMA films.	14
3 Parameters obtained from fitting Equation 13 to the conductivity data of the measurements given in Figure 24 plus silk in Figure 26. ^a	40
4 Refractive indices of various DNA-CTMA (DC) core and cladding materials.....	55
5 Summary of poling results for single-layer DNA-based films.	57

Introduction

Results of the research performed during the Biotronics In-House effort confirm the success and potential of Biotronics technology for optics, electronics and electro-optics applications. Biopolymers based on deoxyribonucleic acid (DNA) and silk, formulated over the last three years, have demonstrated unique optical and electromagnetic properties that no other known polymer possesses. In addition to its unique electromagnetic and optical properties, DNA possesses a self assembly property and an “ordered” type nature which have been used to enhance the properties of several material complexes and electronic and photonic devices.

Low optical absorption, propagation and scattering loss, a large band gap and low electrical resistivity were achieved, simultaneously. We also discovered that the electrical resistivity could be reduced by as much as two orders of magnitude by simply reducing the molecular weight, without increasing the optical losses.

Using a lower molecular weight DNA-based biopolymer as the top and bottom cladding layers in an NLO polymer EO modulator, we were able to demonstrate a 90% poling efficiency and a 3X decrease in the optical insertion loss of the device, from 15 dB to 10 dB ⁽³⁾. Since that first application, these new biopolymer-based materials have been used for many types of electronic and photonic applications.

Even with growing research in biopolymers and the achievements presented in this report, there is still much about biopolymers that we do not know. Use of DNA and silk-based biopolymers in such devices as organic light emitting diodes and organic field effect transistors, has resulted in significant improvements in device performance, all with un-optimized materials. In order to improve and optimize the performance of these types of devices we must first optimize the properties of the material.

We know through the literature, and by experimentation, that reducing the molecular weight of the DNA reduces the electrical resistivity, however, we are not certain why that is. As the DNA is sonicated, the overall molecular weight is reduced. Since the adenine-thymine (A-T) bond is weaker than the guanine-cytosine (G-C) bond, the DNA will typically break at the A-T bond during sonication, thus increasing the G-C to A-T content. Increased G-C to A-T content in dry double stranded DNA of the same length has been reported to have lower electrical resistivity ⁽⁶⁾. In addition, the lengths of the DNA base pairs are also reduced during sonication, which has been also suggested to reduce the electrical resistivity. In addition, with shorter DNA lengths we have the potential for more DNA strands to be in parallel with the applied electric field, which could also be a reason for the reduced electrical resistivity. So, is the decrease in electrical resistivity due to the shorter length, increased G-C to A-T content, more DNA stands in parallel with the electric field, or a combination of all three? When the DNA is sonicated we end up with many different base pair lengths, or molecular weights, but with the majority being near a certain molecular weight. There is still some low and high molecular weight DNAs. A way to better control the base pair lengths would be to use enzymes, however the yields are low and the costs are high. We have been somewhat successful using polyethylene glycol (PEG) to reduce the distribution of the base pairs by reducing the high and low molecular weight DNA, however, the yield is low for this method as well. So we have not yet been able to determine the effect molecular weight has with device performance, other than reduced electrical resistivity.

It has been shown that adding the hexadecyltrimethyl ammonium chloride (CTMA) surfactant to the DNA, to render it water insoluble, increases the electrical resistivity by several orders of magnitude. Since CTMA is a long molecule, the DNA strands would be further apart. Since charge flow between DNA molecules, as well as through them, has been reported⁽¹⁷⁾, could the electrical resistivity be reduced by decreasing the distance between DNA base pairs?

The DNA used in this study has a reduced protein content totaling around 2%. Is that low enough? What effect do proteins have on device performance? Sonicating the DNA produces numerous sequences of DNA all blended together. What role does sequence play and could particular sequences be identified that would be best for particular applications?

We have begun investigation plasmid-DNA. Since it can be produced in large quantities having one molecular weight, no proteins attached and specific genomic sequences, it may hold the answers we are looking for, as well as help solve forthcoming production, yield and cost issues.

Some other properties of DNA, DNA-CTMA and silk we have measured include high optical damage threshold, high photochemical stability.

We measured the thermal conductivity of both DNA and DNA-CTMA and compared it with the thermal conductivity of polymethylmethacrylate (PMMA). The thermal conductivity of DNA and DNA-CTMA measured 0.82 W/mK and 0.6 W/mK, respectively. Compared with the thermal conductivity of PMMA, 0.12 W/mK, reported in the literature⁽¹¹⁾, we find that the thermal conductivity of DNA is 7X higher than the thermal conductivity of PMMA and the thermal conductivity of DNA-CTMA is 5 times higher. This suggests that if DNA is introduced into the device, the potential exists for removing heat from the device more efficiently than using other polymer materials.

We measured the optical damage threshold of DNA and silk using ultrafast Z-Scan at $\lambda = 750$ nm. We found the optical damage threshold for DNA-CTMA and silk to be ~ 2.5 J/cm² and ~ 5 J/cm², respectively. This is comparable to the 2.7-4.0 J/cm² that we measured for fused silica.

The photochemical stability was measured by Rau's group at the Universitatea POLITEHNICA din Bucuresti, working with our group. We found that the kinetic degradation constant for both DNA and DNA-CTMA measured $2.78 \times 10^{-6}/\text{m}$ and $2.57 \times 10^{-6}/\text{m}$, respectively, at $\lambda = 312$ nm (UV), at room temperature. The kinetic degradation constant for polycarbonate measured $3.13 \times 10^{-6}/\text{m}$, under the same conditions, which is about 12% higher than the DNA and DNA-CTMA samples. At 85°C the kinetic degradation constant for DNA and DNA-CTMA measured $6.68 \times 10^{-6}/\text{m}$ and $36.6 \times 10^{-6}/\text{m}$, respectively, where the kinetic degradation constant for polycarbonate measured $11000 \times 10^{-6}/\text{m}$ or ~ 2000 times higher than DNA and ~ 200 times higher than DNA-CTMA. This indicates that DNA-based materials are more photochemically stable than other polymers, especially at elevated temperatures.

In collaboration with Prasad's group at the University at Buffalo, we demonstrated an enhancement in two photon lasing using DNA as a host, compared to other polymer hosts, due to the fact that we found DNA could be doped much more heavily without aggregation than the other polymer hosts⁽⁵⁾.

Jin's and Choi's group at Korea University used DNA as a host material to demonstrate a significant enhancement in the photoluminescence of both fluorescent and phosphorescent type guest materials for sensing and organic light emitting diode applications ^(13,2).

In collaboration with Sotzing's group at the University of Connecticut, we demonstrated nearly exact white, non-phosphor-based solid state lighting, blending donor and acceptor dyes with DNA-CTMA at a donor:acceptor ratio of 1:20 ⁽¹⁴⁾. Illuminating the DNA-CTMA-donor:acceptor complex at $\lambda = 365$ nm, we achieved a chromaticity of (0.35, 0.34). Exact white has a chromaticity of (0.33, 0.33). The donor dye was 4-[4-dimethylaminostyryl]-1-docosylpyridinium bromide and the acceptor dye was Coumarin 102. Comparing the DNA host with other polymer hosts we found that more energy is transferred from the donor to the acceptor when DNA is used and that the observed enhancement in the energy transfer efficiency between the donor and acceptor can be attributed to self assembly, the well defined organization of the dyes by association within the DNA. An actual device was also fabricated by electro-spinning the DNA-CTMA-donor:acceptor complex inside the lens of a 400 nm light emitting diode.

In collaboration with our group, Samoc's group at the Australian National University performed many refractive index studies of DNA and DNA-CTMA complexes. We measured a large second order nonlinearity associated with DNA and have observed a liquid crystalline like behavior ⁽¹⁶⁾.

In collaboration with Kajzar's group at the Université d'Angers, we demonstrated a four times increase in third order nonlinearity using a disperse red one-DNA complex, when compared with a polymethylmethacrylate polymer host ⁽¹²⁾. This increase is thought to be due, in part, to the highly polarizable conjugated π electrons in DNA and that, again, there appears to be a self assembly or alignment taking place in the DNA which is not present in amorphous polymers.

Our in-house group discovered yet another interesting property of DNA. We were able to achieve an 86% selectivity of (6,5) single walled carbon nanotubes (SWNTs) from a metallic and semiconducting mixture by sonicating a blend of the SWNT mixture with DNA ⁽⁸⁾. This compares to 50% selectivity using d(GT)₂₀, a synthetic oligo-DNA. High selectivity is important since it has been shown that one needs at least 86% selectivity of semiconducting SWNT's for high mobility transistors. Another plus to using DNA is that the selectivity of (6,5) SWNTs is \$1000 less per gram to process than using d(GT)₂₀. The patent for this discovery was recently awarded ⁽⁹⁾.

In addition to the 7x decrease in gate voltage achieved by our work in collaboration with Sariciftci's group at the Johannes Kepler University of Linz, using a DNA-based gate dielectric in a pentacene-based organic field effect transistor ⁽²⁰⁾, Jin's and Choi's group recently increased the transistors mobility by using a photoreactive DNA ⁽¹⁰⁾. In collaboration with Peyghambarian's group at the University of Arizona, we developed a DNA-sol-gel complex with enhanced dielectric properties potentially suitable for both capacitors and gate dielectrics ⁽¹⁵⁾. We have achieved a nearly 900 V/ μ m dielectric breakdown voltage with a dielectric constant of 7-8.

In order to use any new material, device fabrication processes also need to be taken into account. We have demonstrated that DNA films can be applied via spin deposition, casting, flow coating, ink jet printing, vapor deposition, spray deposition and pulsed laser deposition. Photoresist can be deposited without dissolving the DNA-based materials and these materials can be exposed to UV

and etched. We have also demonstrated that they can be ablated using an excimer laser and can be nano-imprinted. So, are we close to having DNA-based commercial products in the near future?

From the first point contact transistor, demonstrated by Brattain and Bardeen in 1947, to the p-n junction ⁽¹⁹⁾, to the announcement of the first commercially feasible silicon transistors in 1954 ⁽²²⁾, it took until the mid 1970's to actually realize commercial silicon devices (Teal 1976). Silicon had to be a nearly defect free crystalline material and ultra purified to 99.99999999% to become electronic grade ⁽⁴⁾. Diffusion and implantation techniques had to be developed. Optimum diffusion and implantation materials had to be identified. Photoresist and lithography technologies also had to be developed.

The silicon microelectronics we know today took the combined efforts of physics, engineering and metallurgy pioneers like Bardeen, Shockley, Teal, Ebers, Early, Ohl, Scaff, Theurer, Schumacher, Buehler, Sparks, Hall, Taylor, Noyce, Moore, Galvin and Kilby. It also took the commitments of companies like Bell, Texas Instruments, Motorola, Fairchild, RCA, General Electric, Sylvania, Raytheon, Westinghouse and later on Mostek, AMI and Intel. With decades of research and engineering, it has been an internationally driven endeavor.

Based on this past history for silicon, it would seem that we are probably at silicon's mid 1950's point of development with DNA. We may be able to shorten time a little by taking advantage of past work with silicon, organics and DNA, but there is still much more to be done and much more to learn before we can realize commercial devices. We need to maximize device performance through better understanding of material properties and the effects of protein content, molecular weight and genomic sequence. We need to investigate new sources of DNA such as plasmid-DNA and new guest materials or dopants. We need to better understand and optimize the binding processes for these guest materials. We need to better understand and optimize the alignment of DNA utilizing electrical, magnetic, mechanical and self alignment. We need to better understand and optimize the deposition and fabrication processes. All of the research and development that was needed to realize silicon-based microelectronics also applies to DNA.

As we, and other researchers from around the world, have demonstrated, biotechnology and DNA and silk-based biopolymers are not only applicable for genomic sequencing and clinical diagnosis and treatment, but can also have a major impact on non-biotech applications as well, such as electronics and photonics, opening up a whole new field for bioengineering. Where silicon has been the building block of inorganic electronics and photonics, DNA holds promise to become the building block for organic electronics and photonics.

Details of our research, including materials processing and characterization and device fabrication and testing, will be presented in this report.

1. DNA-SURFACTANT THIN FILM PROCESSING AND CHARACTERIZATION

1.1 INTRODUCTION

The use of biopolymer-based materials, such as deoxyribonucleic acid (DNA), in organic electronic and photonic devices is rapidly becoming an area of interest in the photonics community. Compared to conventional polymer materials, biopolymers, either naturally occurring or artificially produced, can provide additional degrees of freedom in device design and produce enhancements in device performance. This is due to their unique electronic and optical properties. Additionally, biopolymers derived from DNA are a renewable resource that is non-fossil fuel based and inherently biodegradable.

The DNA-surfactant biopolymer is one of the most studied biopolymers currently being used in photonic devices. However, the process required to transform raw, genomic DNA from a natural, biological source into an optical quality material is non-trivial. This chapter will focus on the processing that has been developed in the past several years to form the optical-quality DNA biopolymer from genomic salmon DNA, the various dopants integrated into the DNA biopolymer, and the relevant optical, electronic and material characterization of the biopolymer for electronic and photonic devices^(44, 43, 41, 40, 55, 53, 54, 50, 51, 52, 27, 30, 48, 65, 83, 82, 81).

1.2 DNA PROCESSING

The DNA used in this research was purified by the Chitose Institute of Science and Technology (CIST) in Hokkaido, Japan from salmon roe and milt sacs, waste products of the Japanese fishing industry, using an enzyme isolation process. The use of salmon spermatozoa as a rich source for DNA is not new; what is new is the ability to extract and purify the DNA on a scale of mass production⁽⁸⁸⁾. Although the exact purification details are proprietary, the general steps of the purification process are known as this process is simply a variation on time-proven DNA extraction techniques that have been in use for decades. The DNA received from CIST is reported to have a purity of ~96% with a protein content of ~2%.

1.2.1 Molecular Weight

The molecular weight of the DNA provided by CIST was measured to be greater than 8000 kDa using agarose gel electrophoresis⁽²⁴⁾. This high molecular weight DNA is difficult to process into an optical waveguide quality film due to its high viscosity in solution. In addition, it is necessary to reduce the molecular weight of the DNA to at least 1000 kDa to achieve an appreciable EO coefficient through electrode poling. To reduce the molecular weight, an ultrasonic processor is used^(52, 53). The Sonics & Materials ultrasonic processor model VC-750 with a 19-mm diameter high-gain solid probe can process up to 500 mL of solution and can reduce the mean molecular weight of the CIST DNA to as low as 200 kDa.

To begin with, two grams of DNA are dissolved in 500 mL of 14 MΩ·cm distilled/deionized water at room temperature. The DNA is then sonicated on ice in ten-second pulses with a twenty-second rest period between each pulse. Figure 1 shows the molecular weight as a function of total sonication energy. Sonication does not uniformly reduce the size of the DNA strands; rather it randomly breaks the DNA into a Gaussian-like distribution of molecular weights. The molecular weight reported is the mean of this distribution of molecular weights with a variation of approximately ± 50%. The molecular weight is measured using agarose gel electrophoresis with a 0.8% agarose gel. After sonication, the aqueous DNA solution is filtered through a nylon filter

with a 0.45 μm pore size to remove non-DNA particles (such as carbon black) created during sonication.

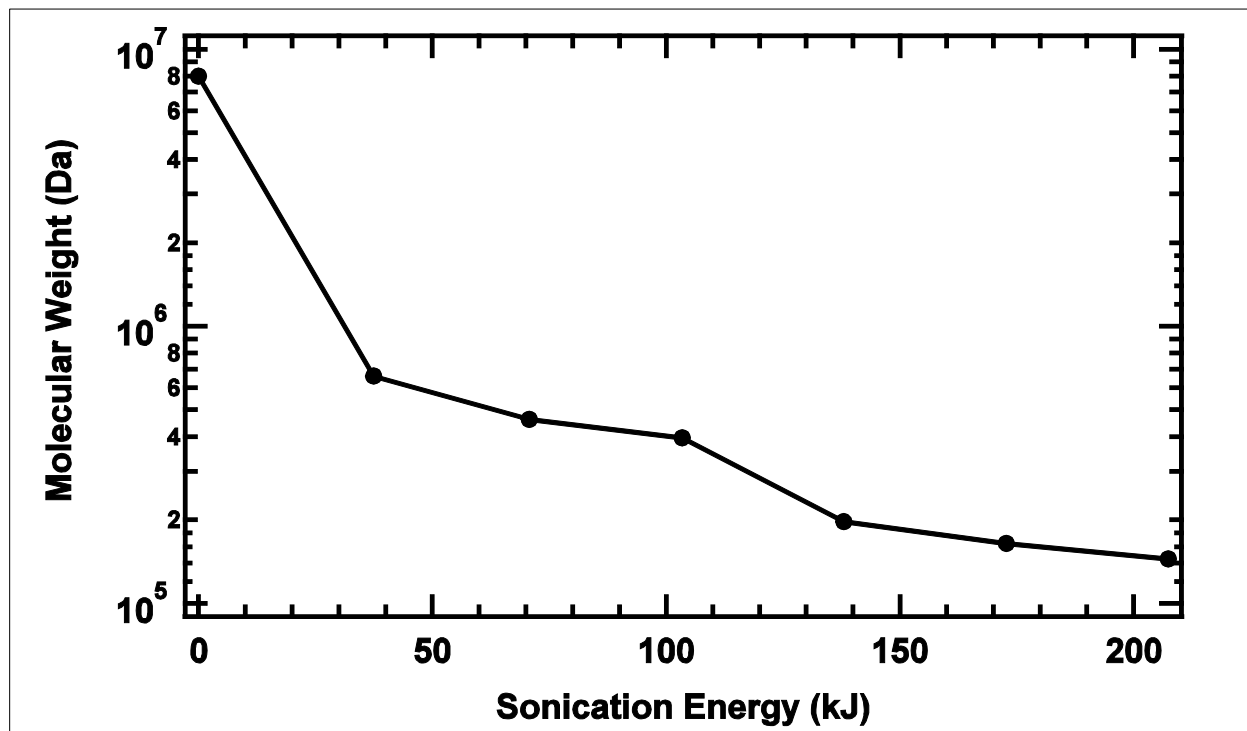


Figure 1. Molecular weight of DNA as a function of total sonication energy.

The DNA was sonicated on ice in 10-s-long pulses with a 20-s rest period between pulses to prevent overheating of the sample.

1.2.2 Precipitation with CTMA Surfactant

The DNA is initially soluble only in aqueous solutions and does not dissolve in any organic solvent. It is precipitated with the cationic surfactant complex hexadecyltrimethylammonium-chloride (CTMA) to make it water insoluble and to provide increased molecular stability^(89, 90). This is done through an ion exchange reaction. The CTMA surfactant was chosen over other surfactants for two reasons. First, the alkyl chain length of 16 for CTMA was ideal. Cationic surfactants with alkyl chains shorter than 16 might induce poor mechanical properties of the material while surfactants with longer alkyl chains are water insoluble (which complicates the precipitation process since it cannot be initially dissolved in water) and pose the risk of damaging the DNA double helical structure⁽⁸⁹⁾. Secondly, the CTMA surfactant was commercially available. It was obtained from Fisher Scientific and used without further purification.

To precipitate the DNA with the CTMA cationic surfactant, the DNA is first dissolved at room temperature in 14 M Ω ·cm distilled/deionized water at a ratio of 4 g/L using a magnetic stirrer. If necessary, the molecular weight of the DNA is reduced with the ultrasonic processor as previously described. An equal amount by weight of CTMA is likewise dissolved in 14 M Ω ·cm distilled/deionized water, also at a concentration of 4 g/L. Using equal amounts of DNA and CTMA by weight ensures that there is one CTMA molecule for each DNA base pair.

The DNA solution is added drop-wise to the CTMA solution with a burette. A white DNA-CTMA precipitate forms as the DNA is added to the CTMA. The solution is mixed for an additional four hours at room temperature. The precipitate is removed by filtering the solution using a TX 609 Technicloth low-lint clean-room paper as a filter. Using this type of filter allows for the precipitate to be periodically squeezed within the filter paper to remove any unprecipitated CTMA. It also provides a more complete rinsing of the DNA-CTMA precipitate. During the filtering process, an additional 3 to 4 L of 14 MΩ·cm distilled/deionized water are poured through the filter to rinse the precipitate and to ensure that any CTMA that did not bind to the DNA is thoroughly rinsed away. When the water running through the filter comes out clear and there is no evidence of surfactant bubbles, it is assumed that the precipitate has been thoroughly rinsed. The precipitate is then collected, placed in a Teflon beaker and dried in a vacuum oven overnight at 40°C. This excessive rinsing and periodic squeezing of the precipitate within the filter is essential to obtaining a pure DNA-CTMA sample with no unprecipitated CTMA mixed in. This method yields a white, powdery DNA-CTMA precipitate. Although squeezing the DNA-CTMA precipitate in the filter paper is the most effective way we have found to remove the excess CTMA, one drawback of this method is that filter fibers tend to stick to the precipitate. These fibers are removed by using a 0.2 μm syringe filter.

1.2.3 Preparation of DNA-CTMA Films

1.2.3.1 Noncrosslinked DNA-CTMA Films

The resulting DNA-CTMA compound is soluble in many of the alcohols including butanol, methanol, ethanol and isopropanol, as well as an alcohol-chloroform blend. To spin-coat a thin film for photonics applications, butanol is the solvent of choice because its slow evaporation due to a high boiling point (116 – 118°C) ensures a smooth, uniform film during the spin-coating process. Butanol has a density of 0.81 g/mL and was purchased from Sigma-Aldrich and used without further purification. The amount of solvent used in dissolving the DNA-CTMA is dependent on the molecular weight of the starting DNA. Higher molecular weight (>1000 kDa) DNA forms a more viscous solution than lower molecular weight (<500 kDa) DNA. A greater amount of solvent is, therefore, required for higher molecular weight DNA.

To make a thin film, DNA-CTMA is dissolved in butanol at a concentration appropriate for its molecular weight. The most common molecular weights used are 500 kDa and 200 kDa. For these lower molecular weights, a solution of 110 mM bp⁻¹ DNA-CTMA in butanol yields a film thickness of between 2 and 3 μm for spinning parameters of 800 rpm for 10 sec. The solution is mixed in a sealed glass bottle, in a 60°C oven, using an ATR Rotamix for six hours. Once completely dissolved, the solution is filtered through a 0.2 μm pore size syringe filter. Because DNA-CTMA solutions are more viscous at room temperature, the filtering takes place inside a 60°C oven using a New Era pump systems motorized syringe pump. The solution is left to sit overnight in a tightly capped container in the 60°C oven to allow any micro-bubbles induced by filtering to dissipate. It is then spin-coated on to a substrate at a speed of 800 – 1000 rpm for ten seconds with a five second ramp. After spinning, the sample is cured in an 80°C oven for one hour. Table provides examples of measured film thickness as a function of DNA molecular weight and DNA-CTMA concentration in solution. These data show that the film thickness is quite sensitive to the DNA-CTMA concentration for a given molecular weight and, as might be expected, higher concentrations are possible with the lower molecular weights.

Table 1. Film thickness of spin-coated DNA-CTMA films at 800 rpm for 10s.

Molecular weight of DNA (kDa) ^a	DNA-CTMA concentration in butanol (mM bp ⁻¹)	Film Thickness (μm) ^b
8000	54.2	5.0
8000	39.8	2.4
1300	61.6	3.0
1300	46.9	1.3
500	85.0	3.0
500	69.3	1.7
300	101.5	2.0
300	85.0	1.5
200	85.0	2.6

^a Estimated uncertainty $\pm 50\%$

^b Estimated uncertainty $\pm 0.1 \mu\text{m}$

1.2.3.2 Crosslinked DNA-CTMA Films

The noncrosslinked DNA-CTMA films, while of high optical quality, are soft and scratch easily (a visible mark is left on the film when scratched by a fingernail). This makes them incompatible with more aggressive processing techniques, such as sawing, that are often required to fabricate a photonic device. One solution to this problem is to crosslink the DNA-CTMA films. The crosslinker used in this work is poly(phenylisocyanate)-co-formaldehyde (PPIF) with a formula weight of 400 g/mol. It was purchased from Sigma-Aldrich and used without further purification. The resulting crosslinked DNA-CTMA films are significantly harder (the films show no mark when scratched by a fingernail) than the non-crosslinked films, allowing them to withstand more demanding fabrication procedures than non-crosslinked films due to their increased hardness. Crosslinked films are also resistant to a wider range of solvents, including butanol and other alcohols. This allows multi-layer DNA-based structures to be fabricated.

It was found through systematic study that the lowest amount of PPIF that can be used and still crosslink the DNA-CTMA film is 10 wt% (36.1 mol%) PPIF with respect to DNA-CTMA. However, concentrations of up to 20 wt% (81.2 mol%) can be used. Beyond 20 wt%, optical losses are too high for photonics applications ($>1 \text{ dB/cm}$). The addition of the crosslinker significantly increases the refractive index and this must be taken into consideration when choosing the amount of crosslinker to use.

To prepare a crosslinked DNA-CTMA film, the DNA-CTMA is dissolved in butanol at a concentration appropriate for its molecular weight. The PPIF crosslinker is dissolved in butanol at a ratio of 1:4, PPIF:Butanol by weight. The DNA-CTMA-butanol solution is mixed in a 60°C oven for at least six hours. The PPIF-butanol solution is not mixed using the Rotamix, but rather is left standing in the 60°C oven. After a few hours of standing in the oven, the PPIF is fully dissolved in the butanol. Once fully dissolved, the DNA-CTMA-butanol solution is added to the PPIF-butanol solution and the resulting solution is mixed for an additional two hours in the 60°C oven. The DNA-CTMA-PPIF solution is filtered through a 0.2 μm pore size syringe filter to remove any impurities and left to sit overnight in a 60°C oven to allow any micro-bubbles induced by filtering to dissipate. It is spin-coated onto a substrate using the same spin parameters as the non-crosslinked DNA-CTMA films. The substrates are baked in an 80°C oven for five minutes

and then cured in a vacuum oven at 175°C for 15 min. After curing, the crosslinked films are resistant to butanol.

1.2.3.3 DNA-CTMA-Chromophore Films

For the core waveguide layer, a chromophore dye DR1 is added to the DNA-CTMA-PPIF solution. DR1 has a formula weight of 314.34 g/mol and was purchased from Sigma-Aldrich and used without further purification. Both crosslinked and noncrosslinked DNA-CTMA-chromophore films were made. For the core layer, an amount between 5 wt% (21.8 mol%) and 10 wt% (45.9 mol%) DR1 with respect to DNA-CTMA was used. The dye was dissolved separately in dioxane at a concentration of 24.6 mM. Dioxane has a density of 1.034 g/mL and was purchased from Sigma-Aldrich and used without further purification. For the lower concentration of chromophore dye, the lower amount of PPIF, 10 wt%, is suitable to achieve crosslinking, however a longer curing time of 20 minutes at 175°C is required. For the higher concentration of chromophore dye, a higher amount of PPIF, 20 wt%, is required to achieve crosslinking.

To fabricate a DNA-CTMA-chromophore film, DNA-CTMA is dissolved in butanol as previously discussed and an appropriate amount of PPIF is dissolved separately in butanol at a concentration of 1:4, PPIF:Butanol by weight, by being allowed to stand in a 60°C oven for several hours. Once dissolved, the DNA-CTMA-butanol solution is added to the PPIF-butanol solution and mixed for an additional two hours. The chromophore dye is dissolved separately in dioxane at a concentration of 24.6 mM. The chromophore dye-dioxane solution is then added to the DNA-CTMA-PPIF solution and mixed for an additional hour. The solution is filtered through a 0.2 µm syringe filter and allowed to stand overnight. It is spin-coated and cured in a manner appropriate for the dye concentration as previously discussed.

1.2.3.4 DNA:PEDOT:CTMA

A processing technique similar to that used to create DNA-CTMA is used to obtain DNA:PEDOT:CTMA^(47, 29). This biopolymer is formed from the raw DNA obtained from CIST, poly(3,4-ethylenedioxythiophene) poly(styrenesulfonate) (PEDOT:PSS), and CTMA. The aqueous dispersion of PEDOT:PSS is commercially known as Baytron P. Two grams of DNA are dissolved in 500 mL of deionized water to produce a concentration of four grams per liter for sonication. This beaker of dissolved DNA is then placed into a bucket and the beaker is surrounded by ice to prevent overheating. Then a Sonics & Materials ultrasonic processor model VC-750 with a 19 mm diameter high gate solid probe is used in pulse mode for ten nine-minute cycles to reduce the molecular weight of the DNA from 6000 - 8000 kDa to an average molecular weight of about 300 kDa. Each pulse consists of sonicating for ten seconds and resting for twenty seconds. Each nine-minute sonication cycle releases around 20 kJ of energy into the dissolved DNA. After sonication is complete, the dissolved DNA is filtered through a 0.65 micron nylon filter. Baytron P is purified before titration by filtering through a 0.45 micron polytetrafluoroethylene (PTFE) syringe filter. Then, 17.0 grams are added dropwise to the dissolved DNA at a ratio of approximately 1:80 PEDOT molecules to DNA base pairs. This is equivalent to adding 36.0 wt% of PEDOT molecules into the DNA, or 89.9 wt% Baytron P into the DNA. The DNA:PEDOT solution is mixed with a magnetic stirrer at room temperature for four hours. An excess amount of CTMA is dissolved in deionized water. The CTMA solution is then slowly poured into the DNA:PEDOT solution, as it is being stirred, keeping the stream of CTMA solution as small as possible. This results in the DNA:PEDOT:CTMA complex. The

DNA:PEDOT:CTMA solution stirs for two hours, and afterwards the precipitate settles out of the water. Finally, the precipitate is thoroughly rinsed and dried overnight in a vacuum oven. This renders an organically soluble, semiconducting complex of DNA:PEDOT:CTMA.

1.3 MATERIAL CHARACTERIZATION

1.3.1 DNA-CTMA Structure

Circular dichroism (CD) and absorption measurements at 260 nm were used to determine if the double helical structure of DNA is preserved in the complexed DNA-CTMA material. CD measurements confirmed that a DNA-CTMA solution does retain its double helical structure at room temperature. Absorption measurements were used to determine the denaturation temperature.

The CD measurements were taken using a Jasco model J-720 spectropolarimeter. The DNA-CTMA is dissolved in butanol at a concentration of 26.0 mM. The absorption measurements are taken using a Cary 100 Bio UV-Visible Spectrophotometer. The liquid samples are placed into a quartz cuvette and the temperature is controlled with a Peltier device connected to Varian Bio-Melt software. The temperature is controlled by the software and is increased 5°C every two minutes, with a 30 s wait time at each temperature before each measurement. The sample concentrations were 50 µg/mL for aqueous DNA measurements and 34 mg/mL for DNA-CTMA in butanol.

A CD spectrum taken at room temperature of DNA-CTMA in butanol was shown to exhibit the same characteristics as a CD spectrum of aqueous DNA, although it is shifted slightly (Figure 2) (70, 79). This shift is most likely due to the addition of the CTMA molecules on the DNA chain. This spectrum implies that DNA-CTMA retains the double helical structure of DNA at room temperature.

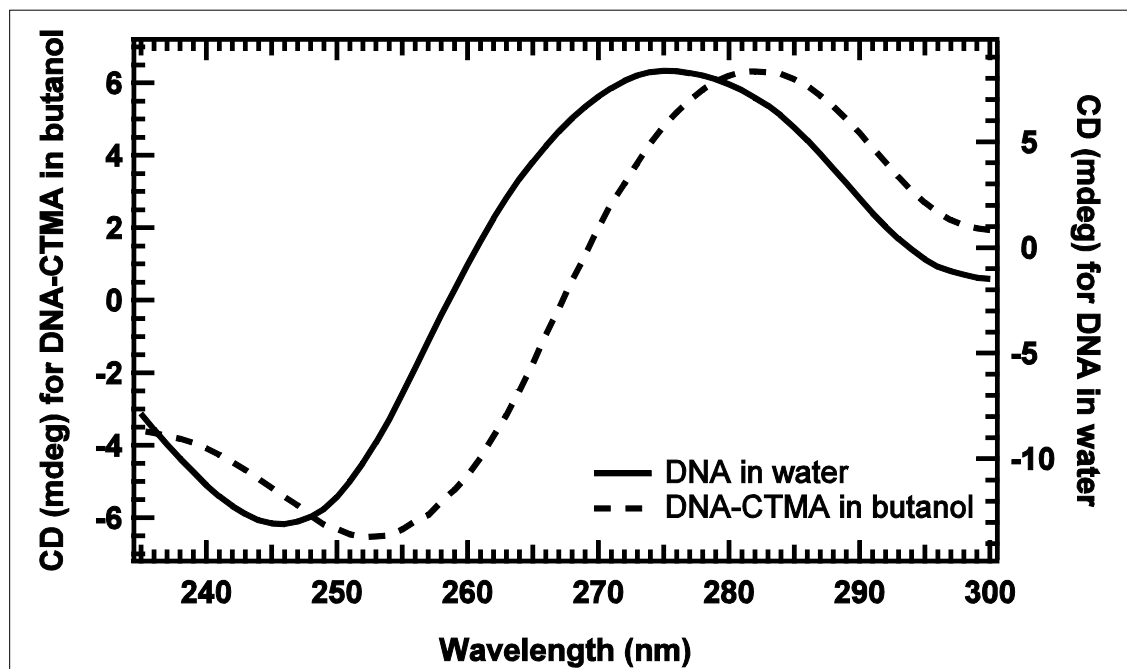


Figure 2. CD spectra of DNA in water and DNA-CTMA in butanol at room temperature.

DNA-CTMA shows the peaks characteristic of DNA, although they are shifted slightly due to the addition of CTMA to the DNA chain. This suggests the helix is intact in the DNA-CTMA butanol solution. The CD signal strength is different for each sample due to differences in concentration. An absorption scan at 260 nm as a function of temperature was used to determine the denaturation temperature of the complexed DNA-CTMA. In aqueous DNA, denaturation occurs at $\sim 90\text{--}95^\circ\text{C}$ ⁽⁵⁸⁾. Figure 3 shows the melting curve at 260 nm for the DNA received from CIST for both aqueous DNA and complexed DNA-CTMA in butanol. The absorption spectrum of the aqueous DNA received from CIST shows the expected increase in absorption centered around 90°C , confirming its expected denaturation temperature. The absorption spectrum for DNA-CTMA dissolved in butanol does not, however, show a substantial increase in absorption even up to 100°C (the high temperature limit for the instrument). This implies that the denaturing temperature for complexed DNA-CTMA is greater than 100°C .

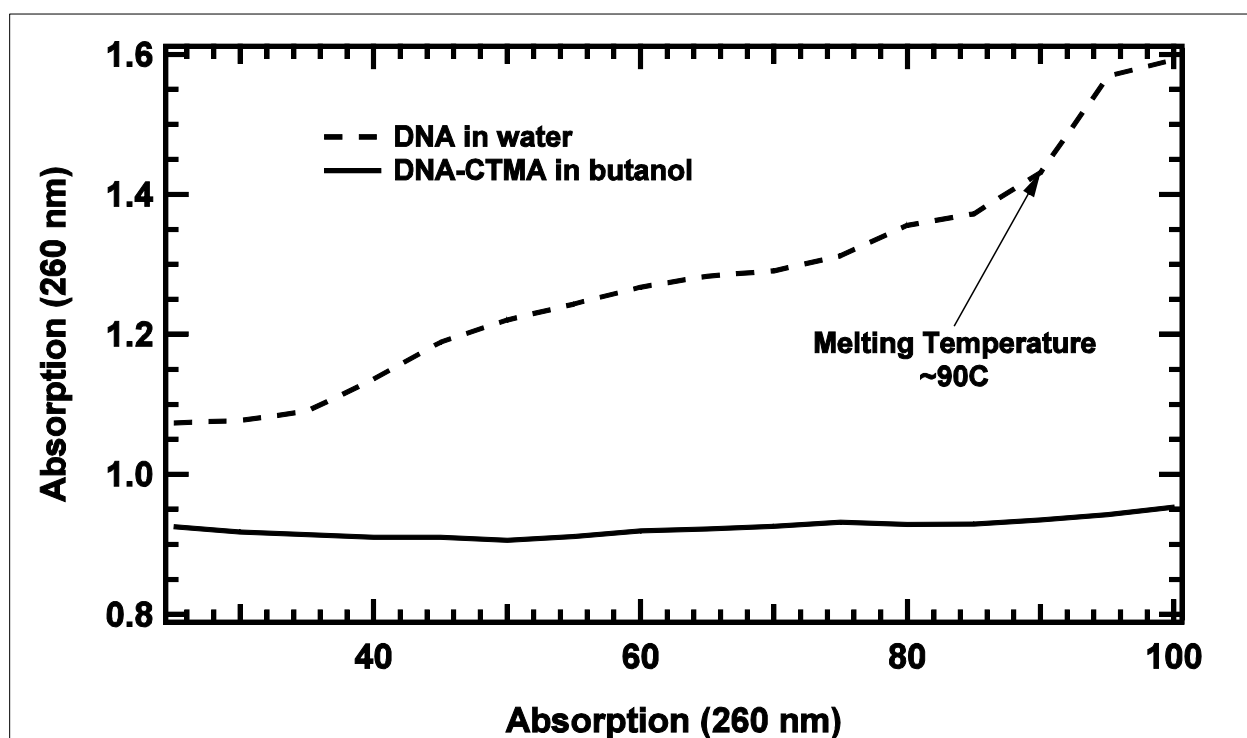


Figure 3. Melting curves of DNA in water and complexed DNA-CTMA in butanol.

Denaturation temperature of DNA in water is $\sim 90^\circ\text{C}$, the denaturation temperature of DNA-CTMA is $>100^\circ\text{C}$.

The CD data confirm that the helix is preserved for the DNA-CTMA solution at room temperature, and the 260 nm absorption data indicate that it remains preserved for temperatures $>100^\circ\text{C}$. It is unknown if the helix is intact for a cured DNA-CTMA film. However, because the noncrosslinked DNA-CTMA films are fully cured at 80°C , well below 100°C , it can be concluded that the double helix also remains intact in the cured, noncrosslinked DNA-CTMA films. Even though the crosslinked films are fully cured at temperatures greater than 100°C , the solvent is completely removed at 80°C . It is therefore reasonable to conclude that the double helix is also intact for crosslinked DNA-CTMA films. A more detailed structural analysis is needed to fully confirm this

supposition.

1.3.2 Index of refraction

The index of refraction was measured with the Metricon 2010 Prism Coupler at three discrete wavelengths (632.8 nm, 1152 nm and 1523 nm). A Cauchy fit to these data was used to plot the dispersion. The indices of refraction were measured for noncrosslinked DNA-CTMA for three different molecular weights (200 kDa, 500 kDa, and 5,000 kDa) and are shown with a Cauchy fit in Figure 4. Within experimental uncertainty, there is no appreciable difference in the indices as a function of molecular weight. The addition of the PPIF crosslinker raises the index of refraction as does the addition of a chromophore dye.

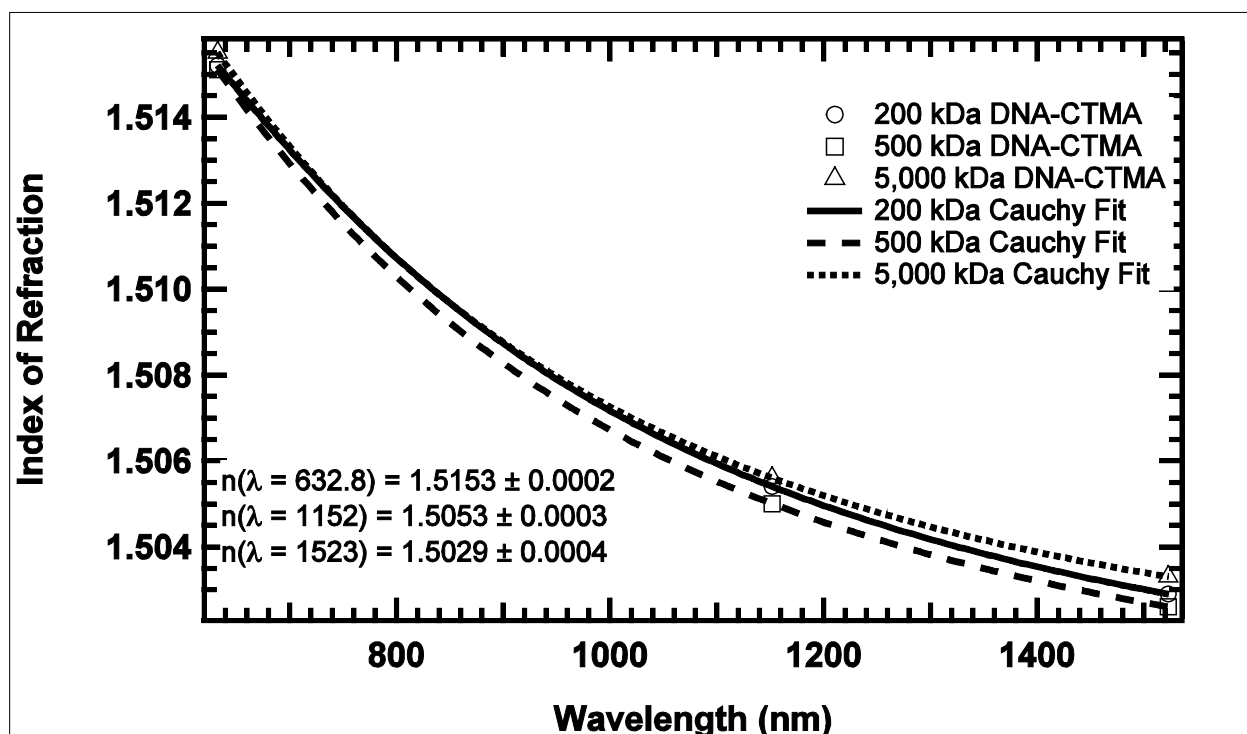


Figure 4. Index of refraction with Cauchy fit of DNA-CTMA for three different molecular weights.

Within experimental uncertainty, there is no appreciable change in index with molecular weight.

1.3.3 Optical loss

1.3.3.1 Absorption loss

A Hitachi model 4001 UV-VIS spectrophotometer was used to measure the optical absorption loss for a thick ($>100\ \mu\text{m}$) noncrosslinked DNA-CTMA film over a wavelength range of 400 – 1600 nm. The thick DNA-CTMA free-standing film used for the transmission measurement was made by slowly evaporating a DNA-CTMA-butanol solution in a Teflon mold in a 40°C vacuum oven. This technique could not be used to measure the absorption loss for a crosslinked DNA-CTMA film due to excessive cracking of the thick crosslinked films.

The absorption loss for a noncrosslinked DNA-CTMA film is shown in Figure 5. The film was measured to be 356 μm thick. The spectrum was shifted slightly to zero loss at 790 nm. The loss was found to be <1 dB/cm at the communications wavelengths: 0.1 dB/cm at 800 nm, 0.2 dB/cm at 1300 nm, and 0.7 dB/cm at 1550 nm. This shows that the conventional criterion that the loss for waveguide applications be ≤ 1 dB/cm at the communications wavelengths is met. The loss was also calculated at 690 nm because of the many measurements taken at this wavelength and was found to be 1.2 dB/cm.

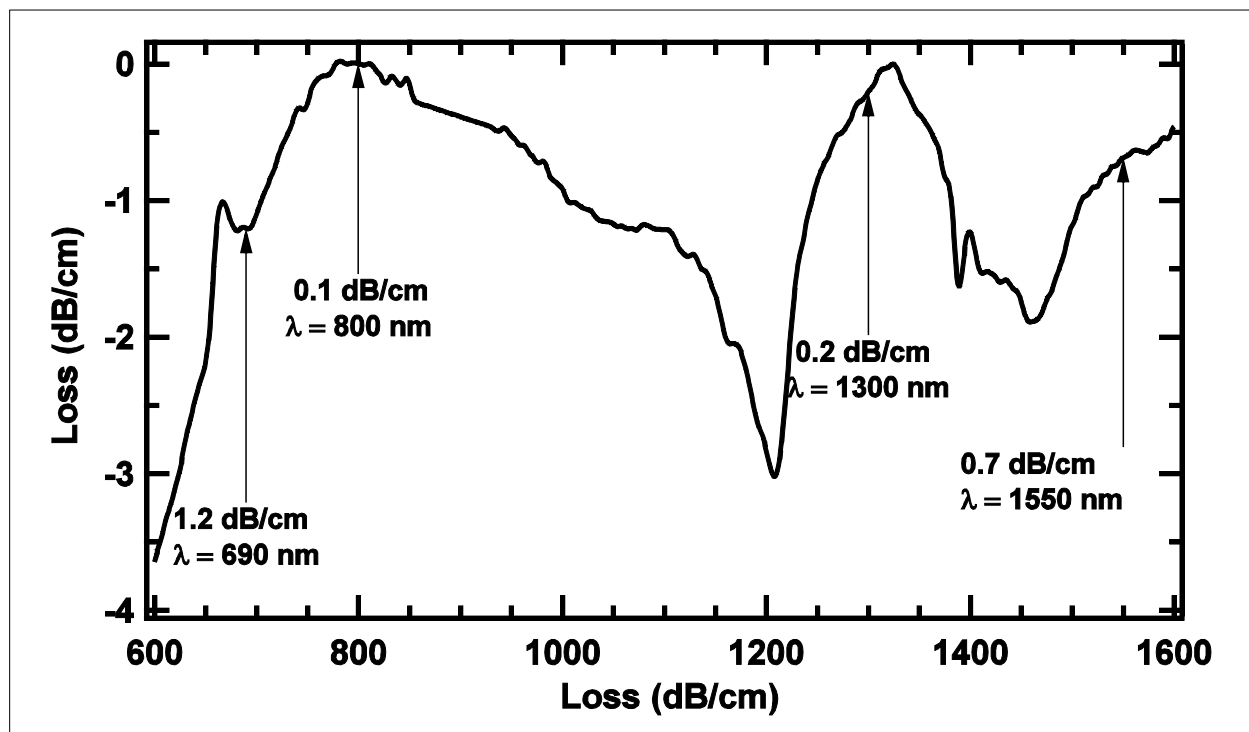


Figure 5. Absorption loss spectrum of a 356 μm thick film of noncrosslinked DNA-CTMA.

The losses at the communications wavelengths are shown to be < 1 dB/cm.

1.3.3.2 Propagation loss

Optical waveguide losses were measured at 690 nm for single layer DNA-CTMA and DNA-CTMA-PPIF by coupling light into the films using the prism coupling method (Pollock 1994). The films act as the core layers of one dimensional waveguide with SiO_2 ($n = 1.46$ at 690 nm) and air ($n=1$) acting as the two cladding layers. The streak propagating through the waveguide is captured with a Sony Cybershot DSC-P93 5.1M pixel digital camera. The length of the streak is calibrated by placing a ruler directly over the streak and recording a photo of the ruler with the camera in the exact position where the photo of the streak was recorded.

The optical waveguide loss was calculated for a noncrosslinked DNA-CTMA film and for three crosslinked DNA-CTMA films with varying concentrations of crosslinker: 10 wt%, 15 wt% and 20 wt% PPIF. The losses for these films at 690 nm are shown in Table 2. The loss increases with increasing concentration of crosslinker. Although the losses reported are >1 dB/cm, these values are for measurements at 690 nm, where higher loss is expected. At 690 nm, the crosslinked films

show a loss increase of ~20% and ~40%, respectively, for the 10 wt% and 15 wt% PPIF films compared to the noncrosslinked film. Assuming the same percentage increase of loss at the communications wavelengths (where for the noncrosslinked film the loss was 0.2 dB/cm at 1300 nm and 0.7 dB/cm at 1550), the absorption and scattering losses in these materials should be sufficiently low at the communications wavelengths.

Table 2. Waveguide loss for varying concentrations of PPIF crosslinker in DNA-CTMA films.

Amount of PPIF crosslinker (wt%)	Amount of PPIF crosslinker (mol%)	Waveguide Loss (dB/cm)
0	0	$1.25 \pm 0.6\%$
10	36.1	$1.48 \pm 1.6\%$
15	57.3	$1.79 \pm 0.8\%$
20	81.2	$3.08 \pm 0.6\%$

1.3.4 Thermal properties

Thermogravimetric analysis (TGA) and differential scanning calorimetry (DSC) were used to characterize the thermal properties of DNA in its various forms. The materials analyzed were: 1) unprecipitated DNA (the raw material received from CIST); 2) DNA-CTMA powder; 3) a DNA-CTMA film; and 4) a crosslinked DNA-CTMA film. TGA was used to determine the thermal stability of the materials, and DSC was used to determine the glass-transition temperature T_g of the materials. The TGA curves for the four DNA materials are shown in Figure 6. The materials show no sharp change in weight up to 200°C, suggesting that they are thermally stable and suitable for device operation up to this temperature. The DSC results are shown in Figure 7. A glass transition temperature of 148.17°C was detected for the DNA-CTMA *powder*; however, a clear T_g could not be detected for the DNA-CTMA *film* or for the other samples.

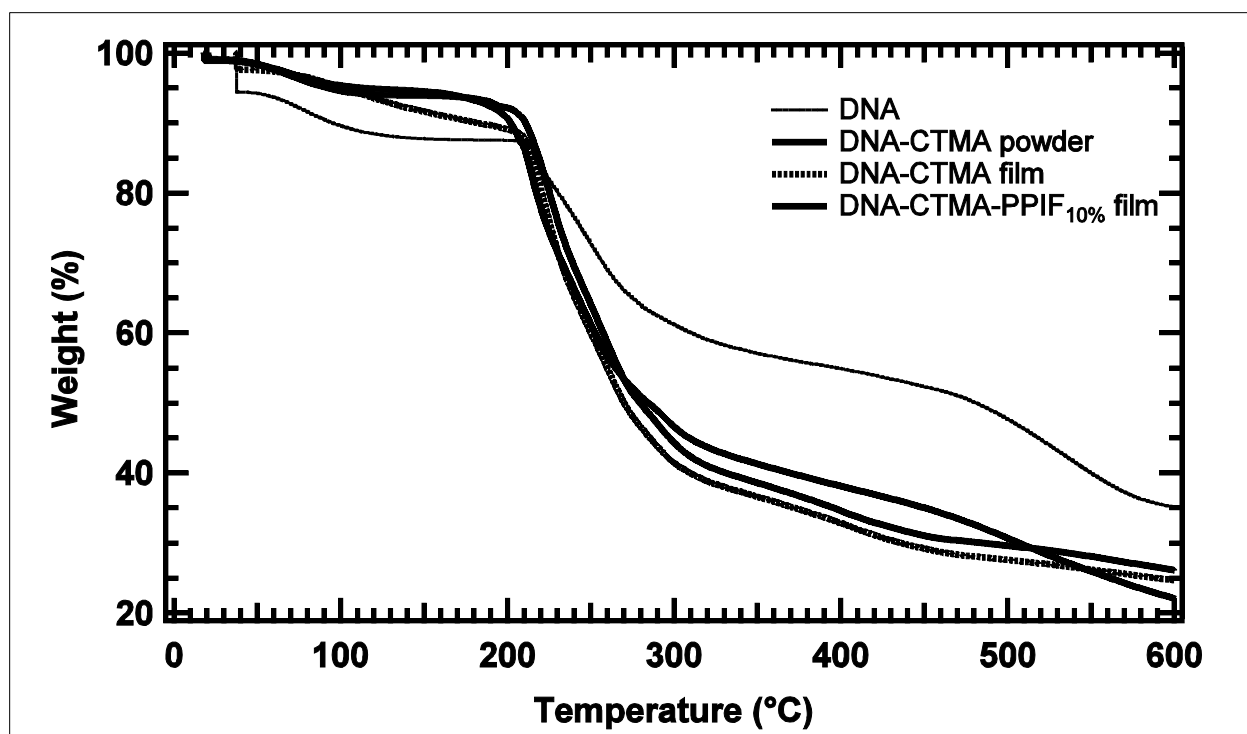


Figure 6. TGA curves for DNA specimens.

There is no appreciable weight loss up to 200°C, indicating these materials are thermally stable up to this temperature.

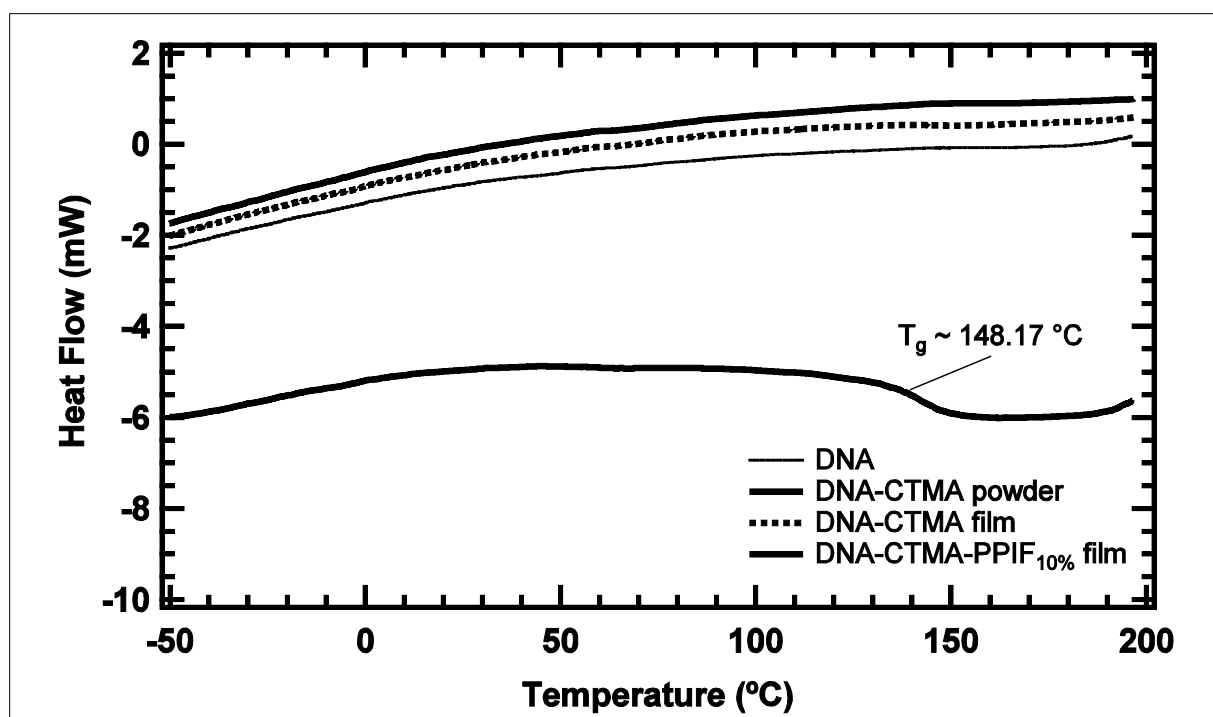


Figure 7. DSC curves for DNA specimens. The DNA-CTMA powder has a T_g of 148.17°C; however, a clear T_g could not be detected for the other materials.

1.4 RF ELECTRICAL CHARACTERIZATION

1.4.1 Capacitive Test Structure

A new capacitive test structure is used to characterize the electrical properties of polymer and biopolymer thin films^(29, 30). Specifically, this capacitive test structure provides a mechanism for determining the dielectric properties of polymer and biopolymer materials in an easily fabricated device. The dielectric properties obtained using the capacitive test structure are determined from microwave measurements.

The capacitive test structures used in these studies are fabricated on a two-inch wafer of high resistivity ($> 10 \text{ k}\Omega$) silicon using shadow masks and spin-coating. The capacitive test structure is shown in Figure 8. This structure is made up of four distinct layers on the silicon wafer. The adhesion layer consists of 100 Å of chromium sputtered through a shadow mask directly onto the silicon wafer. The bottom metal layer, which is formed from 7500 Å of gold deposited by electron beam (e-beam) deposition through the same shadow mask onto the adhesion layer, consists of two ground lines shunted together at their midpoints by a 100 μm wide conductor in the shape of an H. The next layer is the polymer under study, which is deposited as a thin-film by spin-coating on top of the gold. The top layer is 3500 Å of gold, deposited by e-beam deposition through a second shadow mask. This layer forms a ground-signal-ground coplanar waveguide (CPW) transmission line. The CPW line consists of two ground lines, positioned directly above the ground lines in the bottom metal layer, and a signal line, centered between the ground lines and perpendicular to the shunt line in the bottom metal layer. The active region of this test structure is the area where the signal line in the top metal layer overlaps the shunt line in the bottom metal layer. The active region forms a test capacitor, which has an area of approximately 100 μm by 100 μm . The test structure has a large ground pad capacitor that results from the overlap of the ground lines in the top and bottom metal. Since the test capacitor is in series with the much larger ground pad capacitor, the effective capacitance is that of the test capacitor. When a DC bias is applied, the DC current passes through the leakage conductance of the test capacitor, the shunt line in the bottom metal and the leakage conductance of the ground pad capacitor. This eliminates the need for via holes to ground the bottom conductor. Since the large ground pad capacitor has a much higher leakage conductance, the DC bias applied to the signal conductor drops almost entirely across the test capacitor. Figure 9 shows a photograph of the capacitive test structure being measured.

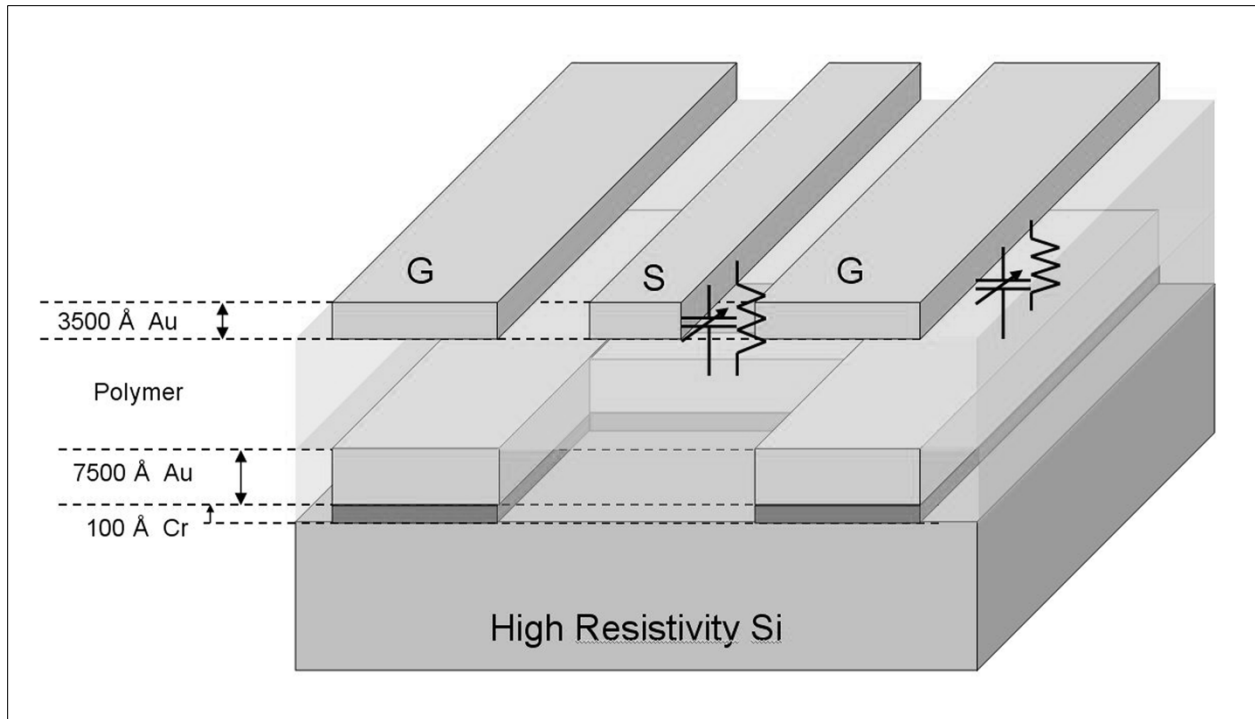


Figure 8. A three dimensional representation of the capacitive test structure, showing the overlap of the signal conductor in the top-metal and the shunt line in the bottom metal which form the test capacitor.

Notice that the large ground pad capacitor is in series with the test capacitor, resulting in the equivalent capacitance of the test capacitor.

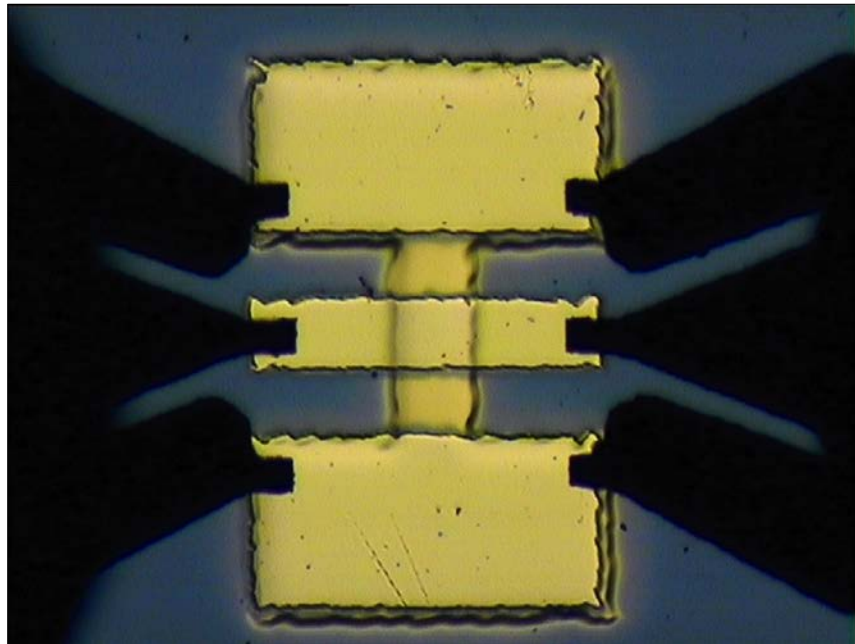


Figure 9. A photograph of a capacitive test structure with the CPW probes in place to make microwave measurements.

An electrical model of the capacitive test structure is shown in Figure 10. In this model, $C(V)$ is the test capacitance of the polymer in the active region, and $R(V)$ is the shunt resistance modeling the leakage conductance of the test capacitor. R_s and L are the parasitic series resistance and inductance, respectively, for the test capacitor. Using this electrical model and the scattering parameters (S parameters), the relative dielectric constant (ϵ_r) and loss tangent ($\tan \delta$) of the polymer can be derived as described below.

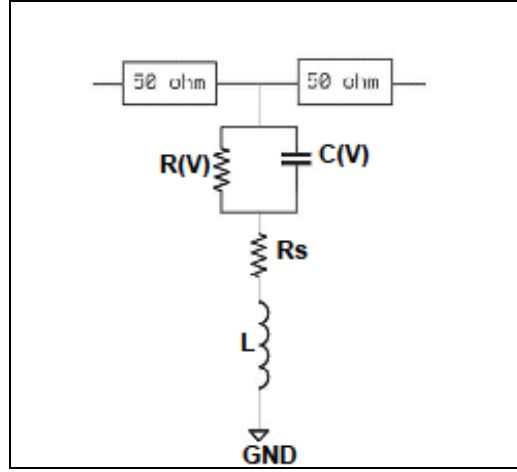


Figure 10. The electrical model for the capacitive test structure.

Since this system is a two-port reciprocal network, deriving the S parameters amounts to deriving S_{11} and S_{21} . For any reciprocal two-port network S_{11} is identical to S_{22} and S_{21} is identical to S_{12} . Any single S parameter, S_{ij} , is defined as

$$S_{ij} = \frac{V_i^-}{V_j^+} \quad (1)$$

where V_j^+ is the amplitude of the wave incident on port j and V_i^- is the amplitude of the wave reflected out of port i (Pozar 1998). This is determined when the only incident wave in the system is that incident upon the input port, port j, and all other ports are terminated with matched loads to avoid reflections. For the two-port network that describes the capacitive test structure, with port 1 as the input port and port 2 as the output port, it can be shown that

$$S_{11} = \frac{Z_{in}^1 - Z_0}{Z_{in}^1 + Z_0} \quad (2)$$

And

$$S_{21} = \frac{v_o}{v_{in}} \quad (3)$$

where Z_{in}^1 is the impedance seen looking into port 1 and Z_0 is the characteristic impedance of the transmission line. To algebraically calculate the S parameters for the capacitive test structure, one must account for the loss associated with the real transmission line. In this case, the loss associated with each 50 Ω transmission line is assumed to be 1 Ω . Using Figure 10 and the characteristic impedance $Z_0 = 50 \Omega$, Z_{in} and the S parameters for the capacitive test structure can be computed as

$$Z_{in} = 1 + \frac{51(R + j\omega L + (1/R + j\omega C)^{-1})}{51 + R + j\omega L + (1/R + j\omega C)^{-1}} \quad (4)$$

$$S_{11} = \frac{2R + 2j\omega L + 2(\frac{1}{R} + j\omega C)^{-1} - 2499}{102R + 102j\omega L + 102(\frac{1}{R} + j\omega C)^{-1} + 24601} \quad (5)$$

And

$$S_{21} = \frac{50[R + j\omega L + (\frac{1}{R} + j\omega C)^{-1}]}{51[51 + R + j\omega L + (\frac{1}{R} + j\omega C)^{-1}]} \quad (6)$$

The relative dielectric constant, ϵ_r , is determined from the capacitance in the electrical model. The capacitance is that of the parallel plate capacitor consisting of the polymer film in the active region. Manipulating the equation for the capacitance of a parallel plate capacitor, the relative dielectric constant can be computed as

$$\epsilon_r = \frac{C(V)t}{\epsilon_0 A} \quad (7)$$

where $C(V)$ is the capacitance, ϵ_0 is the permittivity of free space, A is the overlap area of the active region, and t is the thickness of the polymer. The loss tangent ⁽⁶⁸⁾ is found from the electrical model of the capacitive test structure, using the equation for the shunt resistance such that ⁽²³⁾

$$\tan(\delta) = \frac{1}{\omega R(V)C(V)} \quad (8)$$

where ω is the angular frequency, $R(V)$ is the shunt resistance, and $C(V)$ is the capacitance shown in Figure 10 at a single bias voltage ⁽²⁶⁾.

1.4.1.1 Experimental Procedure

The specific values for the parameters in the electrical model are determined experimentally by fitting the circuit model to the experimentally obtained S parameters using the simulation package in Applied Wave Research's (AWR) Microwave Office® tools. A Hewlett Packard 8720B Microwave Network Analyzer and an on-wafer microwave probe station, shown in Figure 11, are used to measure the S parameters of the capacitive test structure. The setup used to measure the S parameters is the same two-port network, with one port at each end of the signal line, as is described above for the theoretical calculations. The procedure for experimentally determining the S parameters in this study uses the following steps: First, the network analyzer and probe station are calibrated to the device over the frequency range of interest using a Line-Reflect-Reflect-Match (LRRM) calibration (Purroy and Pradell 2001). The frequency range of interest for this work is five to twenty gigahertz, when the data is taken at the Sensors Directorate of the Air Force Research Laboratory, since conductive thickness effects cause skin depth issues that limit the low frequency and equipment limitations restricts the high frequency, and ten to eighteen gigahertz, when the data is taken at the University of Dayton, also due to equipment limitations. Then, the silicon wafer is raised to the temperature of interest and the appropriate DC bias voltage is applied to the signal lead of the probe. Finally, the S parameters are recorded.

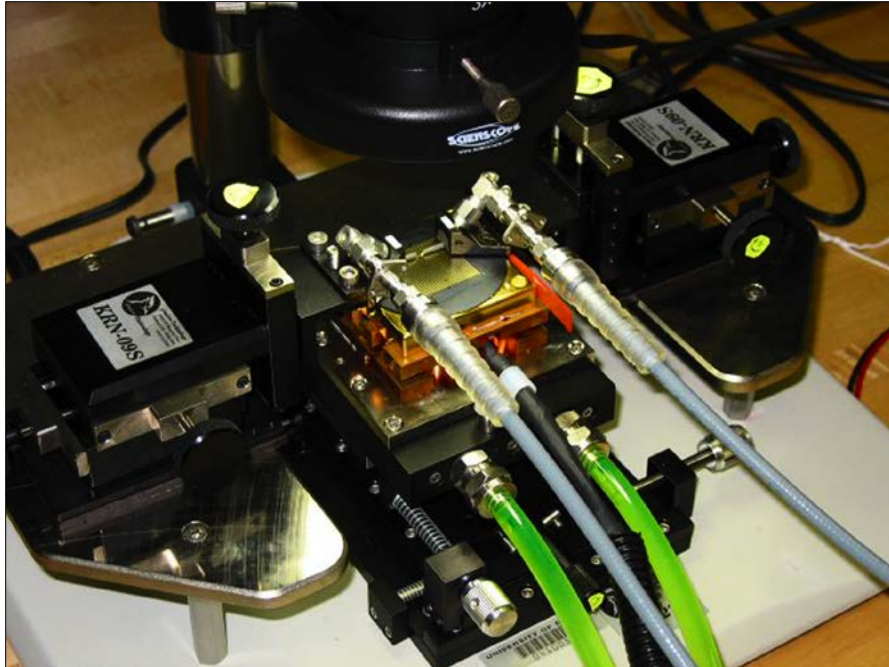


Figure 11. The microwave probe station pictured with the right probe on a capacitive test structure containing BSA-PVA and the left probe hovering above the sample.

The measured S parameters are then imported into the AWR Microwave Office® simulation package. Using the electrical model for the test structure, shown in Figure 11, the electrical parameters are determined. First, an initial estimate of the values in the electrical model of the capacitive test structure is made. Then, the electrical model is manually tuned to match the experimental results for both S_{11} and S_{21} , simultaneously, across the frequency range. This procedure is repeated for each capacitive test structure at every bias voltage and temperature yielding the specific values for the electrical model. Since there are four parameters ($C(V)$, $R(V)$, R_S , and L) in the electrical model that are being varied to match the experimental data, using just the S_{21} or S_{12} curve can result in several matches that appear to be good. However, using both the S_{21} (or S_{12}) curve and the S_{11} (or S_{22}) curve generally produces a unique electrical model that matches both curves well. Figure 12 shows an example of the AWR Microwave Office screen while matching the electrical model to the experimental data. The electrical model is seen on the top right, with the variable tuner below it. The S_{12} graph containing both the experimental data and the theoretical data is seen on the top left and the S_{11} graph is visible on the bottom left (Bartsch et al. 2006, Bartsch et al. 2007).

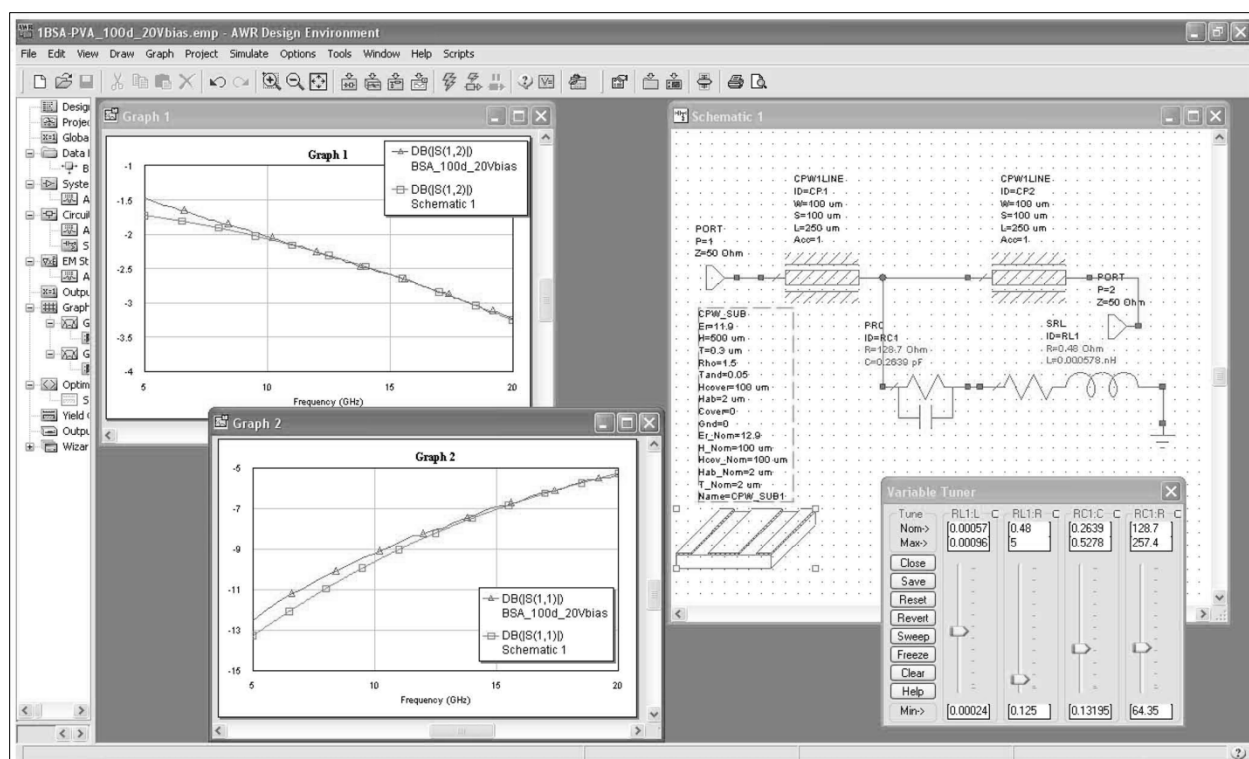


Figure 12. An example of the AWR Microwave Office screen while matching circuit parameters with the measured S parameters.

The graphs of S_{11} and S_{12} with both experimental and theoretical data from the model are seen on the left side of this figure. The electrical model and the variable tuner are seen on the right side of this figure.

1.4.1.2 Results and Analysis

The polymer poly(bisphenol A carbonate-co-4,4'-(3,3,5-trimethylcyclohexylidene)diphenol carbonate), commonly known as APC, is used as a reference polymer for comparison to the DNA-biopolymer, DNA-CTMA. Variations in the S_{21} measurements are found to occur for different capacitive test structures on the same substrate. This is presumably due to thickness variations in the thin films, which cause different thicknesses in the active region of the various capacitive test structures containing the thin film. Since it is not possible to measure the thickness of the film for a particular test structure, the average film thickness is used to obtain the dielectric properties. The average thickness of the APC film is 2.03 μm and of the DNA-CTMA film is 1.78 μm . The following subsections focus on identifying and analyzing the response of APC, DNA-CTMA, and a known ferroelectric material, barium strontium titanate (BST) under the various conditions measured.

1.4.1.2.1 APC

A typical example of S_{21} data obtained for the reference polymer, APC, is plotted in Figure 13. This figure shows that at room temperature the value of S_{21} decreases with increasing frequency, and at 100°C the value of S_{21} decreases with increasing frequency for frequencies above 6.4 GHz, while at frequencies below 6.4 GHz there is a brief decrease in S_{21} and then an increase. These

lower frequency, high temperature effects on S21 are probably caused by the conductor thickness and skin depth effects occurring at slightly higher frequencies than expected, and therefore the brief increase in S21 at 100 °C should be neglected. From Figure 13 it is evident that changing the bias voltage applied to APC in the capacitive test structure does not affect its frequency response. Also note that increasing the temperature of the polymer increases the transmittance of the signal for frequencies above seven gigahertz.

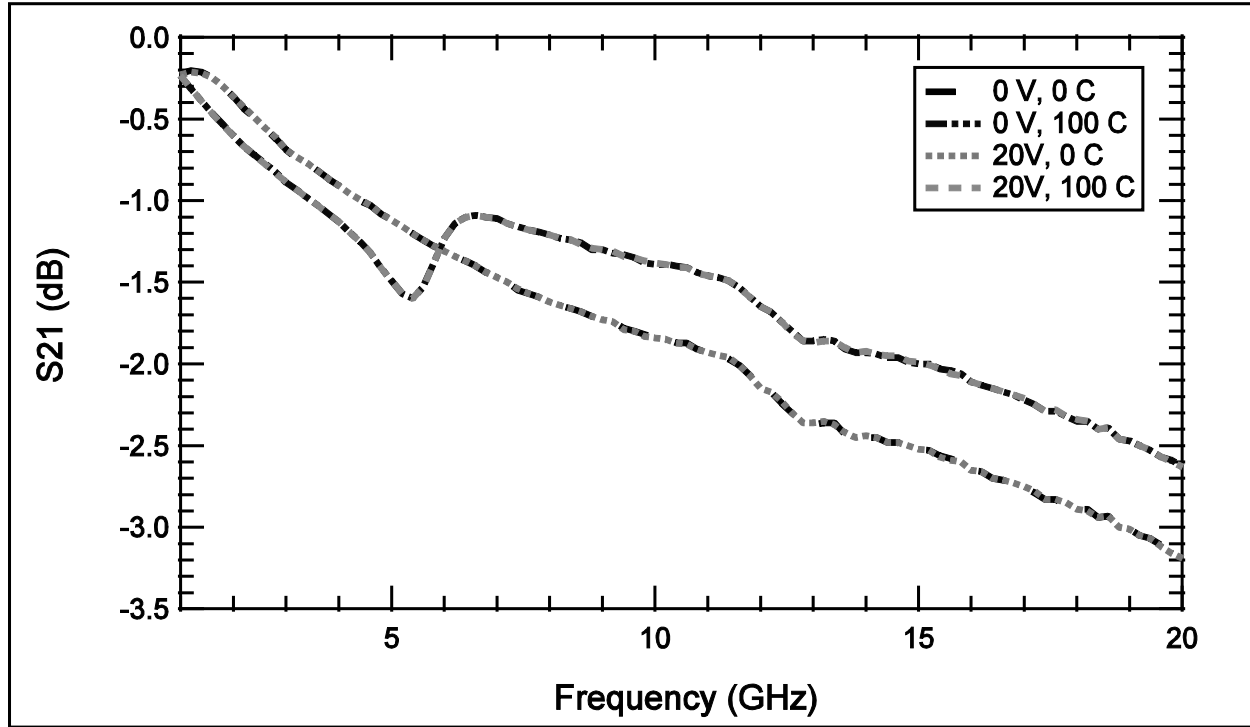


Figure 13. The frequency response of S21 for a capacitive test structure of APC.

1.4.1.2.2 DNA-CTMA

The frequency dependence of S21 for a capacitive test structure containing DNA-CTMA is plotted at room temperature with various applied bias voltages in Figure 14. This figure shows that for all applied biases measured, the transmittance decreases monotonically with increasing frequency. This means that more of the input signal put into port 1 of the capacitive test structure is measured at port 2 when the frequency is lower than is measured at port 2 when the frequency is higher. Figure 14 also shows that the transmittance of the capacitive test structure containing DNA-CTMA changes with applied bias. The transmittance is constant for applied biases up to 10.0 V. At 12.5 V, the transmittance increases slightly, with a greater increase taking place at 15.0 V. The largest increase in transmittance occurs between 15.0 and 17.5 V, and the increase in transmittance is again very slight between 17.5 and 20.0 V.

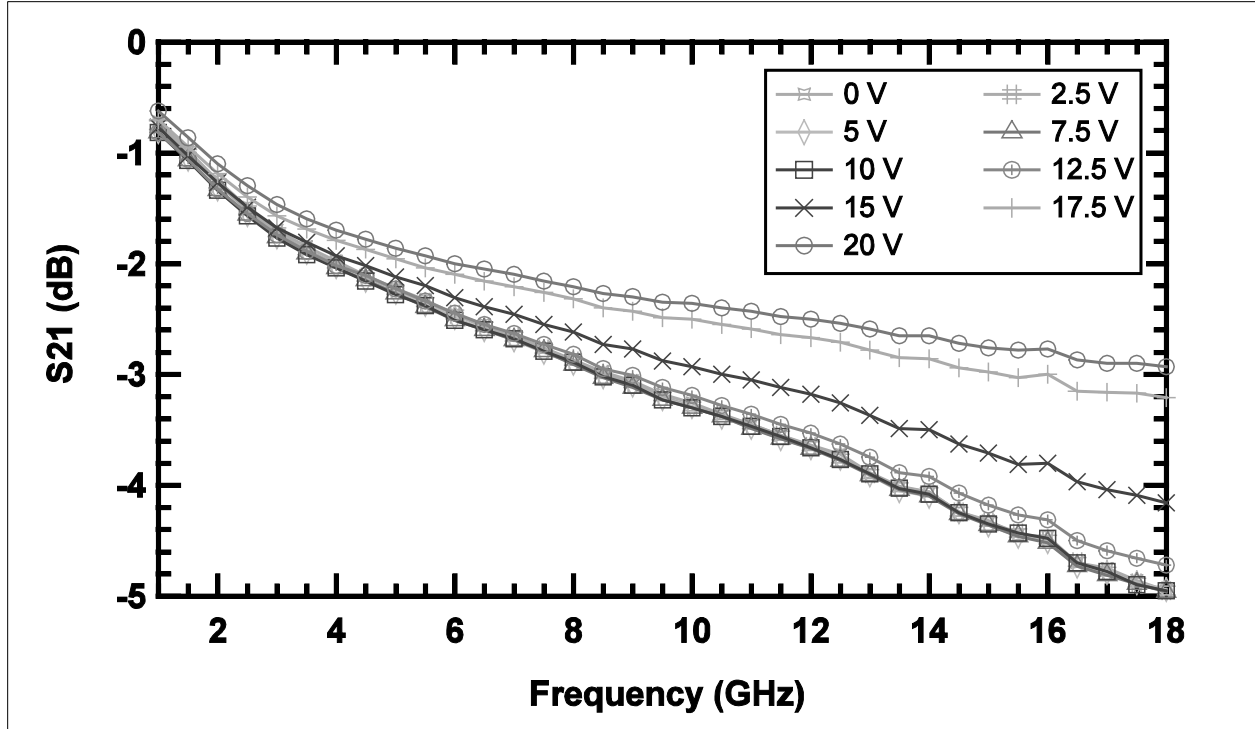


Figure 14. The frequency response of S21 for a capacitive test structure containing DNA-CTMA at room temperature for various applied biases from 0 to 20 V

This change in transmittance corresponds to a decrease in the equivalent circuit capacitance and also in the relative dielectric constant of the DNA-CTMA. Figure 15 shows the calculated relative dielectric constant of DNA-CTMA as a function of applied voltage obtained from analyzing the S parameters in Figure 14 measured on a capacitive test structure containing DNA-CTMA. This figure shows that the relative dielectric constant decreases with increasing applied bias. When the slope is zero, the relative dielectric constant is a constant value. When the slope is non-zero, the relative dielectric constant is changing with applied voltage. The change in relative dielectric constant is greatest when the slope is steepest. The relative dielectric constant of the DNA-CTMA film is 6.56 at 0.0 V and drops to a value of 3.12 at 20.0 V. This corresponds to 52% dielectric tuning as the applied electric field changes from 0 to 113 kV/cm.

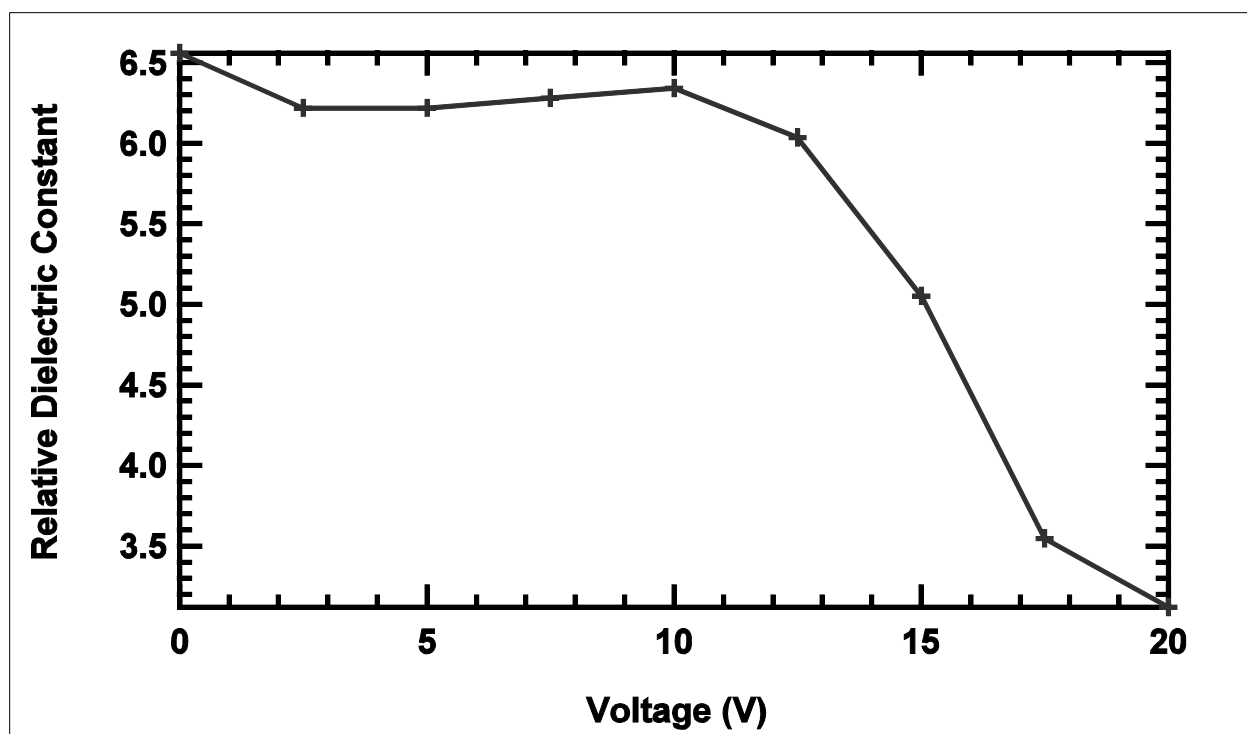


Figure 15. The calculated relative dielectric constant as a function of applied voltage for DNA-CTMA using the measured S parameters from a capacitive test structure.

To quantify if the measured tuning is statistically significant, a two-sided paired t-test is used to determine if there is a difference in the relative dielectric constant values for the DNA-CTMA film at 0.0 and 20.0 V. Using the paired t-test, $|t| = 2.15$, which is greater than $t_{0.05} = 1.80$. Therefore, it can be concluded at the 90 % confidence level that there is a difference in the relative dielectric constants of the DNA-CTMA film at 0.0 and 20.0 V. These results from the two-sided paired t-test provide confidence in the analysis that the DNA-CTMA film tunes with applied voltage.

Figure 16 shows the frequency response of S21 for a capacitive test structure containing DNA-CTMA at 100 °C with various applied biases. This figure shows that the transmittance decreases with increasing frequency for both 0 and 20 V at 100 °C. Figure 16 also shows that S21 does not change with applied bias for DNA-CTMA at 100 °C. This means that while the relative dielectric constant of DNA-CTMA tunes at room temperature, as the temperature increases it does not continue to tune. The reason why the dielectric tunability occurs at room temperature but not at 100 °C is unknown. One possible explanation, however, is that the thin film of DNA-CTMA has a glass transition temperature, T_g , between room temperature and 100 °C. The T_g of DNA-CTMA thin films is unknown because it is undetectable by differential scanning calorimetry, although the T_g of the DNA-CTMA powder has been measured to be 148 °C⁽⁵²⁾. If the DNA-CTMA thin film has passed the transition temperature by 100 °C, then the DNA-CTMA thin film is softer and more flexible at 100 °C than it is at room temperature. This change might explain the differences in the transmittance measurements at room temperature and 100 °C for this biopolymer^(27, 28, 30).

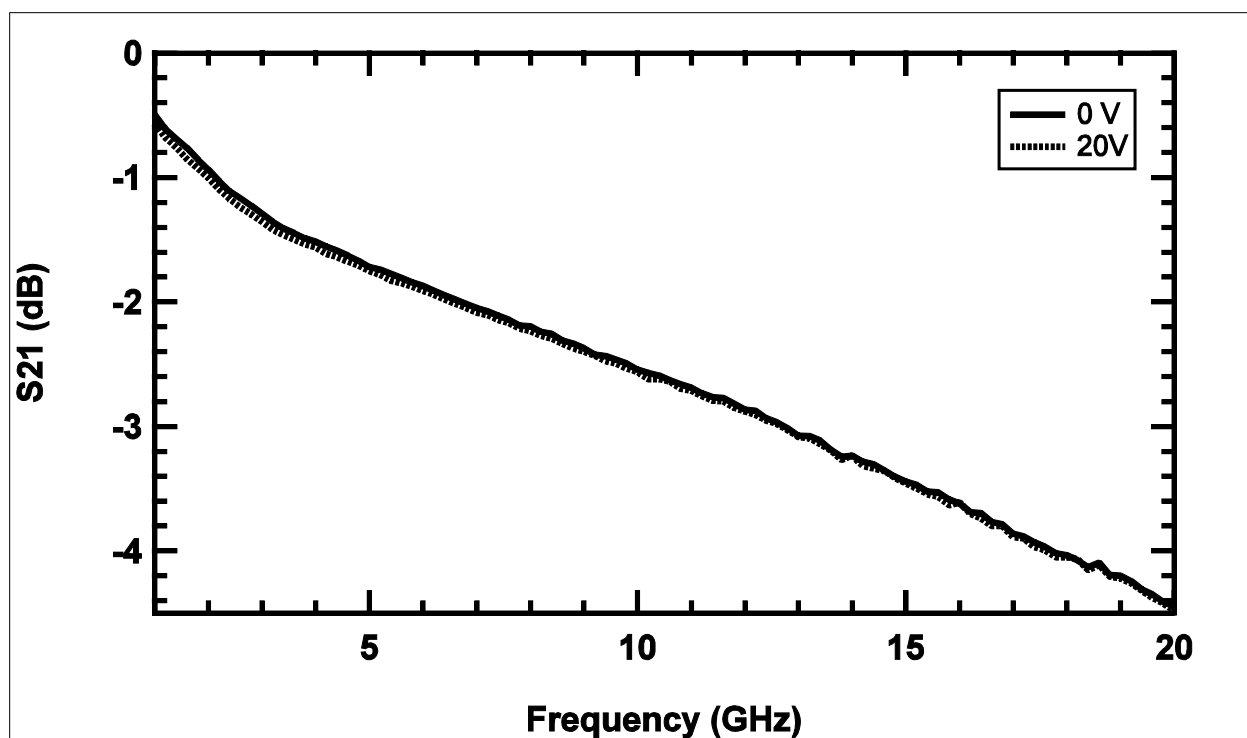


Figure 16. The frequency response of S21 for a capacitive test structure containing DNA-CTMA at 100°C for various applied biases from 0 to 20 V.

1.4.1.2.3 BST

The dielectric properties of the tunable biopolymers described above should be compared to a known inorganic material with voltage tunable dielectric properties, such as barium strontium titanate (BST). The frequency response of S21 for a capacitive test structure containing 300 nm of BST is plotted in Figure 17 with applied biases varying from 0.0 to 3.0 V. This figure shows that the transmittance decreases with increasing frequency at each of these applied biases. The figure also shows that the transmittance increases with increasing applied bias, and confirms that the dielectric properties of BST tune with applied bias. The increasing transmittance corresponds to a decreasing capacitance and therefore a decreasing relative dielectric constant. The relative dielectric constant tunes by 47 % as the applied voltage changes from 0.0 to 3.0 V, which for the 300 nm thick film of BST corresponds to a change in the applied electric field from 0 to 100 kV/cm at room temperature.

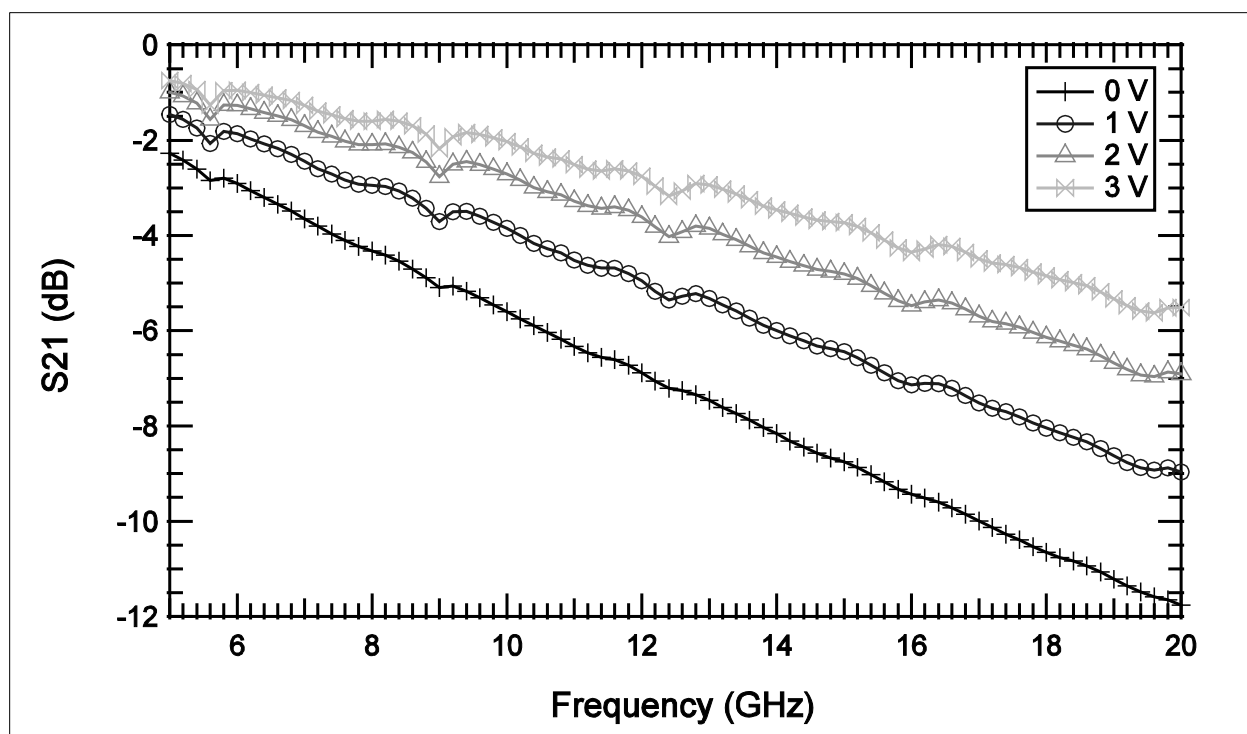


Figure 17. The frequency response of S21 for a capacitive test structure containing BST for applied biases from 0 to 3 V.

It is useful to note that DNA-CTMA film tunes more than the BST film at room temperature. The DNA-CTMA films are unoptimized and are already showing tuning on the order of that seen in the BST film. This suggests that DNA-biopolymers can be used in applications that utilize dielectric tunability, such as sensors and antennas.

1.4.1.3 Capacitance Measurements

Capacitance is measured as a function of frequency to confirm that the electrical properties obtained from the microwave measurements are those of the polymer. This can be done by showing that the capacitance in the electrical model is that of the polymer and is not due to interface charges. An on-wafer probe station with micromanipulators and a HP 4284A Precision LCR (inductance-capacitance-resistance) meter are used to perform low-frequency characterization on thin films using the capacitive test structure. The LCR meter has the ability to vary the voltage, from -40 V to 40 V, and the frequency, from 20 Hz to 1 MHz, and to measure current. Using this equipment, the capacitance and dissipation factors can be obtained as a function of either frequency or bias voltage.

One example of the low frequency capacitance measurements obtained as a function of frequency for a DNA-CTMA capacitive test structure is plotted in Figure 18. This figure shows that the capacitance is very high at low frequencies and decreases to the bulk capacitance with increasing frequency. The high capacitance present at very low frequencies is due to interface charges that are quickly depleted as the frequency increases. The rate of depletion slows down as the frequency increases and therefore equilibrium is approached at the higher frequency values. The equilibrium capacitance value is that of the bulk capacitance and is the same as that obtained from the

microwave frequency measurements. Other capacitive test structures have been measured in this same manner and produce similar results. This verifies that the capacitance values, and therefore the relative dielectric constant and loss tangents obtained from the microwave characterization measurements described above, are for the bulk polymer and are not due to the polymer-metal interfaces in the capacitive test structure ⁽²⁹⁾.

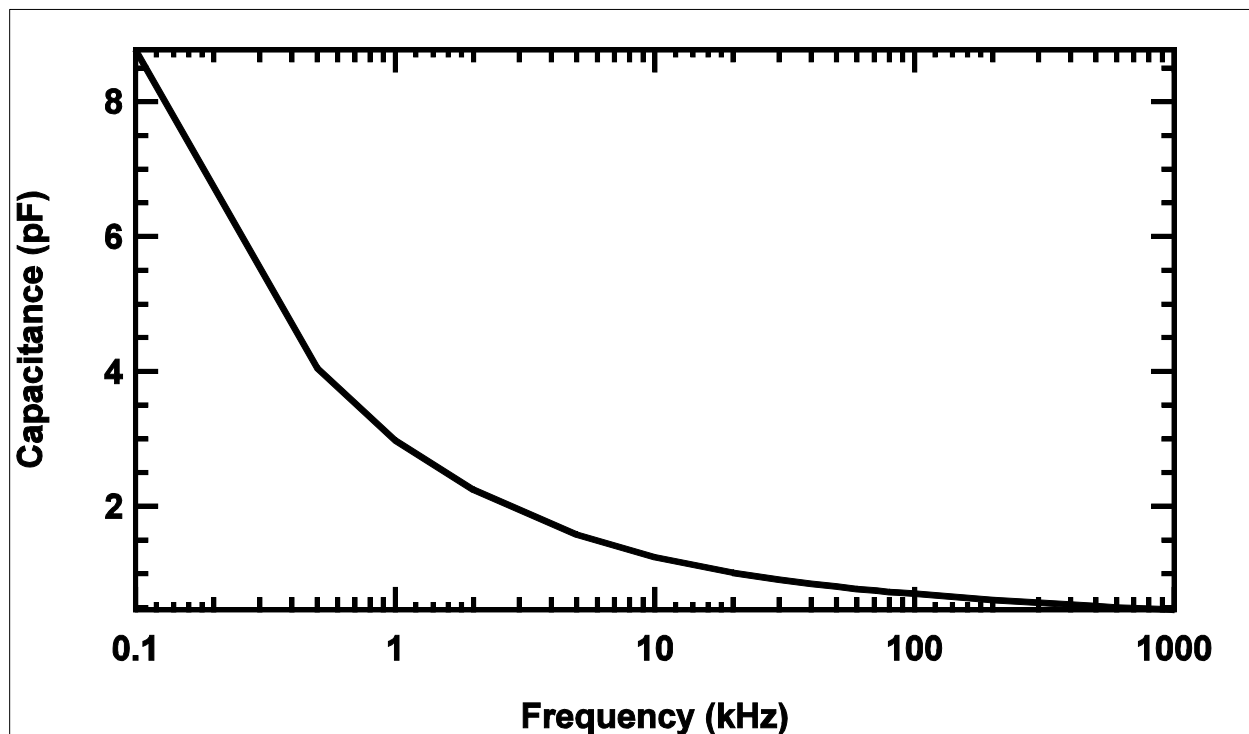


Figure 18. Capacitance as a function of frequency on a log scale for one capacitive test structure made with a DNA-CTMA thin film.

1.4.2 Electric Force Microscopy

Electric force microscopy (EFM) images are taken to examine the mechanisms of the dielectric tunability observed for the capacitive test structure containing DNA-CTMA ^(76, 27). These measurements map the surface topography of the test structure and show the effect of a constant DC bias applied to the DNA-CTMA film by measuring the change in the electric field gradient across the region of interest. Changing the applied DC bias will confirm the dielectric tunability, if large changes in the EFM images are observed.

Atomic force microscopy (AFM) produces high resolution images of the surface topography. To obtain these topography images, a sharp tip on the edge of a flexible cantilever is scanned across the surface of the sample while the system maintains a small and constant force between the sample and the tip. The tip scans the surface in a raster pattern. The deflection of the tip is detected by a laser beam reflecting off the back of the cantilever into a photodetector, where differences in the output voltage correspond to changes in the cantilever deflection ⁽⁷¹⁾.

In this research, TappingMode AFM is used, in conjunction with EFM and Phase Imaging using a Veeco Instruments MultiMode Scanning Probe Microscope equipped with a NanoScope IIIa

Controller and Quadrex Phase-Detection⁽⁶⁹⁾. TappingMode AFM refers to the mode of operation where the AFM tip alternately touches the surface to make high resolution images and is lifted off of the surface to move between imaging locations, to avoid damaging the surface of the sample. In this mode, the AFM cantilever oscillates at its resonance frequency to lightly tap the surface with the AFM tip while imaging. The deflection of the laser beam is used to keep the tip a constant distance from the sample by moving the scanner vertically at every data point. The topographical image of the surface is formed from a record of the scanner's movement.

EFM maps the gradient of the electric field present between the tip and the sample at every point. The EFM images are generated by plotting the change in the phase, frequency, or amplitude of the cantilever oscillation as it encounters vertical repulsive and attractive electric field forces above the sample surface at each point⁽⁷⁴⁾. The change in phase or frequency detection is more commonly used than amplitude detection, as these methods result in better images. A DC bias voltage is applied to the sample through a conductive platinum-iridium coated AFM tip. The field variations due to trapped charges are mapped using EFM. This study images the electric field present between the sample and AFM tip by phase detection, and relies on the vertical force gradients from the sample causing changes in the resonance frequency of the cantilever. Attractive forces pull the AFM tip closer to the sample, thereby reducing the resonance frequency and increasing the phase component of the oscillating cantilever EFM.

Phase Imaging maps the phase of the cantilever oscillations during TappingMode AFM scans. The phase lag of the cantilever, with respect to the drive signal, is monitored for each point during the scan. This imaging highlights edges and provides more information about fine features that can be hidden by a rough surface⁽²⁵⁾.

The scans are performed on a five micron square area of the center of a capacitive test structure containing DNA-CTMA in air at ambient temperatures. A scan rate of two Hertz is used with cantilever resonance frequencies of 65 to 68 kHz. Silver paint is applied from the steel magnetic AFM sample stub to the top of the grounding pads to provide a consistent ground. LiftMode is used to obtain the EFM maps of electric field gradient and distribution as a function of applied voltage, ranging from 0.0 to 12.0 V. LiftMode separately measures topography and electric force in a two pass technique, using topographic information to track the probe tip at 41 nm above the surface. Figure 19**Error! Reference source not found.** and Figure 20 show the TappingMode topography, EFM, and phase images from left to right, as measured on the active region of the capacitive test structure, with applied DC biases of 5.5 V, 6.0 V, 6.5 V, 7.0 V, and 7.5 V.

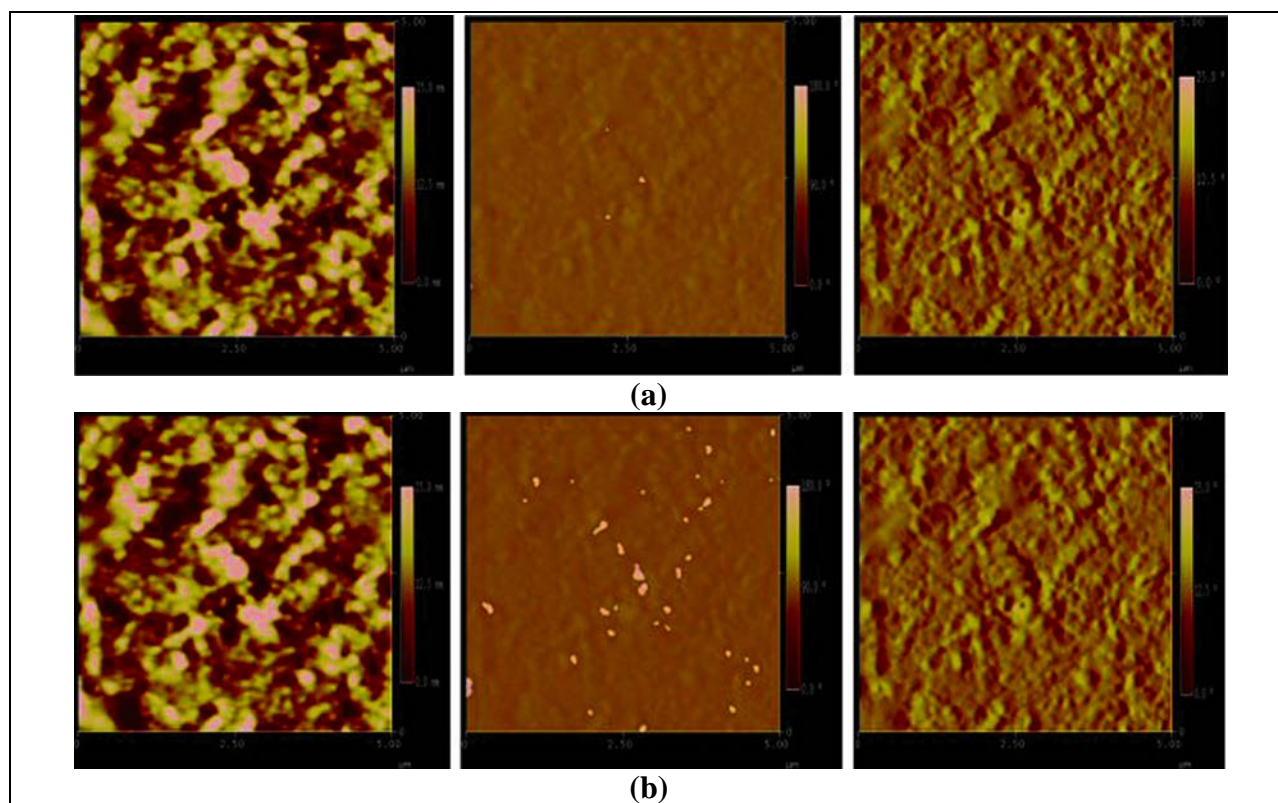


Figure 19. TappingMode Topography (left), Electric Force Microscopy (center) and Phase Images (right) with DC biases of (a) 5.5 V and (b) 6.0 V applied to the AFM tip.

The phase component of the Electric Field is observed over a 5 micron x 5 micron region in the center of the image.

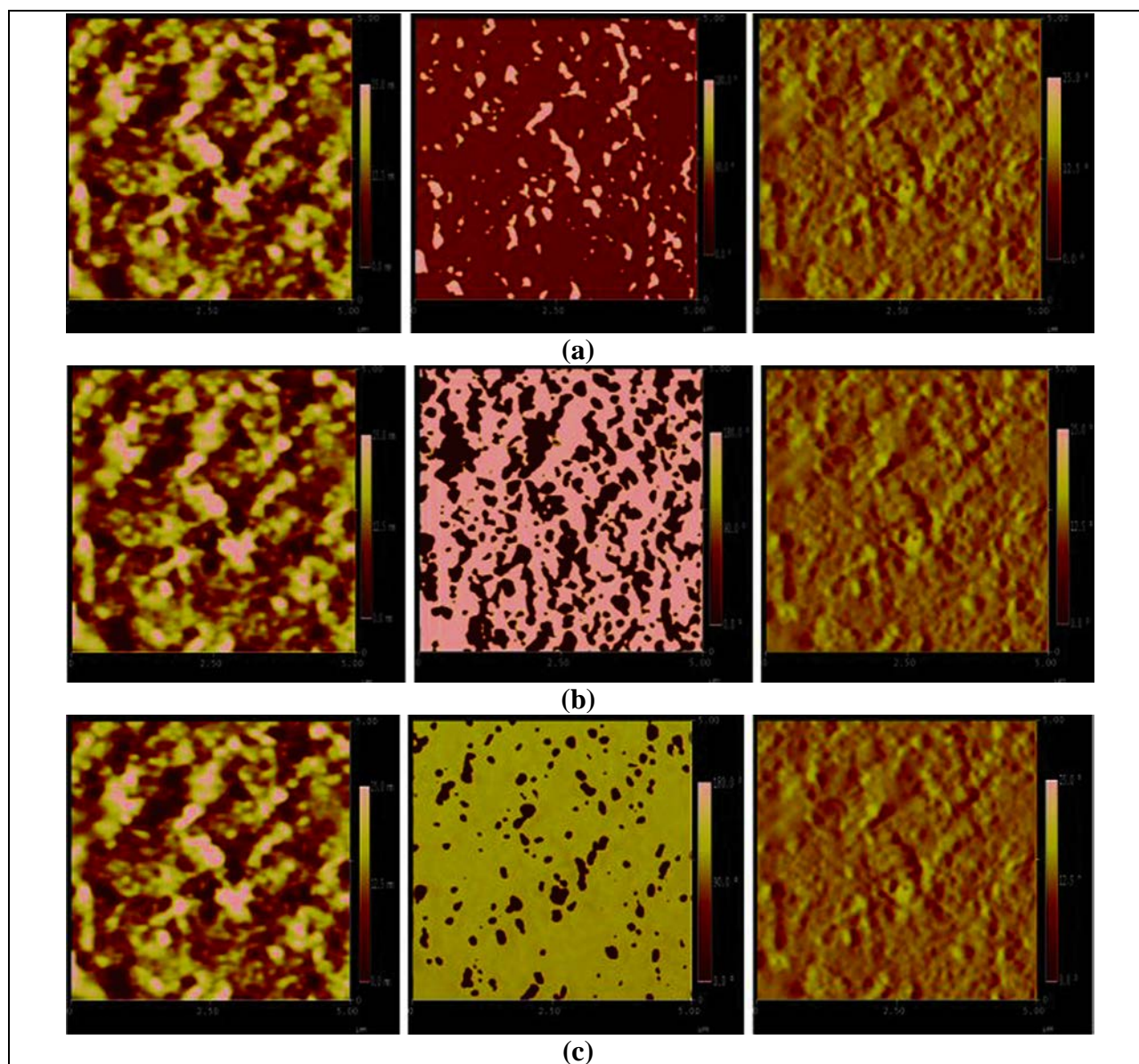


Figure 20. TappingMode Topography (left), Electric Force Microscopy (center) and Phase Images (right) with DC biases of (a) 6.5 V, (b) 7.0 V and (c) 7.5 V applied to the AFM tip.

The phase component of the Electric Field is observed over a 5 micron x 5 micron region in the center of the image.

The phase component of the electric field is mapped in the center images and shows a dramatic increase in the phase of the electric field from 5.5 to 7.0 V, and then decreases from 7.0 to 7.5 V. As the bias applied to the AFM tip increases from 5.5 to 7.0 V, the EFM images show that the phase increases. This increase in phase is due to an increase in the attractive force between the sample and the AFM tip that causes the resonant frequency to decrease. As the voltage on the AFM tip increases from 7.0 to 7.5 V, the EFM images show that the phase decreases, which corresponds to an increase in the resonant frequency of the AFM tip. This change in the direction of the phase is caused by a change in the effective dipole moment in the DNA-CTMA layer which

is seen as a decrease in the relative dielectric constant in the original S parameter measurements on the capacitive test structure made with the DNA-CTMA thin film.

1.5 DC Resistivity Studies

1.5.1. Introduction

The application of the biopolymer deoxyribonucleic acid (DNA) derived from salmon waste products⁽⁸⁹⁾ has spawned research investigations and proof-of-principle development of DNA-based biotronic specimens⁽⁴³⁾. This molecule, with its helical symmetric strands, huge range of possible base pair sequences and the large range of possible molecular weights (from <100 kDa to >8000 kDa, (where Da = Dalton, the unit of molecular weight in grams/mol), has challenged efforts to use it in designing and fabricating electro-optic⁽⁵²⁾, photonic^(48, 87) and electronic specimens^(30, 64). The key to success in these efforts is the availability of detailed data on the electrical^(81, 77), electro-optical and optical properties^(84, 72) of this material. This Section reports studies on the volume dc electrical resistivities of DNA-CTMA in comparison to common non-biopolymers⁽⁸¹⁾. The dc resistivity behaviors of DNA-CTMA films doped with conductive additives and of two silk fibroin biopolymers prepared by different processing procedures are included. Additionally, the quantitative dependence of DNA-CTMA conductivity on molecular weight is presented and discussed in detail.

1.5.2 Measurement Technique

Most of the DNA used in this work (see Section 1.2) was processed with high energy sonication to obtain molecular weights from 200 to 1000 kDa from the as-received level of >8000 kDa (see Section 1.2.1 and Heckman 2005). The DNA was then made water insoluble by treating it with the cationic surfactant hexacetyltrimethyl-ammonium chloride (CTMA) that attaches to the helical strands in place of the Na⁺ counter cations, which remain after the various processing steps that extract the DNA from the starting waste material. The resulting material, DNA-CTMA, is dissolved in butanol and spin coated typically on half glass-slide substrates wherein the solution viscosity, solution and substrate temperatures, and spin parameters determine the film thickness and uniformity (see Section 1.2.3). Uniform films of thickness ranging from ~100 nm to over 10 μ m have been made. Typical resistivity measurements use film thickness, t , between 1.5 and 5 μ m with measurements made at ~1.5 V/ μ m. DNA-CTMA films with $t \leq 1$ μ m often result in electrical shorts between the gold electrodes used for the measurements. Film thickness is measured using a Veeco 6M Dektak profiler.

Two electrode configurations shown in Figure 21 are used to measure the volume resistivity. The initial design had an electrode diameter, $D = 12$ mm and included a guard electrode, which later was found unnecessary. (Note: The 12-mm diameter design with guard electrode greatly increased the number of substrates with shorted electrodes apparently due to the large electrode areas.

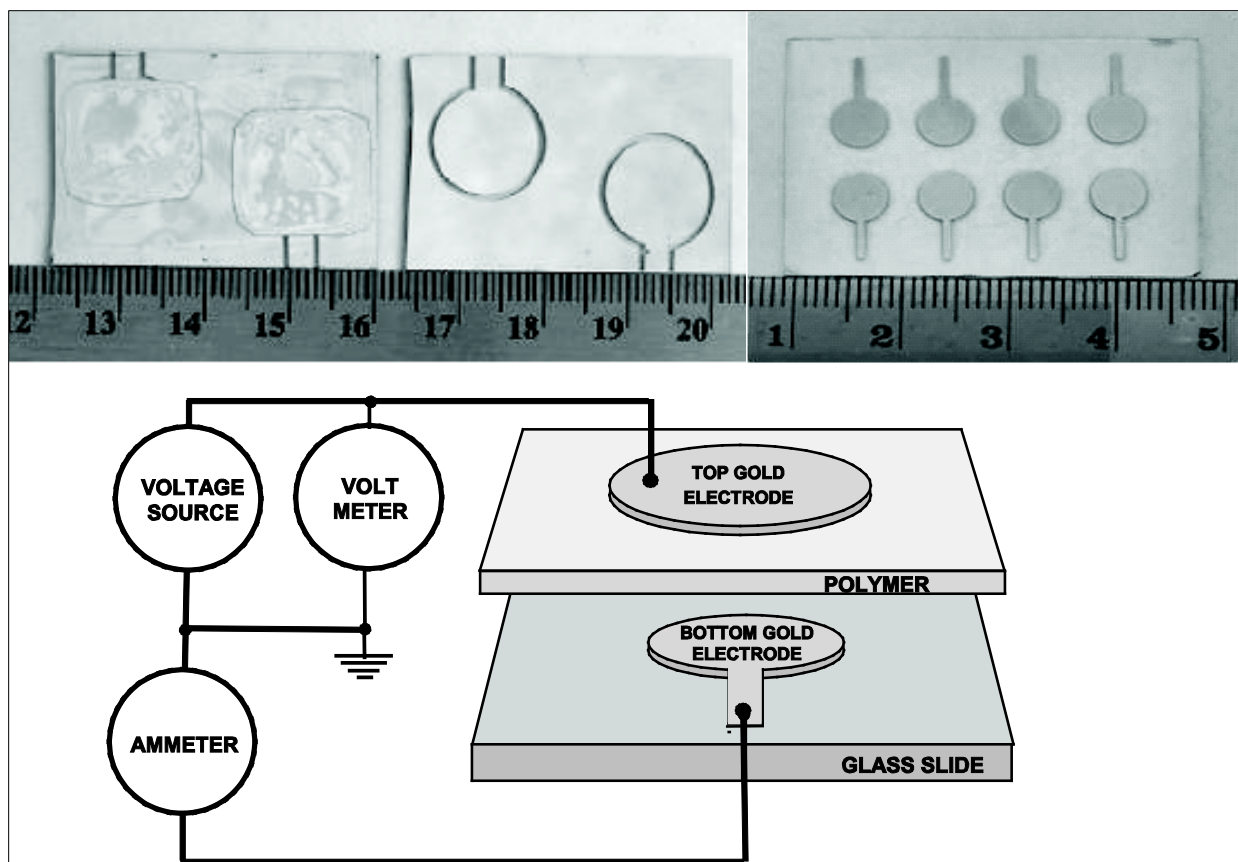


Figure 21. Electrode patterns of 12 and 5 mm dia., and the schematic of the circuit used for volume resistivity measurements.

The guard electrode was found unnecessary, especially since the diameter-to-thickness ratio is typically > 1600 . Because the spin-coated polymer fills the gap between the guarded and guard electrodes, surface resistivity measurements were not possible as originally intended.) The current design has eight $D = 5$ mm electrode pairs or “devices,” which increases the likelihood of having a device that is not shorted for a given spin-coated substrate. The 12 mm specimen is preferred for specimens having very high room temperature resistivity ($> 10^{15}$ ohm-cm), because of the increased electrode area, which reduces the measured resistance.

We use gold electrodes (50-80 nm thick) as shown in Figure 21 in order to minimize any chemical bonding at the electrode-polymer interface, which are usually applied by electron-gun-plasma deposition. A 10-nm chromium layer is deposited first for the bottom electrode followed by a 50 nm-gold layer. The chromium insures firm bonding of the gold to the substrate. Contact to the electrodes use micro-manipulated 12 μ m titanium probes. For the top electrode deposited on the film, which is slightly larger than the bottom electrode on the substrate, we use a small convex brass pad under the titanium probe. These pads prevent damage to the underlying film that can be caused by the bare probes. Since typically $D/t > 1000$, the fringing of the electric field is negligible.

The resistivity specimens are basically capacitors, and therefore, can pick up electrical charge, which polarizes the film. This quasi-static polarization in high resistivity materials decays very

slowly. Thus, when a voltage is applied to these specimens, the observed current does not initially behave in a simple manner due to the electrical history of the film. Typically, a decaying current dependent on the applied voltage plus a current that is independent of the applied voltage are seen. The latter is called a “background” current. The voltage-dependent current must either be nearly constant (with constant applied voltage) or decay exponentially converging to a stable value in order to obtain a viable resistance measurement. The behavior of these currents depends very much on the particular polymer being measured and the specimen temperature. Following the recommendation of the Keithley White Paper⁽³⁴⁾, we use the alternating polarity technique to obtain a measurement, where the voltage-dependent current converges to a within a few percent of constancy, the “background” current is minimized and the temperature is constant.

Basically, the applied voltage source in Figure 21 is a square wave of period T with equal amplitudes in the positive and negative half cycles. The presence of background currents introduce systematic errors and noise when computing the resistance by measuring the current i_T with a voltage V applied to the specimen. Averaging a running measurement of the current over a period of time cannot remove a systematic shift. However, the alternating polarity technique for resistance measurements removes the contributions of the background current and provides a convenient method for obtaining reproducible results. By an averaging procedure, any uniformly decaying background current can be canceled out to second order. An equivalent circuit for the measurement set up is shown in Figure 22(a).

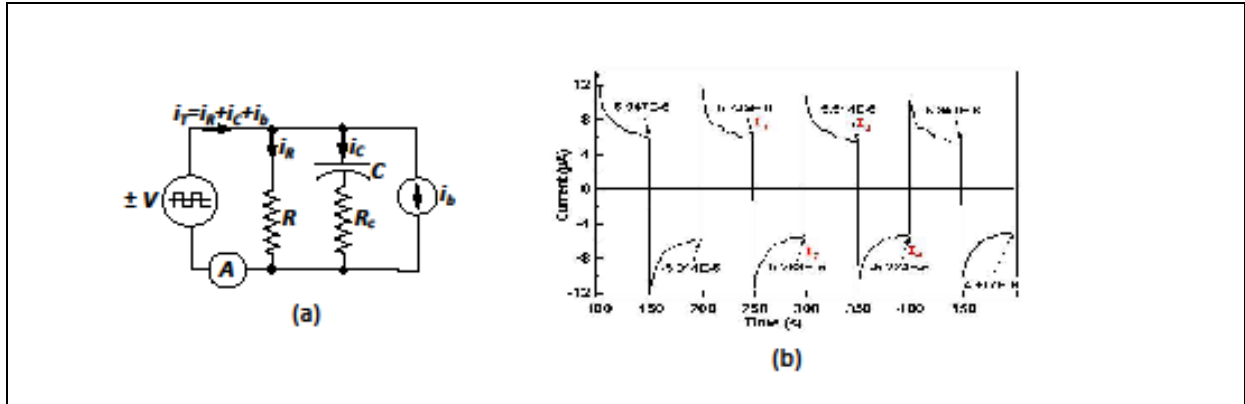


Figure 22. (a) Equivalent circuit for resistivity measurement, where V is the applied alternating potential, i_R is the dc leakage current due to the volume resistance R of the polymer specimen, i_C is the charging/discharging current through C with time constant $\tau_C = R_C C$ of the electrode- polymer- electrode sandwich connected to the measuring circuit and i_b is the polymer “background” current. (b) Typical alternating polarity (± 5 V) data taken on a 3.52 μm -thick, cross-linked, water-insoluble DNA polymer film at 100°C .

Assuming that the decay of the background current can be reasonably approximated by an exponential decay, the total current, i_T , can be written

$$i_T = V/R + i_{C0}e^{-t/\tau_C} + i_{b0}e^{-t/\tau_b}, \quad (9)$$

where V/R is the dc leakage current due to the specimen volume resistance R , i_{C0} is the peak transient current due to the charging of the capacitance C of the specimen, which decays with time

constant $\tau = R_C C$ due to the effective resistance R_C “seen” by C in the measurement circuit, i_{b0} is the initial background current with effective background decay time constant τ and t is measured from the beginning of each half cycle. Taking the Taylor series expansion of the background decay term in Equation 8 to second order and averaging appropriately the end currents for $t = T/2$ at four successive half cycles starting with a positive half-cycle, these decay terms can be canceled out to second order. It is observed that this should start after the first complete cycle, because the first current cycle is typically highly asymmetrical due to the response of the specimen to the initial application of the applied voltage and any initial charge. Starting with a positive half cycle and referring to Figure 22b, this simple averaging process over four successive half cycles is given by

$$\frac{1}{2} \left\{ \frac{1}{2} \left[\frac{I_1 - I_2}{2} + \frac{-I_2 + I_3}{2} \right] + \frac{1}{2} \left[\frac{-I_2 + I_3}{2} + \frac{I_3 - I_4}{2} \right] \right\} = \frac{I_1 - 3(I_2) + 3(I_3) - I_4}{8}, \quad (10)$$

where I_1 and I_3 are the final currents of two consecutive positive half-cycles and I_2 and I_4 are the final (algebraic) currents of the two consecutive negative half cycles that follow the above positive half cycles as illustrated in Figure 22(b). This calculation can be done for any four consecutive half-cycles that start with a positive half-cycle; however, for the cancellation to be complete, the time durations of the half-cycles must be equal to within 0.1% ⁽³⁴⁾. For example, from Figure 22(b), which does not show the first cycle, three values of resistivity are obtained, namely 2.64E9 $\Omega \cdot \text{cm}$, 2.80E9 $\Omega \cdot \text{cm}$ and 2.89E9 $\Omega \cdot \text{cm}$ starting with the first positive value for $I_1 = 5.947\text{E-}6$ A. These data illustrate typical convergence of the resistivity as later cycles are analyzed. The degree of convergence is determined by the choice of cycle duration and the behavior of the material. The 100 s duration used in Figure 22(b) usually gives better than 5% convergence after five full cycles. The length and the number of cycles used for a resistance measurement are set such that the resultant resistance shows acceptable convergence. At room temperature, we use five 100-second cycles. At temperatures typically over 50°C, when the resistivity decreases by ~100 times due to Arrhenius behavior, it is then possible to reduce to four 80-second or shorter cycles. It should be noted that these are static measurements, where the temperature is held constant during the entire data acquisition time period.

The voltage square wave, the current and voltage measurements, temperature control, resistivity calculations and data recording are accomplished with a LabView program controlling a Keithley Model 617 Electrometer and a Watlow F4 temperature controller connected to a custom-designed hotplate inside a dry-nitrogen-purged, electrostatically shielded chamber. The hot plate temperature is held constant to within $\pm 0.1^\circ\text{C}$. This is a special hotplate that has temperature uniformity over its 8” diameter of less than $\pm 1^\circ\text{C}$. There are five thermocouples that monitor the temperature. All thermocouples are mounted with high temperature, thermally conductive paste in holes in the bottom of the hot plate that places the junctions within ~ 1 mm of the hot plate top surface with the center thermocouple connected to the controller. The hotplate and adequate lengths of the thermocouples are mounted inside a tight fitting Teflon “box” around the sides and bottom. Precisely-controlled temperature is essential since the resistivity can change over four orders of magnitude between 20 and 90°C. The specimens to be measured are vacuum dried at ~35°C typically for more than 24 hrs immediately following curing and then measured in a flowing dry nitrogen gas environment with a measured humidity of 0.0%. If the specimen is exposed to air after curing for a day or more, then the specimen often needs to be dried for several days before measuring. These procedures were found to be absolutely necessary for reproducible

measurements, especially with the biopolymers. The electrometer is operated in the V/I resistance mode that permits the choice of an applied voltage that is sufficient to produce accurately measureable current levels while avoiding shorting events between the electrodes. Measurements usually start at $\sim 20^{\circ}\text{C}$, but in some cases a temperature as low as 15°C was obtained with the cold water flowing through the hot plate cooling coils. Maximum temperature was typically 90°C , but some polymers were taken to higher temperatures with no discernable damage.

1.5.3 Data Analysis

The direct current conduction through insulating polymers takes place by ionic, electronic or by polarons, or some combination of these mechanisms⁽⁷³⁾. Ionic conduction typically requires impurities or defects, which create ion vacancies, unattached ions or weakly-attached ions. Electronic transport processes involve electrons or holes, or both, and require some distribution of acceptor and/or donor states. These processes take place by “hopping” mechanisms in which electrons or holes hop between localized sites and drift towards the appropriate electrode in an applied field. In DNA, it has been proposed that the double helix with a random base pair sequence can be viewed as a 1D disordered system. The disorder leads to electronic localization, and electron/hole hoppings between these localized “impurity” sites along the chain are responsible for the conductivity⁽⁸⁶⁾.

There have been a great many studies of charge transfer in DNA molecules^(38, 67, 39, 85, 45, 33, 63). The current view of charge transport in DNA is by electron vacancies or holes, which form polarons⁽⁷⁵⁾. This mechanism is seen as rapid and efficient by virtue of a channel formed by the overlapping π orbitals of the base pairs that provide a means for charge migration of the injected holes in the DNA molecule⁽⁷⁸⁾. A hole is expected to quickly localize at the nearest guanine radical cation, since the oxidation potential of a guanine site is the lowest in DNA⁽⁸⁰⁾. This localized charge cloud is called a polaron and can extend over a few base pairs. The hole or polaron then becomes mobile by the transport of an electron from a distant G residue to the cation site, which can occur over distances >20 nm. Although there are reported differences in the hole transfer rates between guanine-cytosine (GC) bases, called G hopping, and between adenine-thymine (AT) bases, called A hopping, as well as single-step tunneling, which impact the limiting charge mobility, the transport range is almost unlimited. The main limit to the range is suggested to be chemical reaction with water, presumably in the grooves of the DNA molecule, which limits the range to distances less than $5\text{ }\mu\text{m}$ ⁽⁶⁰⁾. Since the as-received salmon Na-DNA used in this work has a molecular weight of >8000 kDa for which the length is $>4.1\text{ }\mu\text{m}$, then charge transport can likely take place over the entire length of the molecule. By comparison, 1000 kDa sonicated DNA has a length of $0.51\text{ }\mu\text{m}$. Going one step further, 200 kDa DNA has a length of only 103 nm, which shows the importance of molecular weight in characterizing DNA-based materials.

In the work presented here, however, the DNA materials studied were in the form of micron-size films deposited on glass or on an oxidized silicon wafer by spin casting or drop casting from either organic solvent or aqueous solutions, cured and thoroughly dried. There was no effort to control the orientation of the DNA molecules and, as such, there will be some random distribution of orientations and “coiling” or non-straight conformations in a given film. Thus, it is evident that the observed dc conduction mechanism in these films includes both the conduction in or through the DNA molecules and between the DNA molecules. The statistical distribution of molecule

orientation in micron-size films can be expected to depend on the molecule lengths. For example, the $>4.1 \mu\text{m}$ as-received Na-DNA formed into a $1.56 \mu\text{m}$ film can be expected to have the helix axes of a large fraction of the DNA molecules predominately parallel, or nearly so, to the plane of the substrate, and hence, to the electrodes.

Theoretical and experimental studies of the polaron conduction mechanism in the DNA molecule have shown the polaron mobility to be high (for a polymer), ranging from 0.04 to $4.5 \text{ cm}^2/\text{V}\cdot\text{s}$ ^(45, 60, 33). We have carried out preliminary studies of the charge transport mobility in our DNA-CTMA and as-received DNA films using the photoconductive time-of-flight technique ⁽⁷³⁾. We found only hole carriers with mobilities $\mu_H \sim 1\text{E-}6 \text{ cm}^2/\text{V}\cdot\text{s}$. In addition, our resistivity studies show a clear dependence on molecular weight from the as-received value of $>8000 \text{ kDa}$ to 200 kDa . Since conductivity is proportional to mobility, this leads us to hypothesize that the charge transport through the micron-size DNA films is dependent primarily on the transport *between* the molecules. If this holds true, then it is reasonable to expect that the charge transport along the helix axis is different than perpendicular to the axis. This expectation appears to be supported by computations of mobility through and across a GC sequence that show the mobility perpendicular to the helix axis is 30 times smaller than along the axis ⁽⁶³⁾. Since the Raman spectra of DNA(sonicated)-CTMA showed no dependence on molecular weight ⁽⁸²⁾, then it is assumed that the observed conductivities of micron-size films of sonicated DNA depend on the statistical distributions of the molecule orientations. These distributions in the thin films used in this work can be expected to be constrained to some degree by the length of the molecules, which is a directly proportional to the molecular weight. Although the attached CTMA surfactants enlarge the physical extent of the DNA molecules, this hypothesis should still apply to DNA-CTMA films, which has been at the center of our resistivity measurements. More experiments and detailed modeling are needed to confirm this hypothesis. Implicit in this discussion is that the mechanism of the observed conductivity in these micron-size films is not ionic. It is not evident that conductivity would depend on molecular weight if ionic transport was the operative mechanism.

It has been found that above some corner or cross-over temperature T_c the conductivity of DNA ^(37, 59, 84) is described by the Arrhenius ansatz given by

$$\sigma = \sigma_0 e^{-(E_a/kT)}, \quad (11)$$

where the exponential prefactor σ_0 depends on the number density of the sites involved in the transport ⁽³¹⁾, E_a is the activation energy, k is the Boltzmann constant and T is the Kelvin temperature. This region is due to nearest neighbor hopping. At temperatures below T_c , charge transfer is described as due to variable range hopping and leads to a weaker dependence on temperature than given in Equation 11. This variable-range hopping model is given by

$$\sigma(T) = \sigma_0 e^{-(T_0/T)^\beta}, \quad (12)$$

where T_0 is a constant and, typically, $\beta = 1/2$ or $1/4$ ^(31, 86, 36), which is often too strong to describe the observed temperature dependence below T_c . Measurements of Li-DNA conductivity down to temperatures $\sim -53^\circ \text{C}$ have shown that a useful empirical model is given by ⁽⁵⁹⁾

$$\sigma(T) = \sigma_B + \sigma_0 e^{-(E_a/kT)}, \quad (13)$$

where σ_B is a constant resistivity at temperatures below the empirical corner or crossover temperature T_c defined as ⁽⁸³⁾

$$T_c = \frac{Ea}{-k \ln(\sigma_B/\sigma_0)} \quad (14)$$

which is the temperature given by Equation 13 at which the generalized Arrhenius function equals σ_B . A graphical representation of this “corner” or “crossover” temperature is given in Figure 23. Kutnjak et al. were able to fit a portion of their data from measurements on Li-DNA to Equation 12 for $\beta = 1/2$.

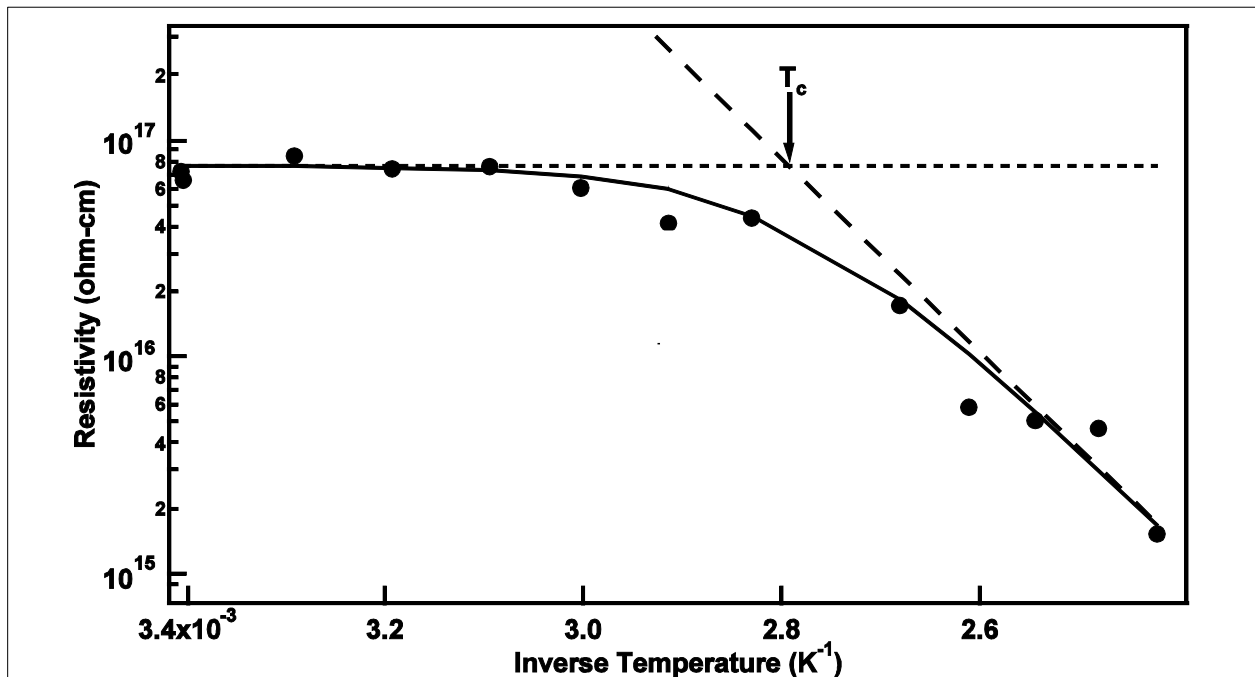


Figure 23. Illustration of the corner temperature, T_c , using the APC data from Figure 24.

The dotted line is σ_B and the dashed line is the Arrhenius term.

The thrust of these studies was to characterize the temperature behaviors of the resistivity of both as-received DNA and DNA-based films, including as a function of the mean molecular weight, and compare to the behaviors of selected oil-derived insulating polymers. The alternating polarity technique was used to measure the resistivity ρ and characterize the behaviors by fitting Equation 13 to the data using the conductivity $\sigma = 1/\rho$. The resistivity is computed from the measured resistance R by $\rho = \pi R D^2 / 4t$, where D is the bottom electrode diameter and t is the mean thickness measured from the tab across D (see Figure 21).

The analysis and graphing program Igor Pro was used to fit Equation 13 to the data, which often required some experimentation to be successful for a given data set. The σ_B term was needed for all the data sets consistent with Kutnjak et al. ⁽⁵⁹⁾. It was found that only the conductivity form of

the data could be consistently fitted. Efforts to fit Equation 12 with $\beta < 1$ to data having high T_c were not successful. The long measurement time needed to reach a reasonable convergence for each data point using the alternating polarity technique made it difficult to automate the measurements or to acquire a large number of points for every specimen. Nevertheless, the resulting parameter values give evidence of adequate characterization of the studied materials.

1.5.4. DATA

1.5.4.1 DNA compared to non-biopolymers

The as-received DNA has molecular weight >8000 kDa. Solutions using this DNA can have high viscosity, which are difficult to spin coat and can give uneven films when drop cast. Lower viscosity can be obtained by reducing the molecular weight using a high power sonication probe (see Section 1.2.1), which gives mean molecular weights down to ~ 200 kDa. (Note: The term “mean” molecular weight is the maximum of the assumed symmetrical molecular weight distributions obtained from agarose gel electrophoresis measurements. A more precise characterization might be the “peak” molecular weight. See Figure 1). This is followed by exchanging the surfactant CTMA⁺ for the Na⁺ counter ion on the DNA resulting in hydrophobic DNA-CTMA. The sonication, however, produces broad distributions of molecular weight, typically $\pm 50\%$ or more, which means the distinctiveness of the measurements on films with different mean molecular weights could be somewhat compromised. Measurements were made on many DNA(sonicated)-CTMA films with mean molecular weights ranging from 200 to 1000 kDa. In addition, unsonicated, as-received DNA and as-received-DNA with CTMA were studied. The former is water soluble, which is more of a challenge to produce as a uniform film by spinning or drop casting. A summary of these studies on DNA materials are given in Figure 24. The fits of the Arrhenius function plus a constant, Equation 13, to the conductivity data, from which the fitting parameters given in Table 3 were obtained, are given as resistivity and shown as solid curves in the figure. These data are given in units of ohms-cm rather than siemens/m, because resistance is more useful for device design when the conductivity is very low. The data are plotted with the inverse temperature increasing to the left in order to show the Celsius temperature behavior increasing to the right. The Celsius scale is shown at the top of each graph. This method of plotting with a logarithmic ordinate clearly shows the Arrhenius temperature dependencies of the resistivities.

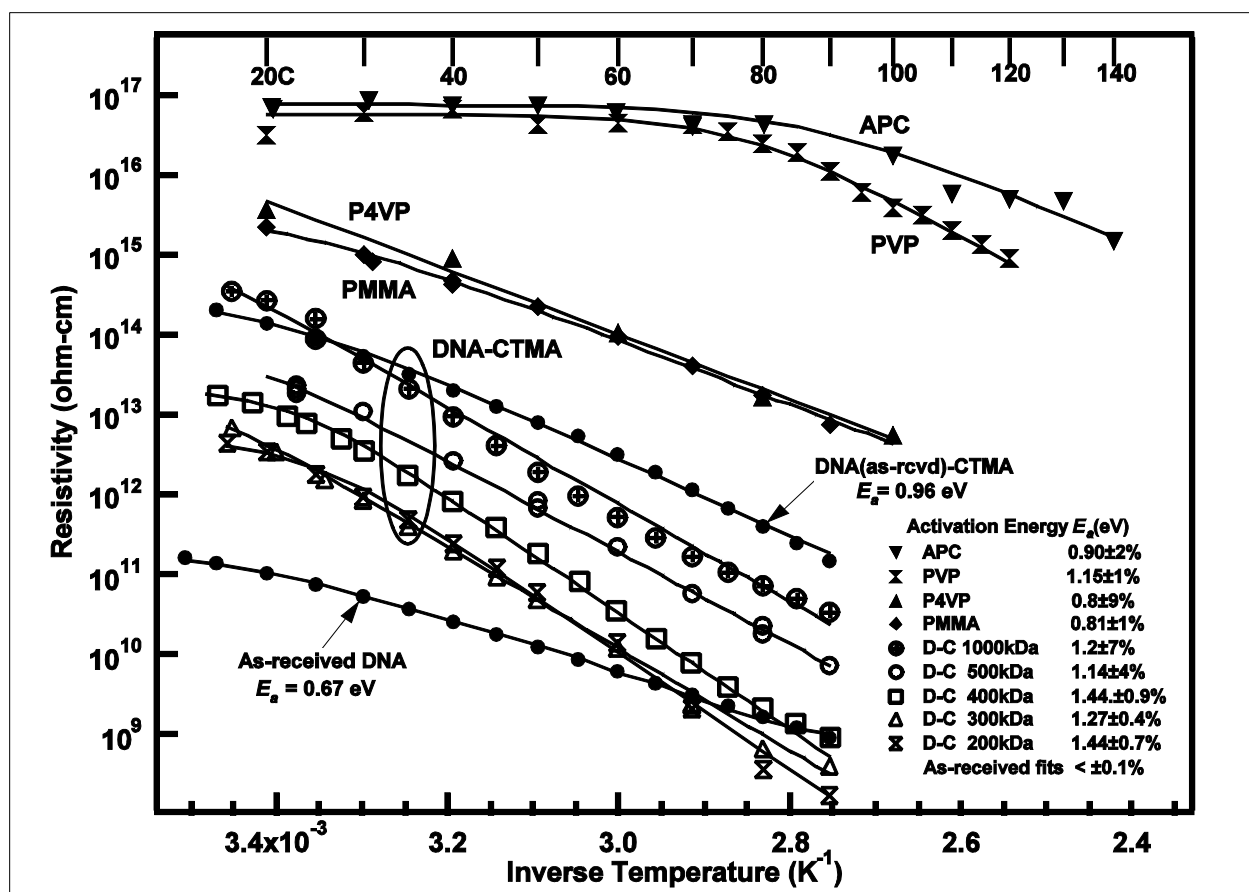


Figure 24. Resistivities of DNA-based films and selected non-DNA polymer films.

Solid curves are fits of Equation 11 to the data. Fitting parameters are in Table 3. Note the Celsius scale at the top of the graph.

The data show that processing as-received DNA with CTMA increases the activation energy from 0.67 to 0.96 eV and sonication further increases this parameter to 1.3 eV on average. In addition, there is a clear dependence of resistivity on molecular weight with little change above 1000 kDa. Likewise, there is little difference between 200 kDa and 300 kDa data. Although, the corner temperature, T_c , was computed for all the DNA plots in Figure 24, these plots did not extend to sufficiently low temperatures to allow for accurate determinations of T_c in all cases; however, for completeness these values are included in the data Table 3.

Table 3. Parameters obtained from fitting Equation 13 to the conductivity data of the measurements given in Figure 24 plus silk in Figure 26.^a

Polymer	ρ @ 20°C $\Omega\text{-cm}$	E_a eV	σ_0 $(\Omega\text{-cm})^{-1}$	σ_B $(\Omega\text{-cm})^{-1}$	T_c °C
DNA(1000 kDa)-CTMA	2.04e14	1.21±7%	2.64e6	3.0e-16	~4
DNA(500kDa)-CTMA	3.04e13	1.14±4%	9.07e5	1.0e-14	~14
DNA(400kDa)-CTMA	1.32e13	1.44±0.9%	2.08e11	4.5e-14	22
DNA(300kDa)-CTMA	4.17e12	1.27±0.4%	1.16e9	4.0e-14	~11
DNA(200kDa)-CTMA	3.32e12	1.44±0.7%	5.38e11	2.0e-13	24
DNA(>8000kDa)-CTMA	1.41e14	0.96±0.1%	1.03e2	3.3e-15	19
DNA(>8000kDa)	1.04e11	0.67±0.1%	2.23	3.0e-12	~12
Tufts' Silk	1.92e12	0.62±5%	3.5e-4	5.1e-13	79
APC	8.0e16	0.90±2%	5.88e-5	7.6e16	86
PVP	5.4e16	1.15±1%	0.738	5.4e16	76
P4VP	4.7e15	0.8±9%	4.64e-2	~2e16	~10
PMMA	1.9e15	0.81±1%	1.88e-2	3.9e15	20

^a $\Omega\text{-m} = 0.01 \Omega\text{-cm}$; $\text{siemens/m} = 100 (\Omega\text{-cm})^{-1}$

The sonication procedure typically involves a periodic series of high energy ultrasonic pulses separated by cooling periods. This is done typically for 30 min with the total sonic energies up to 200 kJ (see Section 1.2.1). In an effort to determine the impact of continuous sonication on resistivity, a cooled batch of DNA was sonicated without pulsing for 30 min with occasional interruptions for cooling to give a mean molecular weight of ~200 kDa. Although there was much debris in the solution, most was removed by filtering and a resistivity device was fabricated and measured. The data are given in Figure 25 with pulsed-sonicated DNA(200kDa)-CTMA shown for comparison. This is the first data set for which it was necessary to include a linear term in Equation 13 to achieve a quality fit. As can be seen in Figure 25, the fit is perfect to the eye with $E_a = 1.06 \text{ eV} \pm 0.6\%$. Moreover the resistivity increased by nearly four orders of magnitude compared to the pulse-sonicated DNA. Micro-Raman spectroscopy studies were carried out on DNA(sonicated)-CTMA and on as-received Na-DNA⁽⁸²⁾ which showed that the former is B-form DNA independent of the sonicated molecular weight. The Raman spectrum of the continuously sonicated DNA (Yaney 2009, unpublished) showed considerable reduction in the strengths of the vibrational modes of the bases relative to the phosphate mode, a broadening of the phosphate mode and a broad, irregular Raman band well below the base breathing modes ($<650 \text{ cm}^{-1}$) relative to the pulsed sonicated DNA. These changes suggest that the continuous sonication caused significant damage to the DNA molecules and that the DNA material was probably made partially amorphous by the sonication. The similarity of the resistivity behaviors of this heavily sonicated material to that of APC (amorphous polycarbonate, see below) cannot be ignored.

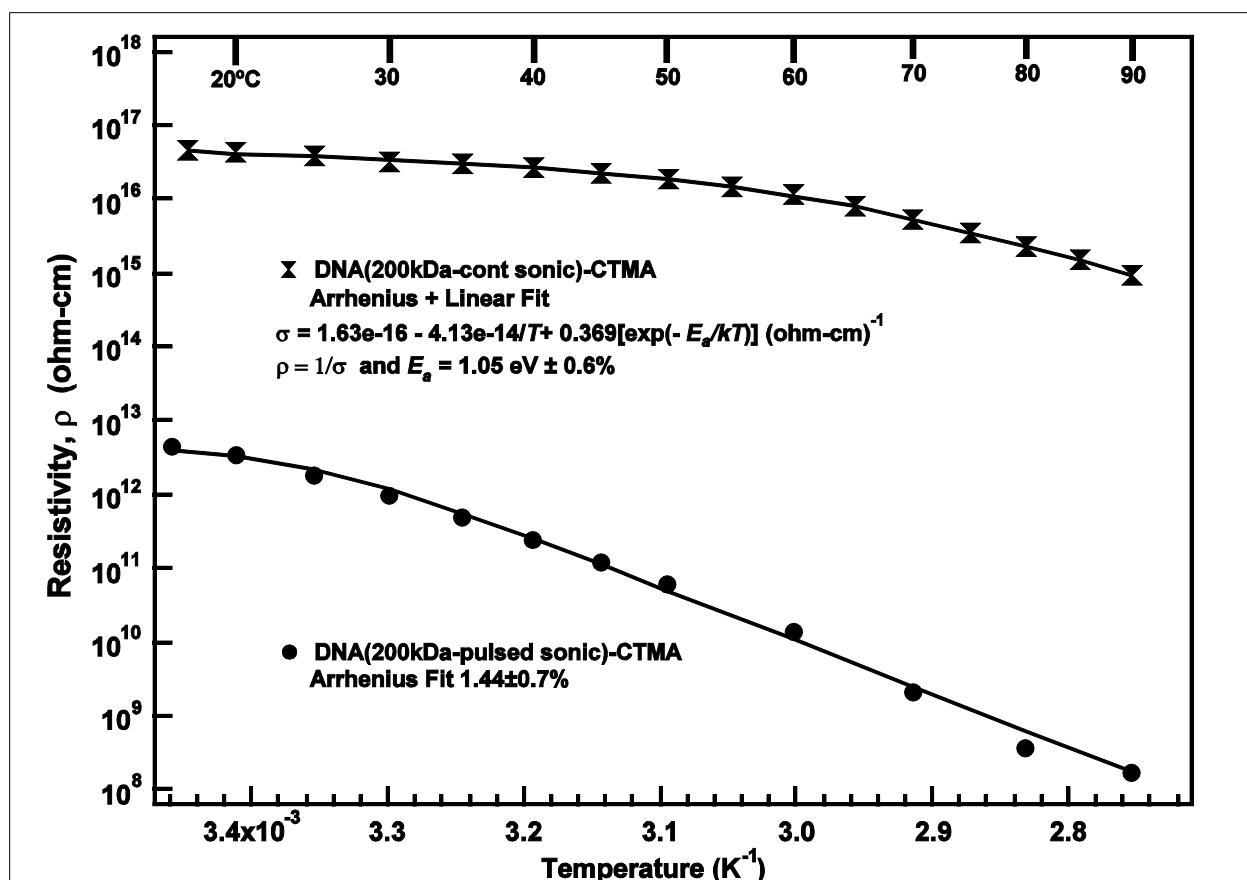


Figure 25. Resistivity of DNA(200kDa)-CTMA from continuously sonicated DNA in comparison to normal pulsed sonication.

The measurements on non-biopolymers poly[methyl methacrylate] (PMMA), amorphous polycarbonate (APC), poly 4-vinylphenol (P4VP) and poly(vinylpyrrolidone) (PVP) are also included in Figure 25 for comparison. There are three sets of data in the APC plot taken on different days. As a result, these data show more scatter, which is not unreasonable considering the extraordinary high resistivity of this polymer. Nevertheless, the three sets still follow the basic trend, confirming reasonable repeatability. The PVP, which is water soluble, also showed a very high resistivity close to APC. Both polymers are distinctive in that the onset of Arrhenius behavior occurs around $T_c = 80^\circ\text{C}$. These four high-resistivity polymers were measured with the 12-mm diameter electrodes to lower the measured resistance. Fitting parameters for these polymers are included also in Table 3.

1.5.4.2 Silk

Silk films from Tufts University⁽⁵⁶⁾ and from AFRL/RX⁽⁶⁶⁾ processed from bombyx mori silk fibroin were studied. The Tufts' films were provided on our 12-mm-dia. electrode substrates. The silk was prepared from high concentrations of regenerated silk fibroin in aqueous solution (~8 wt.%). After processing, the silk is insoluble in water. The AFRL/RX material was dissolved in an ionic liquid, processed and provided in solution form, from which we spin-coated films. The resistivity data for these two materials are given in Figure 26 and the fitting parameters for the Tufts' material are given in Table 3. Although the Tufts' silk resistivity on the scale used in the

figure appears almost independent of temperature, the data does show the onset of Arrhenius behavior at $T_c = 79^\circ\text{C}$ with activation energy of 0.62 eV, which is very close to the as-received DNA value of 0.67 eV. The silk film from AFRL/RX was initially cured at $\sim 60^\circ\text{C}$, which produced a somewhat erratic and time-dependent resistance behavior versus temperature, some of which is visible in Figure 26. Curing the specimen again, but at 90°C , gave a more smooth and stable temperature dependence. However, the material showed no Arrhenius behavior and, in fact gave a “concave up” curvature in contrast to the Tufts’ silk curve and the curves in Figure 24. The AFRL/RX silk is nearly 1000 times more resistive than the Tufts’ silk, which, if nothing else, highlights the complexity of these biopolymers and the importance of the processing techniques. The observed behavior of the AFRL/RX silk suggests weak ionic conductivity.

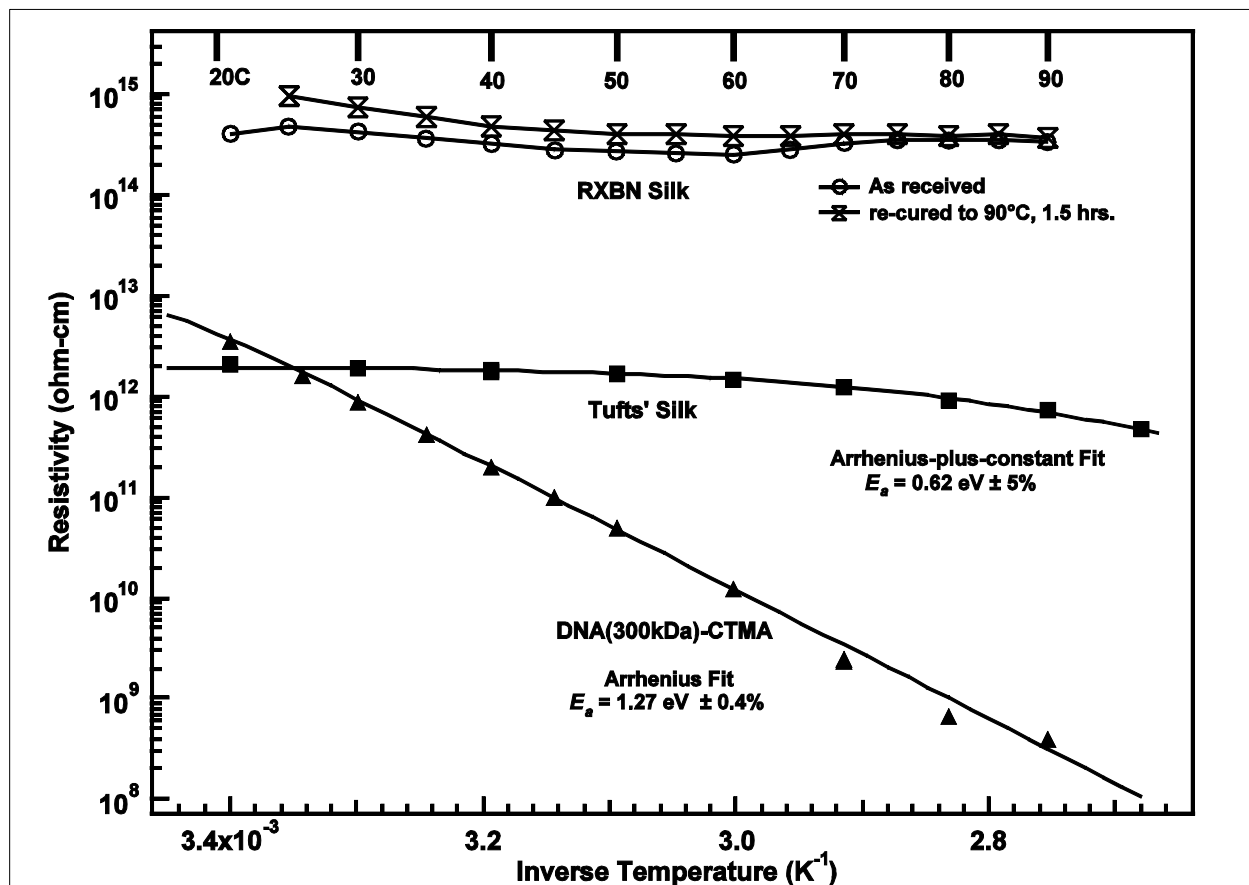


Figure 26. Resistivities of silk films compared to DNA(300kDa)-CTMA.

Solid curve for Tufts’ silk is the fit of Equation 11 to the data. The solid lines for the AFRL/RXBN data connect the points for clarity.

1.5.4.3 Effect of humidity and measurement accuracy

Enhanced conductivity, lower activation energies and/or bending of the curve in the 20 to 40°C range occur when a small amount of excess water is present, that is, when the films are not thoroughly dried. Two sets of data for each of DNA(as-rcvd) (hydrophilic) and DNA(as-rcvd)-CTMA (hydrophobic) given in Figure 27 are examples of these effects. These resistivity changes that occur when excess water is present are attributed to H^+ ions from

dissociation of the water^(46, 32). The contrast between two data sets taken on the same resistivity device given in Figure 28 is an extreme example of the long term effect of humidity when no effort was made to thoroughly dry the film. The unusual increase in resistivity due to long exposure (many weeks) to room air might be explained by water being *absorbed* into the volume of the film, which interfered with charge transport and charge injection, thus increasing the resistivity. The behaviors of the two materials in Figure 27 are more typical when either hydrophobic or hydrophilic films are exposed to humid air for about a day or are not adequately dried, wherein water is probably *adsorbed* onto the polymer molecules in the film-electrode interfacial regions. As reported by Eley and Spivey⁽³⁷⁾, the bending of the resistivity curve in the initial plot for the DNA(as-rcvd)-CTMA film near room temperature has been seen often in our DNA-CTMA studies when a film was not adequately dried.

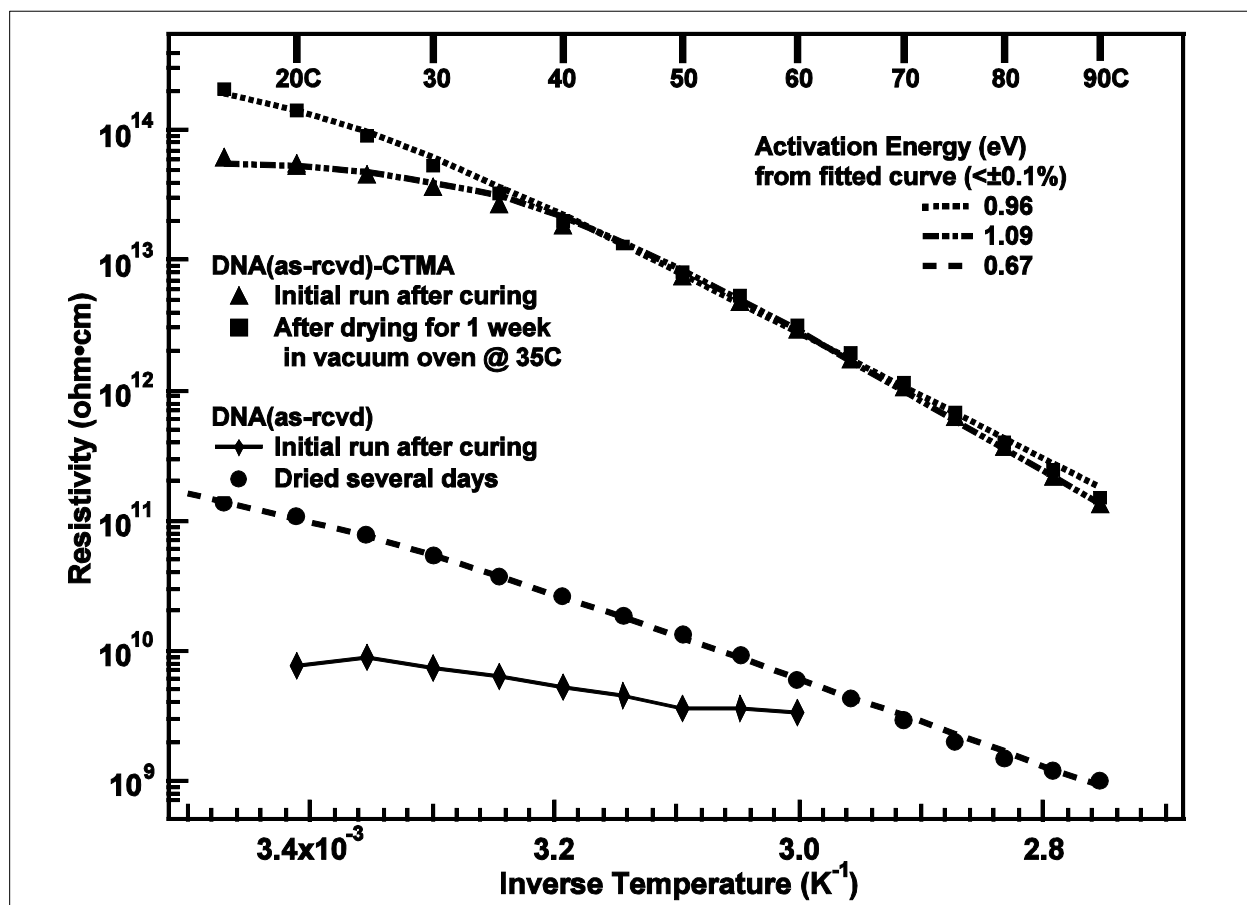


Figure 27. As-received DNA with Na⁺ counter ion and as-received DNA with CTMA⁺ replacing the Na⁺.

The effect of inadequate drying after curing the water-based as-received DNA film is shown in the lower plot.

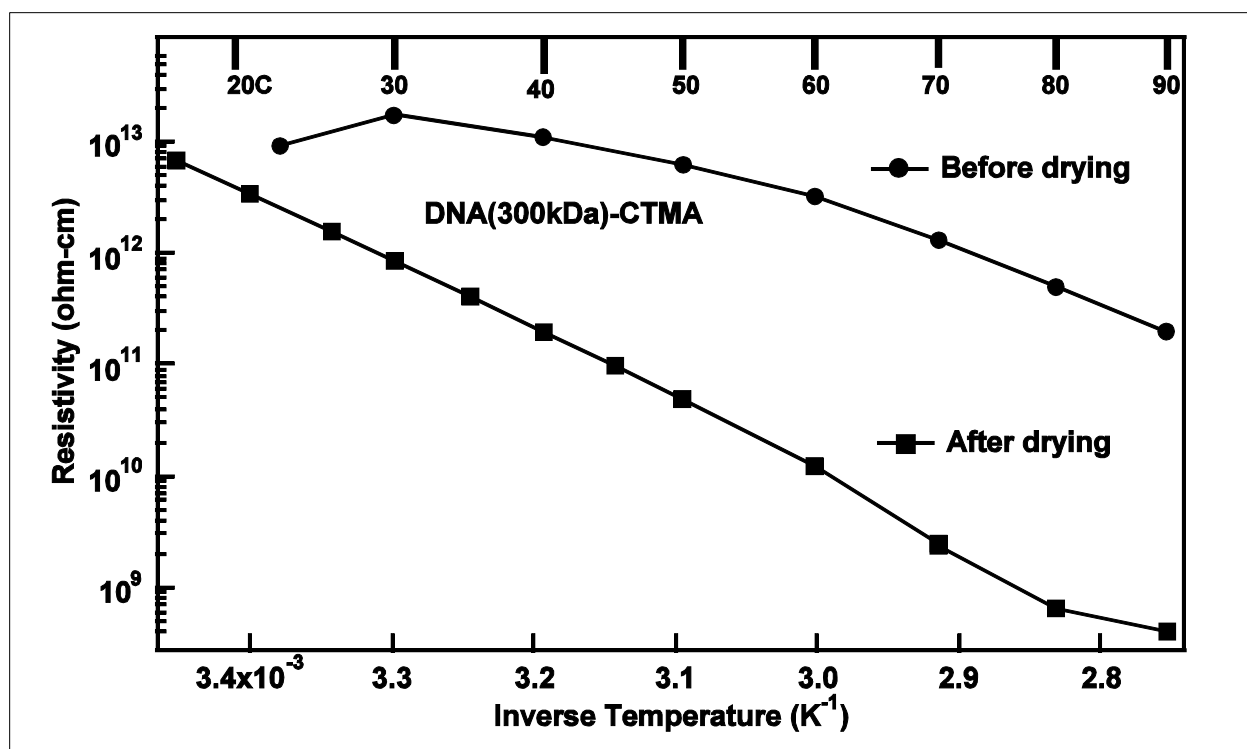


Figure 28. Effect of long-term exposure to humidity and inadequate drying on the resistivity of a DNA-CTMA film.

The lines connect the points for clarity.

The precision of these measurements is best shown by examples of reproducibility. For example, two different PMMA specimens were measured with the resulting data and the fits to the data equal to within $\pm 10\%$. Another example is DNA(500kDa)-CTMA shown in Figure 24 as D-C 500kDa. This plot has data from two separate specimens taken at different times. Some plots shown in Figure 24 show small deviations from well-defined behavior at the higher temperatures. This is probably due to changes in the polymer and/or changes in the contact (i.e., the interface) between the gold electrodes and the polymer. The accuracy of the resistivity measurements is difficult to estimate, because of material and processing issues and the lack of precise knowledge of the complete three-dimensional thickness profiles of the films; however, we estimate that the accuracies for the well-behaved data from spin-cast films are equal to or better than $\pm 20\%$ based on our ability to reproduce the measurements, and the accuracies of the Keithley electrometer and the Dektak profiler. The surface temperature of the hotplate was within $\pm 0.3^\circ\text{C}$ to the reading of a calibrated electronic surface thermometer.

1.5.4.4 DNA with conductive dopants

There are at least two ways to make materials using DNA that have significant dc conductivity, namely 1) somehow organize the DNA molecules in a lattice such that the material exhibits true semi-conducting behavior, or 2) add conducting chemicals to the DNA with the hope that they will enhance the charge transport sufficiently and/or increase the charge density to make the material useful for fabricating electronic devices such as BioFET's (see Chapter 2). The following gives a summary of our current efforts to implement method 2).

Three dopants or additives that were investigated are phenyl-C61-butyric acid methyl ester (labeled PCBM in Figure 29), polyethylenedioxythiophene-polystyrenesulfonate, PEDOT-PSS, known as Baytron P or CLEVIOS P (Baytron and CLEVIOS are registered trademarks of H. C. Starck-CLEVIOS GmbH, Goslar, Germany) (labeled BP in Figure 30), and ammonium tetrachloroplatinate ($(\text{NH}_4)_2\text{PtCl}_4$) (labeled Pt in Figure 31). The BP and Pt aqueous solutions were each mixed with sonicated DNA followed by ion exchange processing with the surfactant CTMA and then dissolved in butanol. PCBM was dissolved in chloroform prior to mixing it with DNA-CTMA in butanol. These solutions were spin coated on half glass slides with eight gold electrodes (see Figure 21), and then coated with the top gold electrodes for resistivity measurements. Figures 29-31 give the results of the measurements plus plots of non-doped DNA films for reference. The graphs are plotted with identical scales to facilitate the comparisons.

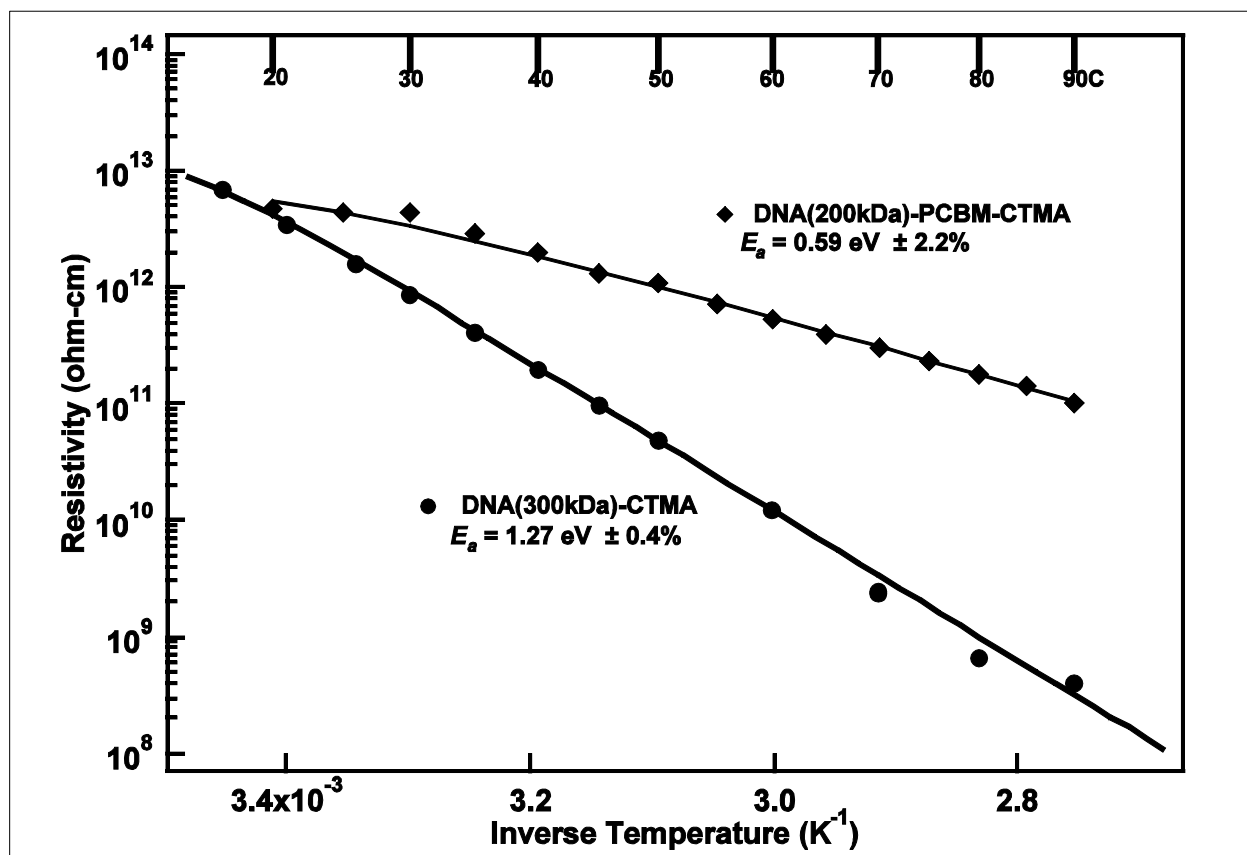


Figure 29. Behavior of DNA(200kDa) complexed with dopant PCBM before adding CTMA in comparison to DNA(200kDa)-CTMA from Figure 24.

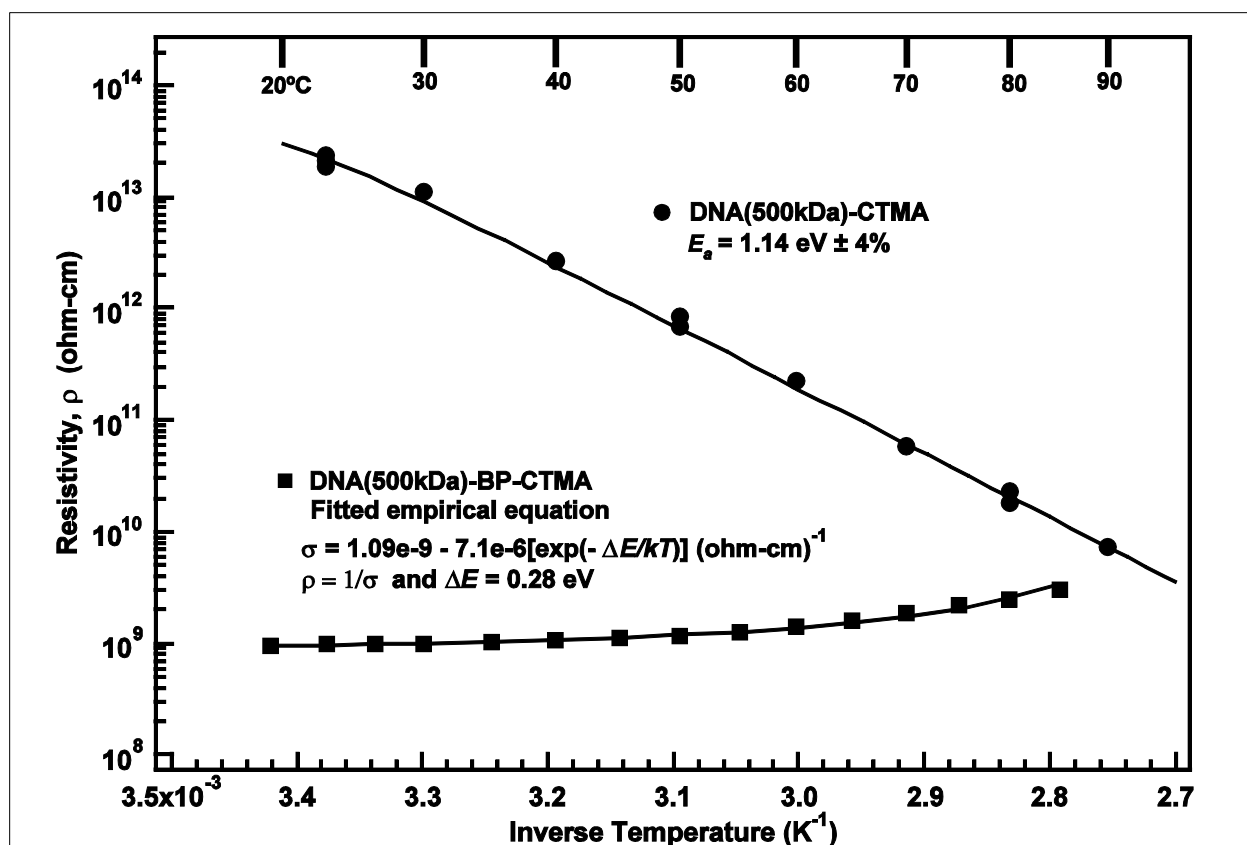


Figure 30. Behavior of DNA(500kDa) complexed with dopant BAYTRON P (from H. C. Starck-CLEVIOS) before adding CTMA in comparison to DNA(500kDa)-CTMA from Figure 24.

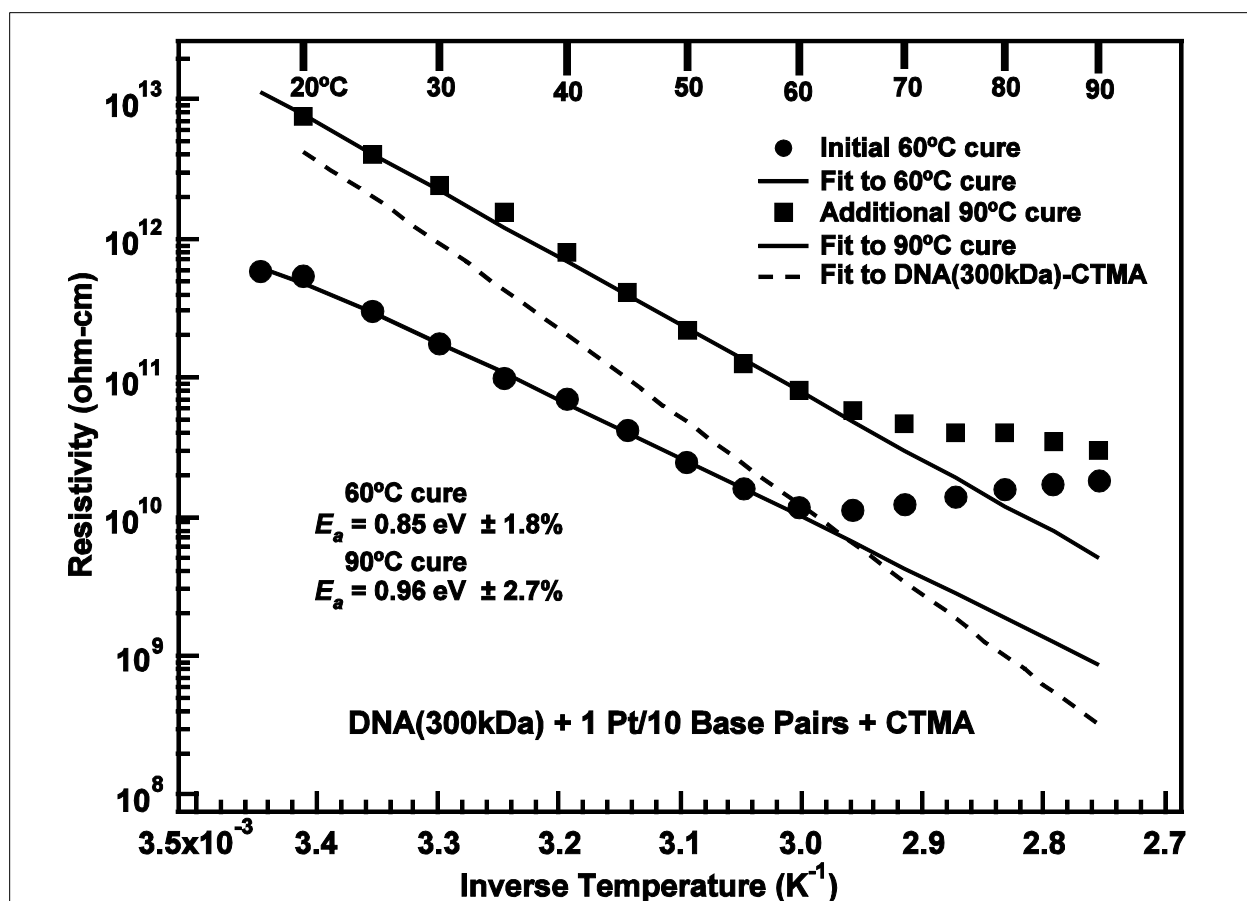


Figure 31. Behavior of DNA(300kDa) complexed with ammonium tetrachloroplatinate dopant before adding CTMA after curing at two temperatures in comparison to the fitted curve for the DNA(300kDa)-CTMA data in Figure 24.

Although the PCBM-doped data in Figure 29 showed clear Arrhenius behavior, the room temperature resistivity was only slightly lower than the non-doped material and had activation energy approximately half of the non-doped material.

In Figure 30, the BP-doped film gave over four orders of magnitude lower resistivity at room temperature. Although it shows very small temperature dependence, it did have an “inverted” Arrhenius (concave upward) behavior, which permitted fitting an empirical “inverted” Arrhenius-type function to the data as shown in the graph.

The Pt data, given in Figure 31, had Arrhenius behavior up to 60°C (negative slope), but then the resistivity plot changes to a positive slope. Initially, the specimen had been cured at 60°C, which gave resistivities lower than the non-doped material by about a factor of 10. Because of the deviation from Arrhenius behavior, the specimen was re-cured at 90°C with hope that the plot would “straighten.” As shown in Figure 31, this curing increased the resistivity, probably due to water or ammonia loss, but did not remove the break in the curve at 60°C. It was not evident what property of the material was responsible for this effect, although the behavior appears to be some sort of threshold response.

Instead of adding BP to sonicated DNA before doing the ion exchange with CTMA, a much more conductive version of BP identified as BFE (Baytron™ FE and CLEVIOS™ FE are products of H. C. Starck-CLEVIOS GmbH, Goslar, Germany) was added in increasing dopant levels to as-received DNA in aqueous solutions without complexing with CTMA and drop cast into thin films. The main objectives were to compare to DNA-BP-CTMA and to determine how the resistivity behaved with increasing amounts of BFE. It was not possible to do this kind of study using BP, presumably due to the presence of CTMA. The results are given in Figure 32, which show two to five orders of magnitude decrease in resistivity over the neat as-received DNA plotted in Figure 27. This behavior is similar to the DNA-BP-CTMA result, including little or no dependence on temperature, but the 11.9 wt% DNA-BFE resistivity was a 1000 times more conductive than DNA-BP-CTMA. This conductivity is the largest observed so far using dopants in DNA. The 5.8 wt% device was measured to 105°C to check for Arrhenius behavior.

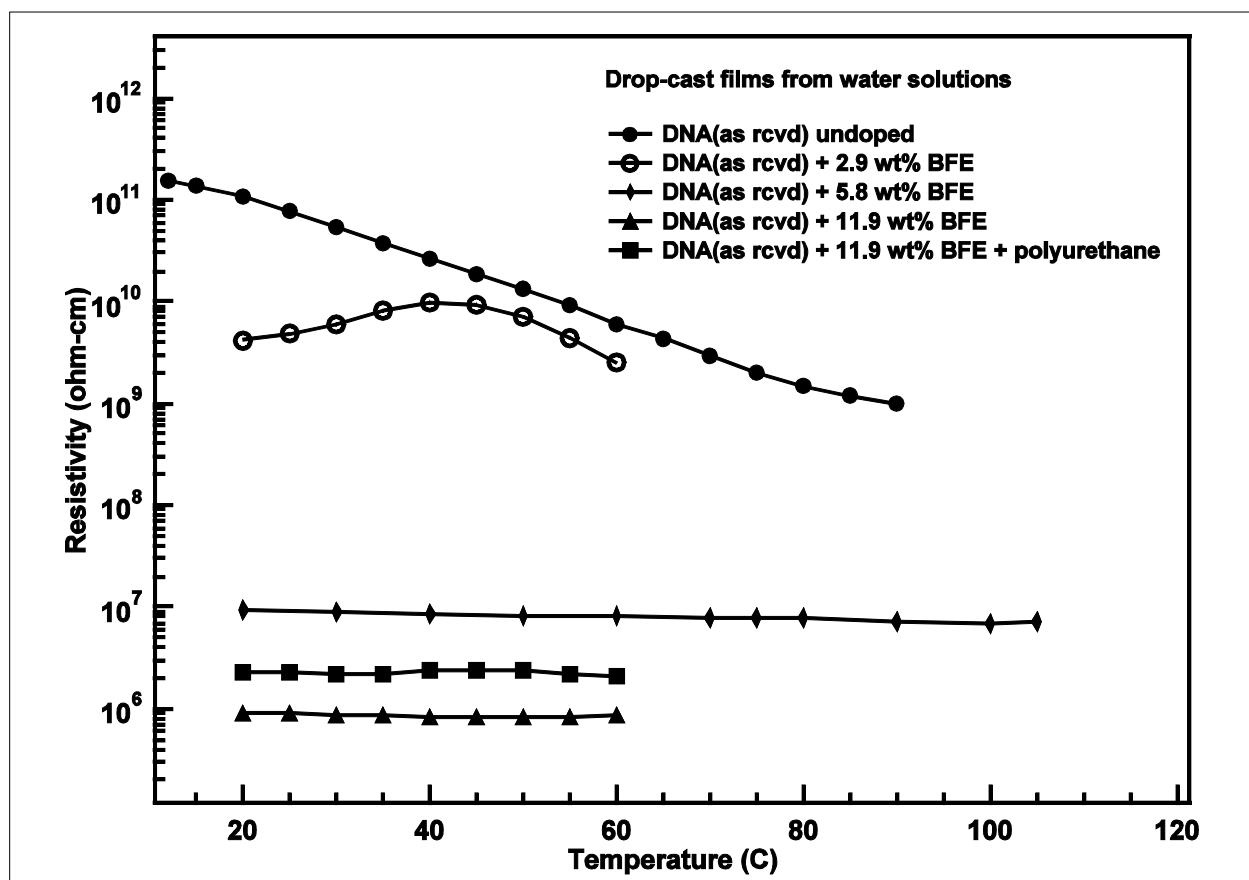


Figure 32. Behavior of as-received DNA with dopant BAYTRON FE (from H. C. Starck-CLEVIOS).

Note the linear temperature scale on the abscissa.

1.5.4.5 Discussion

Our studies show that, with the exception of RX silk and continuously-sonicated DNA-CTMA, the room temperature resistivities of the non-doped bio-derived polymers are a factor of 10 or more lower than the oil-derived polymers measured in this work. Moreover, except for PVP, the

activation energies of the oil-based polymers average 0.84 eV, as compared to the range of 0.96 to 1.44 eV for the as-received DNA-CTMA and the five molecular weights of DNA-CTMA given in Figure 24 and Table 3. A second difference is the high corner temperatures of $T_c \sim 80^\circ\text{C}$ of APC and PVP. The only other studied vacuum-dried polymers that showed high T_c were Tuft's silk and continuously sonicated DNA. One possible connection between these four materials could be that they are all highly amorphous.

Referring to Table 3, this leads to a third difference between Group A that has the five molecular weights of DNA(sonicated)-CTMA and Group B that includes DNA(>8000 kDa), DNA(>8000 kDa)-CTMA, Tuft's silk, APC, PVP, P4VP and PMMA, which is the extraordinary gap between the values for the prefactor σ_0 . The A:B ratio of these values range between $\sim 8.8\text{E}3$ and $9\text{E}15$. Following the DC hopping model by Miller and Abrahams⁽⁶¹⁾ reviewed and updated by Böttger and Bryksin⁽³¹⁾, this prefactor for nearest neighbor hopping is proportional to $\exp[-f(\eta\alpha N^{1/3})]$ in a disordered or random material, where α is the inverse of the Bohr radius (Bohr radius = $5.29\text{E}-2$ nm), N is the number density of the sites involved in hopping transport, $N^{1/3}$ is the mean spacing of pairs of hopping sites and η is a number of order unity. Assuming the proportionality constants are approximately equal for the two groups, then the natural logarithm of the A:B ratio of the prefactors ranges from ~ 9 to 37 Bohr radii (using the minimum and maximum A:B ratios). This indicates the difference between the mean hopping distances of Group B minus Group A ranges between ~ 0.5 to 2 nm. These are significant differences on the atomic scale and demonstrate that Group B polymers are better electrical insulators than Group A and the sonicated DNA materials have higher densities of hopping sites, which presumably could lead to enhanced conductivity, if some kind of ordering can be achieved in the material. Based on this approximate analysis, APC and Tuft's silk have the lowest density of hopping sites relative to Group A.

The DNA studies by Kutnjak et al.⁽⁵⁹⁾ included measurements at 78 V/cm of the conductivity of $3\text{-}4$ mm thick specimens of vacuum dried, oriented $10,000$ kDa Li-DNA prepared from calf thymus, but most of their studies were at 75% humidity. Their vacuum dried data give a resistivity parallel to the orientational (helix) axis at $\sim 20^\circ\text{C}$ of $5\text{E}12$ ohm-cm, which is 50 times the value we obtained at ~ 15 kV/cm for a vacuum dried 1.56 μm thick film of as-received Na-DNA of molecular weight >8000 kDa. Their data, however, shows for an increase in field from ~ 31 V/cm to ~ 78 V/cm, an increase in the conductivity by seven, which suggests that our lower resistivity (higher conductivity) is due partly to our much higher field and to the statistical orientation of Na-DNA in our devices that sets the field largely perpendicular to the helix axes, as discussed below.

An activation energy of 0.98 eV for oriented, vacuum dried Li-DNA from calf thymus was reported by Kutnjak et al. as compared to 0.67 eV for vacuum dried, randomly oriented Na-DNA from salmon roe and milt sacs used in our work (see Section 1.2). The small polaron is usually considered the hopping charge carrier in DNA^(85,33). In this case, the activation energy of a disordered material is the sum of the energy to move the polaron over its site barrier plus the energy need to hop the distance to another site⁽³¹⁾. The mean site barrier energy seen by the polarons, which must hop between molecules, could depend on either the base sequence in the DNA molecules or the counter ion, while the mean hopping distance would depend on the DNA number density (i.e., packing density) in the material. The change in the Raman spectra for B-form DNA with six different guanine-cytosine (GC) to adenine-thymine (AT) ratios reported by

Deng et al. ⁽³⁵⁾ indicates that the salmon DNA has a GC:AT ratio of ~27% ⁽⁸²⁾, whereas calf thymus has a ratio of 42% ⁽³⁵⁾. This difference in the GC:AT ratios could account for the different activation energies; however, the counter ion and mean hopping distance cannot be neglected. More carefully designed experimental studies are needed to resolve this issue.

Measurements by Eley and Spivey ⁽³⁷⁾ on five specimens of vacuum dried thymus DNA gave an average activation energy $E_a = 1.22$ eV, which compares well to Group A DNA-CTMA average value of 1.30 eV, but is almost twice the 0.67 eV value for our Na-DNA. They dried their specimens in high vacuum at 100°C and their lowest temperature was ~80°C. Since their activation energy is also higher than that reported by Kutnjak et al., it would appear that neither base sequence nor counter ion is a factor. The closeness of the DNA-CTMA average activation energy to the Eley and Spivey value would seem to support different number densities, since the DNA molecules with CTMA counter ions would be expected to have a smaller DNA number density with the corresponding larger mean spacing of the hopping site pairs. More study is needed to understand these behaviors.

An important issue in designing electrical or electro-optical specimens using sonicated DNA material is the dependence of bulk (or volume) electrical and electro-optical properties on the molecular weight of the sonicated DNA (see Section 1.2.1). The results for dc resistivity given in Table 3 show this dependence. As discussed in Section 1.5.3, the observed conductivity in the films studied in this work is due primarily to the molecule-to-molecule charge transport, which can be expected to be constrained by the mean length of the molecules, which is proportional to the molecular weight. This means the statistical distribution of orientations of the molecules in the thin films relative to the electrodes depend on the molecular weight. Okahata et al. ⁽⁶²⁾ measured the conductivity of dried, aligned DNA strands in a film and reported the conductivity parallel to the strands to be four orders of magnitude higher than perpendicular to the strands. This behavior can be attributed, at least in part, to anisotropic mobility such as computed for a GC sequence by Ortmann ⁽⁶³⁾, which will be dependent on base sequence in the particular DNA molecule under study ^(85, 33). Thus, it is reasonable to conclude that changes in resistivity of our films are due to the changes in the orientation distribution of the molecules with molecular weight. As described in Section 1.5.3, since high molecular weight DNA would be expected to have a large fraction of the helix axes perpendicular to the applied field, the high molecular weight would have the lowest conductivity (highest resistivity) as reported here. As the molecular weight is decreased, the molecule length decreases and the orientation distribution will include more molecules aligned parallel to the applied field thereby increasing the conductivity (decreasing resistivity). Thus, the conductivity is dependent on the inverse of the mean molecule length and therefore on the inverse of the molecular weight. The conductivities at 20°C of DNA-CTMA plotted in Figure 33 versus the inverse of the mean molecular weight show increasing conductivity consistent with this model. This behavior follows also at higher temperatures. The trend curve shown in the figure is the likely form of the functional dependence, which is given to illustrate the anticipated flattening out of the dependence for molecular weights above 1000 kDa and below 200 kDa.

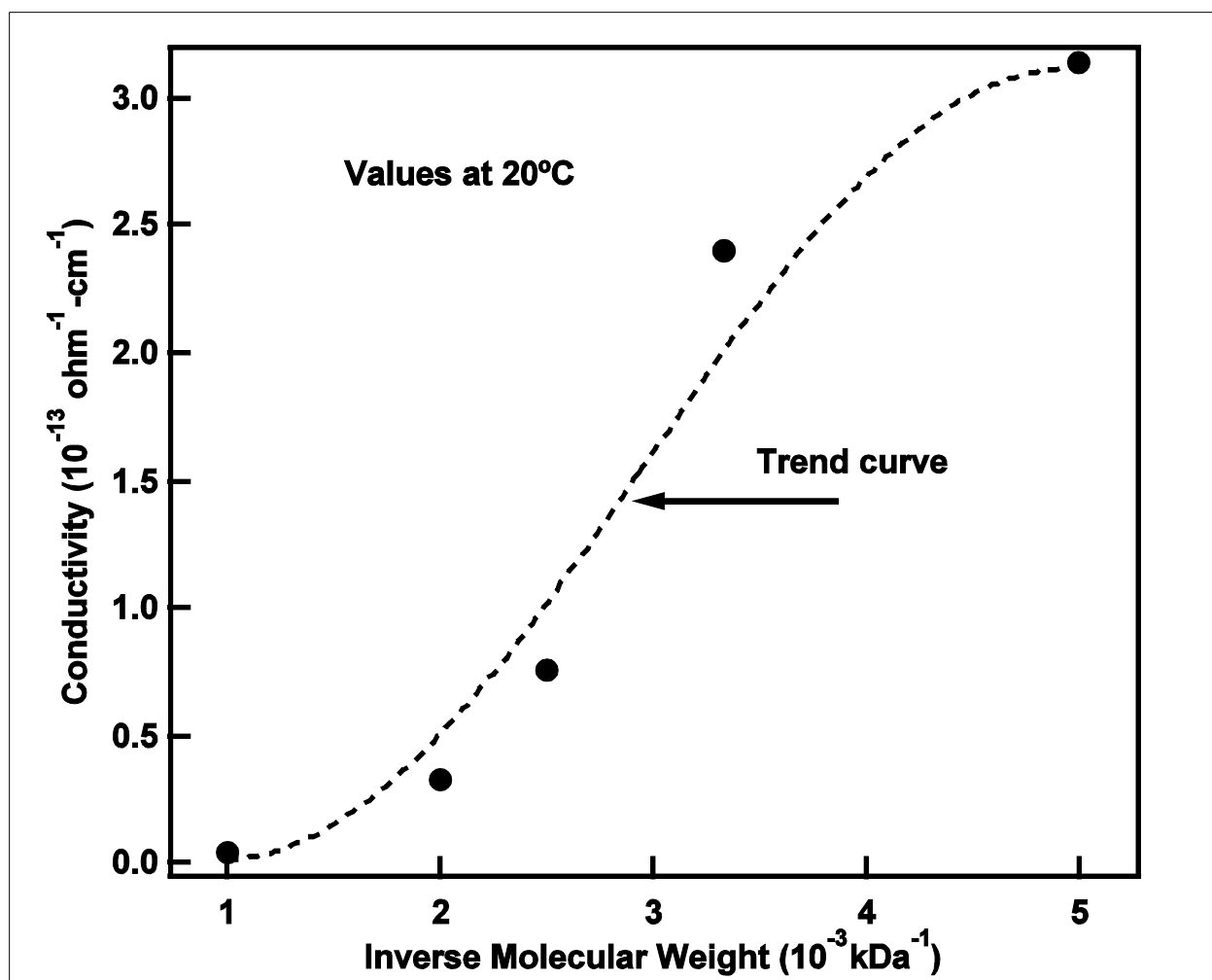


Figure 33. Dependence of the dc conductivities of DNA(sonicated)-CTMA at 20°C on the inverse of the mean molecular weights.

The trend curve is a conjecture showing the expected behavior.

This flattening out at the two ends of the Figure 33 plot happens for similar reasons. As the length of the molecule increases beyond 0.51 μm (1000 kDa), the orientation distribution of the DNA molecules in the films will approach the point where an increase in molecular weight does not change the orientation distribution significantly from parallel to the electrodes, because of the increasing lengths of the molecules. This description appears supported by the >8000 kDa DNA(as-rcvd)-CTMA curve in Figure 24 at the lower temperatures, but shows a change in the flattening behavior with increasing temperature, because of its lower activation energy. At the other extreme, the difference in resistivity between 200 kDa (103 nm length) and 300 kDa (154 nm length) is small indicating that as the molecular weight decreases, the DNA molecules are randomly oriented over all orientations independent of the length and the resistivity approaches a constant value independent of molecular weight. This analysis applies to the typical spin-cast, micron-size films that are fabricated for DNA resistivity measurements. Of course, there are additional factors that might impact the conformation of the molecules in the film, such as interfacial effects. Additional experiments and modeling are needed.

Fabricating films of DNA-CTMA can be done with some degree of confidence that a given film will be smooth and without pinholes. This depends on the solution viscosity, the spin parameters, temperature of the spin solution and the temperature of the substrate as well as the effort taken to minimize bubbles in the wet film during and following spinning. The alternating polarity technique typically shows that the measured current is independent of the polarity, which was the reason for choosing non-chemically-reacting gold electrodes.

1.5.5 Summary

One of the key results of these measurements on DNA, Tuft's silk and oil-derived polymers is that the dc volume resistivity-versus-temperature behavior of these polymers can be described by the Arrhenius function plus a constant from room temperature up to at least 90°C. This implies that the charge transport mechanism in all of these materials above the corner temperature is dominated by nearest neighbor hopping. Many of these measurements were repeated a number of times such that we have high confidence in this description. These studies have also confirmed that this description of the resistivity behavior can be seen only when the film is thoroughly dried and measured in a totally dry atmosphere. Humidity is the primary factor that can cause the measurements to deviate from the above description. There was some concern early on that the dry nitrogen gas we used could be a factor, particularly in the DNA measurements; however, measurements in a dry argon atmosphere were the same as in the dry nitrogen. Among the materials studied, the DNA materials are the most sensitive to humidity.

From the earliest days of resistivity studies on DNA-CTMA, it has been qualitatively known that high molecular weight DNA has a resistivity higher than that of low molecular weight DNA. This is confirmed quantitatively for mean molecular weights between 200 kDa to 1000 kDa. An explanation based on the dependence of the DNA molecule length on the molecular weight and anisotropic mobility relative to the helix axis of the DNA molecules is described.

There is a general increase in the activation energies for the six DNA-CTMA films studied from 0.96 to 1.44 eV, which roughly increases with decreasing molecular weight. This behavior might be due to an increase in the mean spacing of hopping site pairs with decreasing molecular weight, which could point to a decrease in the DNA-CTMA number density possibly due to CTMA. Although, there are significant discrepancies between our activation energy values and those previously reported, our values appear reasonably self-consistent. More measurements and modeling are needed.

Using a simple model for conductivity, large differences in the number density of sites involved in hopping between the DNA(sonicated)-CTMA materials and the oil-derived polymers plus Tufts' silk were revealed in the pre-exponential parameters obtained from fits of Equation 13 to the data. The fact that the as-received DNA did not show these large differences suggests that sonication contributed to these larger hopping site number densities, which is supported by the 200, 300 and 400 kDa sonicated materials having the highest number density values relative to the above materials as determined from the model.

The stark differences in the resistivity behaviors of the two silk films underlines the dependence on the origin and processing history of these complicated biomaterials. Using the DNA results as a reference, it can be suggested that the Tufts' material shows hopping-type conduction, because it

has Arrhenius behavior for $T_c > 60^\circ\text{C}$ with 0.62 eV activation energy, while the RX material shows no Arrhenius-type behavior, and therefore, no evidence of a nearest neighbor hopping transport. The very high resistivity of this material and the temperature behavior suggests that this material is more amorphous than the Tufts' material and might be showing weak ionic conductivity.

The PCBM and Pt dopants or additives that were complexed with the DNA show well-defined activation energies. Both dopants lowered the activation energy, but PCBM lower it by more than a factor of two, which is a desirable feature, because it suggests that PCBM reduces either the hopping site barrier or the mean spacing between the hopping sites in the doped DNA material. The Pt dopant did not provide any significant improvement in the conduction behavior over that of DNA(300kDa)-CTMA. More study is needed to clarify these issues.

The BP and BFE dopants, however, reduced the room temperature resistivity by a factor of 10^4 or more. These are the lowest resistivities with doped DNA we have observed at room temperature. Interestingly, the BP film had a well-defined weak “inverted” Arrhenius-type behavior wherein the resistivity increased with increasing temperature. The increase was only about a factor of two over 20 to 90°C meaning that this polymer has nearly constant resistivity similar to the BFE dopant. This temperature independence or near-independence of the resistivity in the BP and BFE dopants does not fit any of the usual hopping models for the charge transfer mechanism. This suggests that either nearly-free ions or electrons are responsible for charge transport. Although it appears that the DNA functions as a host for controlling the concentration of the highly conductive BP or BFE dopants, more information on how BP and BFE molecules interacts with the DNA molecule is needed before this behavior can be understood. AC impedance studies of these dopant-host systems would be useful towards this end.

2. Biopolymer-Based Bio-Organic Devices

Thin film organic based devices (electrical, optical, and electro-optic) have many advantages over their inorganic counterparts such as low cost, low temperature fabrication leading to flexible, transparent, and biocompatible devices with high tunability. With these new organic structures comes a significant need for new materials to drive the development of high performance devices. One such material is genomic deoxyribonucleic acid (DNA). The structure of the DNA molecule, as well as its high optical transparency and tunable electrical conductivity make it a very useful material for a number of electro-optic devices. Three of these devices are detailed in this chapter: All-DNA-Based Electro-Optic Waveguide Modulator⁽¹¹¹⁾, Field Effect Transistors⁽⁹⁶⁾, and Bio-Organic Light Emitting Diodes⁽¹¹⁰⁾.

2.1 All-DNA-Based Electro-Optic Waveguide Modulator

This research focuses on integrating a DNA-based biopolymer, for the first time, as both the cladding and core layers of an electro-optic (EO) polymer waveguide modulator. The central thesis of the work on this device is that it will seed important advances in the field of photonics research. It introduces a new, bio-derived material with many potential performance enhancements over current polymer materials. As a core EO polymer layer, the DNA was doped with the EO chromophore Disperse Red 1 (DR1) and electrically poled to induce an EO coefficient. To date, this result was the first and only known example of a poled DNA-based polymer film^(112, 113). The first all-DNA-based three-layer optical waveguide was also demonstrated. The waveguide used a DNA-based film for both cladding layers and an un-poled DNA-DR1-based film for the core layer.

2.1.1 Fabrication

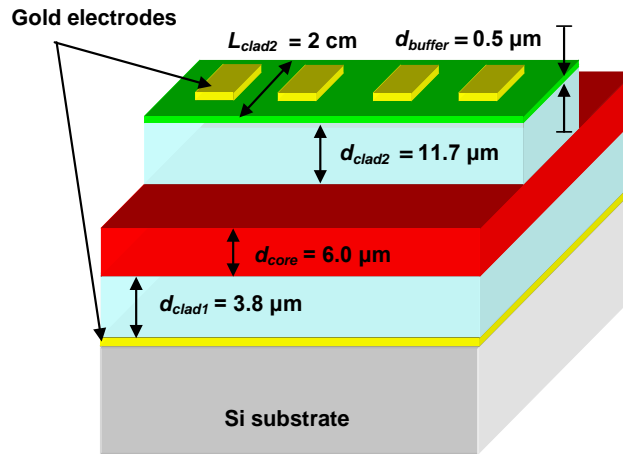
Both the waveguide core and cladding layers were prepared from 200 kilo-Dalton (kDa) DNA-CTMA dissolved in butanol at a concentration of 110 mM. A chemical crosslinker, poly(phenylisocyanate)-co-formaldehyde (PPIF), was used to crosslink the DNA-CTMA films to allow successive spin-coating of multiple layers without solvent damage to the existing layer. The core layer had 20 wt% (81.2 mol%) PPIF crosslinker and 3 wt% (12.8 mol%) DR1 and the cladding layer had 10 wt% (36.1 mol%) PPIF crosslinker. A summary of the refractive indices for films with varying concentrations of PPIF and DR1 are shown in Table 4⁽¹¹³⁾. All percentages are given with respect to the initial amount of DNA-CTMA in each solution. The DR1 was limited to 3 wt% to limit absorption losses at the 690 nm measuring wavelength. Each layer was successively spin-coated onto a gold-coated silicon (Si) substrate at 800 rpm for 10 s with a 5 s ramp. Initial curing to remove the solvent took place for 5 min at 80°C and the samples were then transferred to a 175°C vacuum oven for 15 min. Before spin-coating the top cladding layer, a low-tack tape was used to mask off both ends of the substrate so that only a 2 cm middle section of the core layer was exposed. This facilitates prism-coupling into the core layer to launch the waveguide mode. Finally, a 7.5 wt% polymethylmethacrylate (PMMA) solution in cyclopentanone was spin-coated at 1000 rpm for 10 s with no ramp over the top cladding layer (again using low-tack tape to protect the exposed core layer) and cured at 80°C for 2 h to form an ~0.5 μm buffer or passivation layer. The top electrodes were deposited through sputtering.

Table 4. Refractive indices of various DNA-CTMA (DC) core and cladding materials.

Material	Use	n (690 nm)	n (1152 nm)	n (1300 nm)	n (1523 nm)
DC	Clad	1.5135	1.5054	1.5042	1.5029
DC-PPIF ₁₀	Clad	1.5292	1.5201	1.5191	1.5181
DC-PPIF ₁₅	Clad	1.5325	1.5225	1.5212	1.5199
DC-PPIF ₁₀ -DR1 ₄	Core	1.5526	1.5350	1.5335	1.5321
DC-PPIF ₁₀ -DR1 ₅	Core	1.5476	1.5292	1.5272	1.5252
DC-PPIF ₂₀ -DR1 ₅	Core	1.5637	1.5452	1.5433	1.5415
DC-PPIF ₂₀ -DR1 ₃	Core	1.5544	1.5390	1.5370	1.5350
PMMA	Buffer	1.4881	1.4840	1.4836	1.4832
APC	Buffer	1.5662	1.5548	1.5534	1.5521

Crosslinker is PPIF and DR1 is the chromophore dye. The numbers in subscripts are the amounts of each substance in wt% with respect to DNA-CTMA. The indices listed at 1152 nm and 1523 nm are measured values, while the indices listed at 690 nm and 1300 nm are found from a Cauchy fit to the measured values. Also listed are APC and PMMA, materials that could be used as a buffer layer.

The waveguide has a bottom cladding layer thickness of 6.0 μm , a core layer thickness of 3.8 μm and a top cladding layer thickness of 11.7 μm plus the PMMA buffer layer. This yields a total thickness of 22 μm . All thicknesses were measured with a Veeco Dektak profilometer. This waveguide was not designed to be single mode and supports four TE and four TM modes. Although ultimately single-mode operation is preferred, the multimode design was chosen for ease of fabrication and testing. A schematic of the modulator design is shown in Figure 34⁽¹¹³⁾.

**Figure 34. Schematic of 3-layer DNA-based waveguide modulator.**

Actual Si substrate is round with a 2" diameter.

2.1.2 Electro-Optic Coefficient

Electrode poling was used to pole both the crosslinked and noncrosslinked DNA-CTMA-chromophore films. Preliminary poling studies were made on single-layer films. The films are spin-coated onto indium tin oxide (ITO)-coated glass slides with spinning

parameters optimized to achieve 2 – 3 μm -thick films. After the films have cured, gold electrodes are deposited on top of the film with a 100 Å layer of chromium applied first to promote adhesion. Poling conditions ranged from 60 – 100 V/ μm applied fields at a poling temperature of 60 – 80°C in a flowing nitrogen environment. The EO coefficients were measured using a common ellipsometric technique (modified Teng and Man) ⁽¹³⁹⁾.

A summary of the poling results achieved with single-layer films is presented in Table 5 ⁽¹¹⁴⁾. Because DNA is unique among polymer materials, it presents poling challenges not seen with other polymers. A clear T_g could not be measured for either crosslinked or noncrosslinked DNA-CTMA films using differential scanning calorimetry (DSC). The temperatures used for poling the DNA-based films were determined through systematic study, and 65°C was found to be optimum. The molecular weight (MW) of the starting DNA plays a significant role in the poling efficiency for both crosslinked and noncrosslinked DNA-CTMA films. An EO coefficient could not be obtained for DNA with a MW >1000 kDa; a MW <500 kDa was necessary to induce an EO coefficient. Two different poling techniques were tried and it was found that applying the poling temperature first then incrementally applying the field achieved better results than applying the field first, then raising the temperature. These are referred to as the *T then V* and *V then T* techniques, respectively.

EO coefficients comparable to poled PMMA-DR1 films were achieved with the DNA biopolymer-DR1 films for similar concentrations of DR1. The results in Table 5 are for a single-layer film only. When poling a three-layer waveguide, the resistivities of each layer must be accounted for to determine the actual poling field across the core region ⁽¹⁰⁷⁾. The resistivities of the core and cladding layers were previously measured to be the same; the small differences in crosslinker and DR1 concentrations do not produce a measurable effect ⁽¹⁴⁶⁾. Neglecting the buffer layer, the voltage across each layer can be approximated as the total applied voltage divided by the layer thickness. Because the waveguide is relatively thick (22 μm), the poling voltage across the core region was limited due to the available voltage supply (1 kV). Additionally, the full available voltage range was not used to prevent the possibility of shorting the sample. The sample was heated to a poling temperature of 65°C and a total of 700 V was incrementally applied across the three-layer stack. This corresponds to a poling field of 32 V/ μm across the core region. Based on previous poling data, it is estimated that under these poling conditions for 3 wt% DR1, an EO coefficient r_{33} of 0.5 pm/V was to be expected ⁽¹¹²⁾.

Table 5. Summary of poling results for single-layer DNA-based films.

Sample ID	Mean MW (kDa)	Cross-linker (wt%)	DR1 (wt%)	Poling Field (V/ μm)	Temp ($^{\circ}\text{C}$)	r_{33} (pm/V)	Poling Technique
NXL1	200	0	5	56	65	0.72 ± 0.10	<i>T then V</i>
NXL2	200	0	5	56	65	0.70 ± 0.01	<i>T then V</i>
NXL3	200	0	5	64	65	0.48 ± 0.02	<i>T then V</i>
NXL4	500	0	5	41	65	0.65 ± 0.01	<i>T then V</i>
XL1	200	10	5	70	65	2.02 ± 0.03	<i>T then V</i>
XL2	200	10	5	64	65	1.51 ± 0.02	<i>T then V</i>
XL3	200	20	5	91	65	1.04 ± 0.07	<i>T then V</i>
XL4	200	10	5	75	65	0.83 ± 0.03	<i>V then T</i>
XL5	200	10	5	50	65	0.60 ± 0.02	<i>V then T</i>
XL6	200	10	5	50	100	0.71 ± 0.01	<i>V then T</i>
XL7	200	20	5	75	65	0.74 ± 0.02	<i>V then T</i>
XL8	500	20	5	75	65	1.00 ± 0.04	<i>V then T</i>
XL9	500	20	5	100	80	1.33 ± 0.03	<i>V then T</i>
XL10	500	20	5	100	90	1.12 ± 0.01	<i>V then T</i>

Under Sample ID, “NXL” designates noncrosslinked DNA-CTMA films and “XL” designates crosslinked DNA-CTMA films. All r_{33} results were measured at 690 nm using the ellipsometric technique. Under Poling Technique, T then V designates the temperature was applied before the voltage, and V then T designates the voltage was applied before the temperature.

2.1.3 Device testing and performance

The common crossed-polarizer technique for a transverse EO phase modulator was used to evaluate the performance of the modulator^(114, 147, 143). The modulator is placed between a polarizer-analyzer pair oriented at 45° and -45° so that with no voltage applied, there is no transmitted signal. When a voltage is applied, a phase change between the TE and TM components is induced. Using the isotropic material model (and neglecting overlap issues), the index of refraction change for the TM mode is three times larger than that of the TE mode ($r_{33}=3r_{13}$)⁽¹³²⁾. In this configuration, the resulting equation for the half-wave voltage V_{π} is^(147, 143)

$$V_{\pi} = \frac{\lambda d}{n^3(r_{33} - r_{13})L} = \frac{\lambda d}{n^3\left(\frac{2}{3}r_{33}\right)L} = \frac{\lambda d}{n^3r_{\text{eff}}L} \quad (15)$$

where λ is the wavelength, d is the core thickness, n is the index of the core, L is the length of the electrode, and r_{eff} is the effective EO coefficient for this modulator configuration. For a polymer device, which has different indices in the planes perpendicular and parallel to the poling axis, the addition of a compensator before the analyzer is needed to adjust the polarization of the out-coming light from elliptical back to linear. Because the laser is linearly polarized, a polarization rotator is used in place of the polarizer to orient the incident beam to 45° . A schematic of this configuration is shown in Figure 35⁽¹¹³⁾. Prism coupling was used to couple the beam into

and out of the modulator ⁽¹⁴⁶⁾. A picture of the prism-injected waveguide mode propagating through the modulator both under and next to the top electrode is shown in Figure 36.

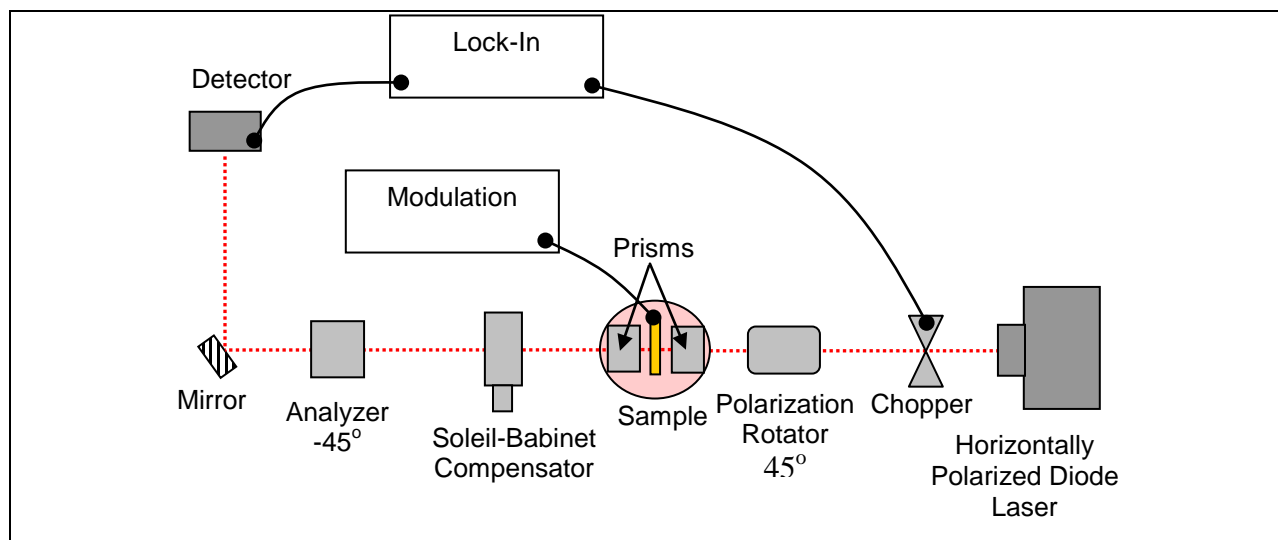


Figure 35. Schematic of testing configuration for transverse EO polymer phase modulator.

The horizontally polarized laser beam is rotated by 45° and an analyzer is set to -45°. The compensator is used to adjust the phase from elliptical back to linearly polarized light. A chopper is used to reference the lock-in amplifier.

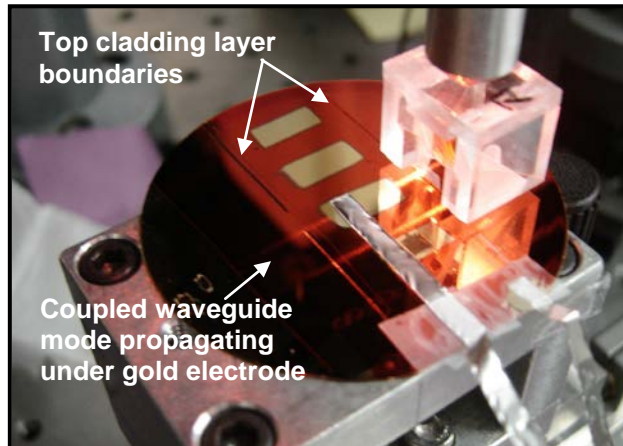


Figure 36. Two beams propagating through three-layer poled DNA-based waveguide.

One beam is propagating under the electrode and the other is next to the electrode. A second beam between the electrodes is also shown.

After launching 45° linearly polarized light into the modulator, it was found that the amplitude of the TE mode was larger by a factor of three than that of the TM mode. This prevents cancellation of the two polarization components at the output, regardless of the compensator setting. To ensure equal TE and TM amplitudes at the output, the polarization rotator was adjusted toward TM until the output TE and TM amplitudes were equal and good cancellation was observed. With no

voltage applied across the sample, the compensator was adjusted to find minimum transmission. A dc voltage was then applied across the electrodes to induce a phase change between the TE and TM components. A lock-in amplifier was used to measure the resulting signal change.

Because of the 22 μm total modulator thickness, it was not possible to apply a dc voltage large enough to observe a π phase change. Based on our estimate of $r_{33} = 0.5 \text{ pm/V}$, and given the modulator parameters of $L = 0.8 \text{ cm}$, $d = 3.8 \text{ }\mu\text{m}$, $n = 1.5544$, and $\lambda = 690 \text{ nm}$, a V_π of 262 V was expected. To observe the π phase change with this half-wave voltage would require a total voltage of 1517 V across the 22 μm three-stack. To avoid risking electric field breakdown of the materials making up the modulator, the voltage was limited to 400 V. A sine-squared function was fit to the data; however, the data spanned an insufficient range to conclusively determine the function fitting parameters. This precludes the possibility of determining the values of V_π and r_{33} , as there are an infinite number of sine-squared fits to these data. However, by using our predicted value of $V_\pi = 262 \text{ V}$ and the square root of the modulation signal as a weighting factor (assumed proportional to the standard deviation in the curve fitting), a good fit was found to the data. This fit yielded a $V_\pi = 263 \text{ V}$ with an uncertainty of $\pm 10\%$ ⁽¹¹³⁾. Figure 37 shows the change in the lock-in signal as a function of applied dc voltage with the sine-squared fit. Although this analysis does not give an experimentally-determined value of V_π and thus r_{33} , it does confirm the expected sine-squared behavior within a reasonable uncertainty.

An unpoled electrode on the same specimen was also tested to confirm that the observed effect was an EO effect and not another voltage-dependent effect such as piezoelectric or electro-absorption. No change in signal was observed as a result of the applied voltage, confirming that the observed effect is EO. The poled electrode on the modulator was tested several times over a 5-day time span. Qualitative ac modulation was also observed. For ac modulation, the chopper was removed and the lock-in was driven by the applied ac signal. A dc bias of 200 V was applied in addition to the ac signal. A clear ac modulation was detected with both the lock-in and a digital oscilloscope. Figure 38 ⁽¹¹³⁾ shows the oscilloscope screen with both the applied ac signal and the observed ac modulation of the laser beam ⁽¹¹³⁾. No ac modulation was observed with the unpoled modulator.

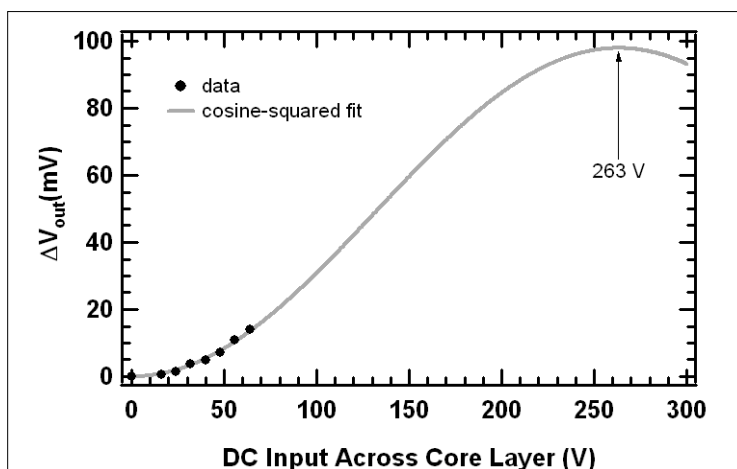


Figure 37. DC modulation of an all-DNA-based EO modulator, extended view.

A sine-squared fit is used to find the DC input across the core layer required for a π phase change.

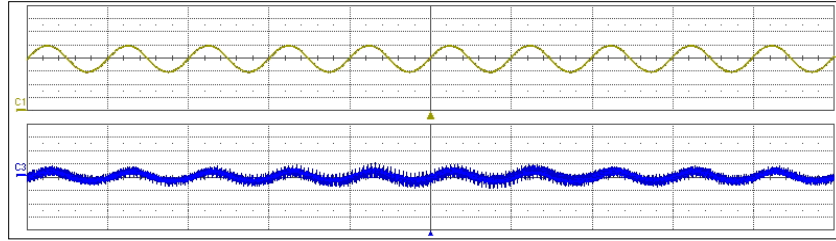


Figure 38. Oscilloscope screen showing ac modulation of all-DNA-based EO modulator.

The top trace is the applied voltage of 200 V dc plus an ac component of 35 V rms. The modulated signal from the photodetector is shown in the bottom trace with a value of 0.6 mV rms. The channel labels at the left (C1 and C3) indicate the zero voltage positions.

2.1.4 Conclusions

An all-DNA-based EO waveguide modulator has been successfully fabricated and tested and found to exhibit EO modulating behavior. Using an estimated value of $r_{33} = 0.5$ pm/V and $V_{\pi} = 262$ V, a sine-squared fit to the modulating data was obtained that yielded a $V_{\pi} = 263$ V with an uncertainty of $\pm 10\%$. While these performance parameters are far below the desired industry standard of sub-volt operation already demonstrated by other polymer modulators⁽¹⁴³⁾, it is predicted that future DNA-based biopolymer Mach-Zehnder modulators can meet or exceed current polymer device performance (and would utilize the full value of r_{33}). This can potentially be accomplished by using an increased concentration of a higher quality chromophore to achieve a greater EO coefficient. Reducing the thickness of the core and cladding layers and using lower resistivity cladding layers, relative to the core, will also allow for higher poling fields to further increase the EO coefficient, in addition to allowing single mode operation. Additionally, an all DNA-based Mach-Zehnder device offers several promising advantages over conventional polymer devices including reduced optical losses, refractive index tunability for enhanced waveguide design and increased EO activity through chromophore alignment. It is projected that this device demonstration will lead the way to attaining these many potential advantages of the DNA biopolymer.

2.2 Field Effect Transistors

2.2.1 Principles of Operation

Thin-film field effect transistors (FETs) are three terminal devices that use a small input signal to control a large output⁽¹³³⁾. The three terminals of the FET are typically called the gate, source and drain. Each FET is designed to have a particular spacing between the source and drain. The gate is separated from the source and drain by a layer of electrically insulating material. The first organic thin-film transistor, reported by Weimer in 1962, is based on polycrystalline semiconductor films deposited onto an insulating substrate (Weimer 1962).

The FET structure used in this work is that of a metal-insulator-semiconductor field effect transistor (MISFET). Current flows from the source to the drain of the MISFET when voltage is applied across the source and drain (V_{DS}). The resulting current (I_{DS}) can be influenced by voltage applied to the gate (V_{GS}). V_{GS} causes a layer of charges that is just a few nanometers thick to form at the interface between the insulator and the semiconductor thin film. The layer of accumulated charges at the interface of the semiconductor and insulator is the channel. This channel connects

the source to the drain, and permits the flow of charges when the transistor is active. The maximum amount of charge that flows through the channel at any particular time is controlled by the voltage applied to the gate. FETs can operate in two different modes, called enhancement mode and depletion mode. A depletion mode, or normally on, FET has a large channel where current is free to flow when there is no gate bias applied ($V_{GS} = 0V$). Therefore, to stop the flow of current through a depletion mode FET, a negative or positive bias (depending if the semiconductor is n or p type) is used to deplete the channel of charge carriers⁽¹³¹⁾. The pinch-off voltage in a depletion mode FET is the voltage that causes the channel to be completely shut-off, and current no longer flows. An enhancement mode, or normally off, FET has no current flowing when there is no gate bias (no accumulation layer); therefore, for current to flow, a channel first needs to be created⁽¹³¹⁾. The threshold voltage in an enhancement mode FET is the voltage where the transistor changes from having no current flowing in the channel to having current flow. In an enhancement mode FET, applying a bias with a greater magnitude than the threshold voltage ($V_{GS} > V_t$) to the gate causes the channel to expand such that more current flows. The ratio between I_{DS} in the off state (no accumulation layer is present) and I_{DS} in the on state is called the on/off ratio, and this provides a measure of the performance of the FET as an electronic switch. The drain current equation for a FET in the linear region is given by Equation 16.

$$I_{DS} = \mu_{lin} C_i \frac{W}{L} \left[(V_{GS} - V_t) V_{DS} - \frac{1}{2} V_{DS}^2 \right] \quad (16)$$

and in the saturation region (at higher V_{DS}), the drain current equation is given by Equation 17.

$$I_{DS} = \mu_{sat} C_i \frac{W}{2L} [(V_{GS} - V_t)^2] \quad (17)$$

where I_{DS} is the drain current, W/L is the ratio of channel width to channel length, μ_{sat} is the charge carrier mobility in the saturation region, μ_{lin} is the charge carrier mobility in the linear region, V_{GS} is the gate to source voltage, V_{DS} is the drain to source voltage, C_i is the capacitance per unit area of the electrical insulator, and V_t is the threshold voltage. The transconductance, g_m , in the linear region, is given by Equation 18.

$$g_m = \frac{\partial I_D}{\partial V_G} = \frac{W}{L} C_i \mu_{lin} V_D \quad (18)$$

where the partial derivative of I_{DS} with respect to V_{GS} is taken for a constant value of V_{DS} , and the variables are as defined above.

2.2.2 Polymer FETs

The FETs of interest in this chapter are those that have one or more polymer layers. Polymers can be used for any part of a FET. When a polymer makes up any layer of a FET, from the electrodes to the semiconducting layer, the FET is often referred to as a polymer FET, an organic FET (OFET), or a thin film transistor (TFT). The advantages of organic-based FETs include low cost,

abundance of raw materials, and most importantly the possibility of designing large area systems by using simple techniques such as spin coating and vacuum evaporation. The development of OFETs is presently hindered by poor device performance, as compared to their inorganic counterparts such as crystalline or amorphous Si transistors. This is mainly due to the very low charge carrier mobilities in organic semiconductors. Most of the organic FETs described are constructed as thin-film transistors with silicon dioxide, SiO₂, as the insulator.

The first solid-state OFET using an organic semiconductor on an inorganic dielectric is reported in a paper published two decades ago⁽¹⁰³⁾. A. Tsumura *et al.* demonstrate a transistor that is fabricated utilizing a film of an organic macromolecule, Polythiophene, as a semiconductor (~1400 Å thick) and thermally grown SiO₂ (~ 3000 Å thick) as a gate insulator. They report an on/off ratio around 10², with a field effect mobility of ~10⁻⁵ cm²/(Vs) and a transconductance of 3 nS⁽¹⁴¹⁾.

Yamamoto *et al.* examine a spin-coated polymer semiconducting layer made of copolymers in which standard transistor behavior is observed. Copolymers are polymers that are capable of operating in both n-type and p-type FETs⁽¹⁴⁵⁾. TFTs using semiconducting polymers show that performance is dependent upon polymer film thickness⁽¹⁰¹⁾. Polymers can be used as gate dielectrics, but this has caused a large hysteresis in the transfer characteristics. Uemura *et al.* report that using a layer of mineral clay to protect the semiconductor layer eliminates the hysteresis⁽¹⁴²⁾.

All-polymer FETs

All-polymer FETs are typically fabricated by spin-coating, vapor deposition and other common lithography techniques with all the layers made of polymer materials. They are shown to be stable in air without protective coatings which is important for low-cost, high volume applications⁽¹²⁸⁾. In comparing all-polymer FETs to fully inorganic FETs by changing one layer at a time of the inorganic FET to a polymer material, it is reported that very slight degradation of performance is seen when the polymer layer replaces the silicon substrate and oxide layer⁽⁹⁵⁾. Organic FETs need to be lightweight, thin and pliable to obtain flexible electronic devices. Pliable materials need to be used for the active and insulating layers in order to achieve this⁽¹⁴⁸⁾. Thin film semiconducting polymers can be used as the active material in FETs. However, undoped semiconducting materials have high electrical resistivities. Edman *et al.* report that doped semiconducting polymers have lower electrical resistivities, and higher doping levels yield lower resistances. Therefore, polymers with high electron and hole mobilities, that can support doping, are useful for transistors⁽¹⁰⁴⁾.

The mobility and device performance of FETs with organic gate insulators are affected by the specific polymer used⁽¹¹⁷⁾. X. Peng *et al.*⁽¹²⁶⁾ reports the first all-organic thin film transistors made of alpha-sexithienyl (α6T) as the semiconducting layer with various polymeric insulating layers. They compare the field effect currents from five different polymers as gate insulators. These five polymers are polystyrene (PS), polymethymethacrylate (PMMA), polyvinyl alcohol (PVA), polyvinyl chloride (PVC), and cyanoethylpulluan (CYEPL). Their results ranged from no field effect current to an amplified current that surpassed the SiO₂-based devices.

Ashizawa *et al.* report on successfully fabricating and testing FETs where the source, drain, and gate electrodes and also the channel are made of the same doped conducting polymer. The FET is normally on, with a positive gate voltage causing it to act in depletion mode⁽⁹⁴⁾. Thin film polymer

FETs have also been used for optical emission applications. The gate bias controls the location of the light emission^(135, 129). In these light emitting FETs, high performance is obtained from the simultaneous injection of holes from the drain and electrons from the source⁽¹²⁹⁾.

Sensor applications

Many polymer FETs described in the literature are used for sensing applications. Sensors are devices that measure a particular signal, such as voltage, temperature, gas, and light. Krishna *et al.* describe a polymer FET with a conducting polymer gate that is fabricated as a chemical sensor using standard complimentary metal-oxide-semiconductor (CMOS) processing⁽¹²²⁾. Kazanskaya *et al.* report on FET based sensors with a polymer membrane that works as a potentiometric sensor detecting ammonium ions or as a biosensor detecting urea. The polymer membrane used with this sensor is light sensitive and its elements are easily changed so that it can detect a variety of biological substances⁽¹¹⁹⁾. Dutta and Narayan report on a polymer FET that detects light and operates as a memory device. Information is optically introduced and electrically removed from this FET⁽¹⁴⁹⁾. Deen and Kazemeini describe the use of photosensitive semiconducting polymers in photodetectors. These photodetectors are highly sensitive with no gate bias⁽¹⁰⁰⁾. The low cost and comparable semiconducting characteristics of polymer semiconducting materials to silicon make their use appealing for sensor applications. However, polymer semiconducting materials tend to have low charge carrier mobility and strong temperature dependence⁽¹⁰⁶⁾, which may not be ideal for some sensor applications.

Conducting polymers are typically the active gate material in gas or vapor sensors. They operate at room temperature, consume lower power than non-polymer based FET sensors and are dependent upon the humidity present⁽⁹⁹⁾. They are more sensitive than resistive gas sensors and they respond quickly⁽¹²³⁾. Using composite conducting polymers prevents humidity from affecting the magnitude of the response but shows significant unwanted temperature dependence. In addition, it is easy to combine the polymer deposition with current CMOS technology⁽⁹⁸⁾.

2.2.3 DNA-biopolymer as the Semiconducting Layer

Field effect transistors are used to demonstrate the use of DNA-biopolymers as the semiconducting layer. Biologically-based field effect transistors (BioFETs) utilizing a DNA-biopolymer as the semiconducting layer are studied. First, a brief description of the measurement system used is given. Next, a bottom gate BioFET structure is described and the results from the first DNA-based semiconducting layer in a transistor are analyzed and discussed⁽⁹⁶⁾. Finally, improvements to this initial device and the results obtained from this improved device are described and analyzed.

Measurement setup

A Keithley 4200 Semiconductor Characterization System is connected to the transistor under study using an on-wafer micromanipulator needle probe station, shown in Figure 39⁽⁹⁶⁾.

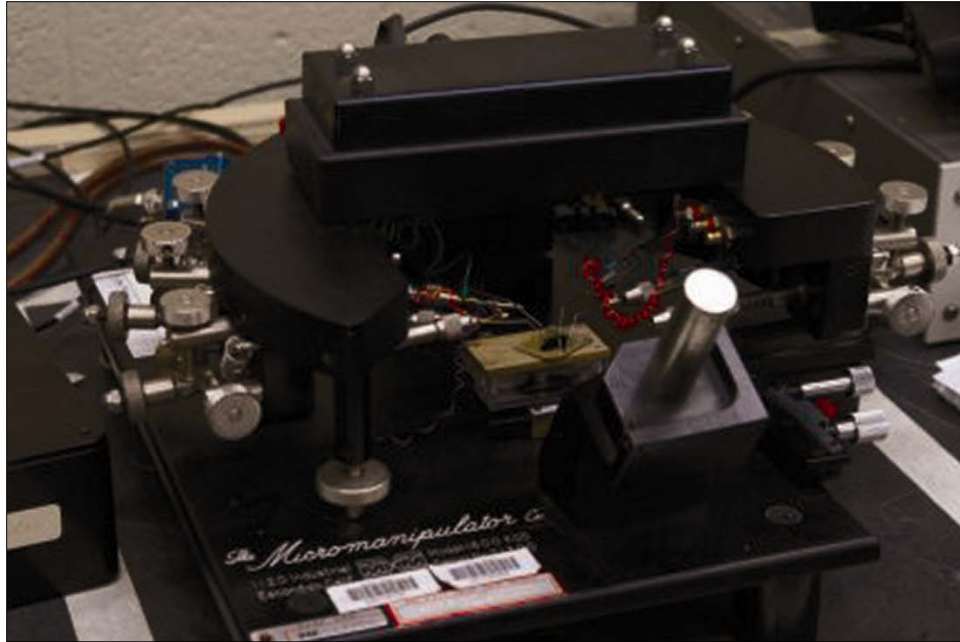


Figure 39. The probe station setup used for measuring the DNA-based transistors.

The semiconductor characterization system controls and measures the currents and voltages in all the transistor structures described in this chapter. This semiconductor characterization system has a current compliance level that can be set for each terminal. The current compliance level is a limit set on the measured current level that limits the power that can be delivered to the device. Using this characterization system, contact is made to the source, drain, and gate by direct contact with needle probes, unless the gate is located on the bottom of the substrate. The sample holder on the needle probe station is gold coated and is, therefore, conductive, so when the gate is on the bottom of the substrate, the needle probe to the gate is placed directly on the sample holder rather than contacting the gate directly. The body on the top gate transistor structure can be contacted in the same way as the gate on the bottom gate structure. The semiconductor characterization system is setup to function as a curve tracer, measuring, recording, and plotting current-voltage (I-V) curves for the BioFETs while also producing a spreadsheet that contains all the voltages and currents being controlled and measured during the test scan.

Initial Bottom Gate BioFET

One of the standard polymer transistor gate insulators seen in the literature is SiO_2 used in a bottom gate FET structure. In the literature, this structure is built from low electrical resistivity silicon wafers with a SiO_2 layer on top of the silicon. The gate contact is on the unpolished side of the silicon wafer, with the SiO_2 , serving as the gate insulator. The source and drain are patterned on top of the SiO_2 and on top of the source and drain the semiconducting polymer is deposited⁽¹⁰¹⁾.

The cross-section of the fabricated BioFET structure is shown in Figure 40⁽⁹⁶⁾.

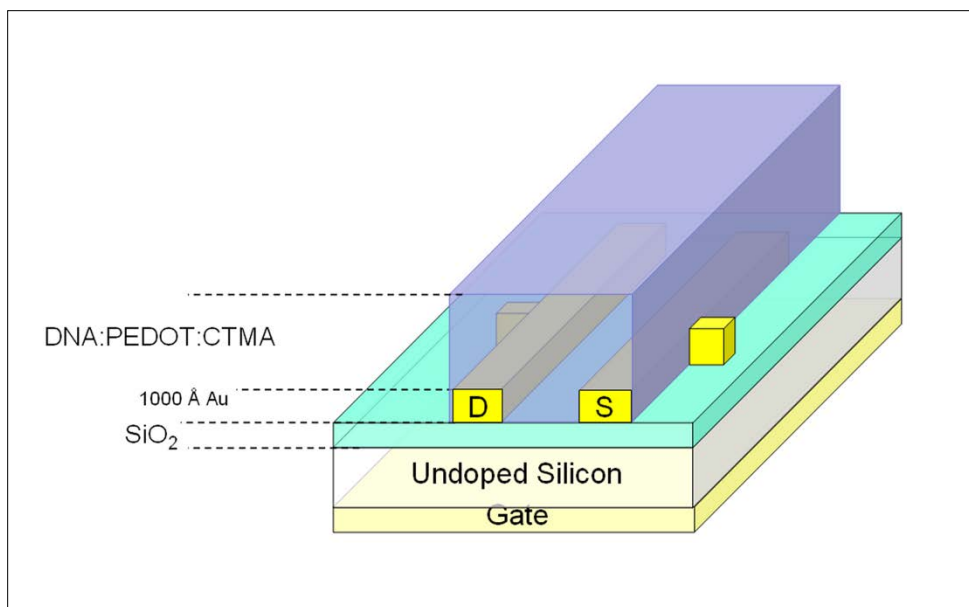


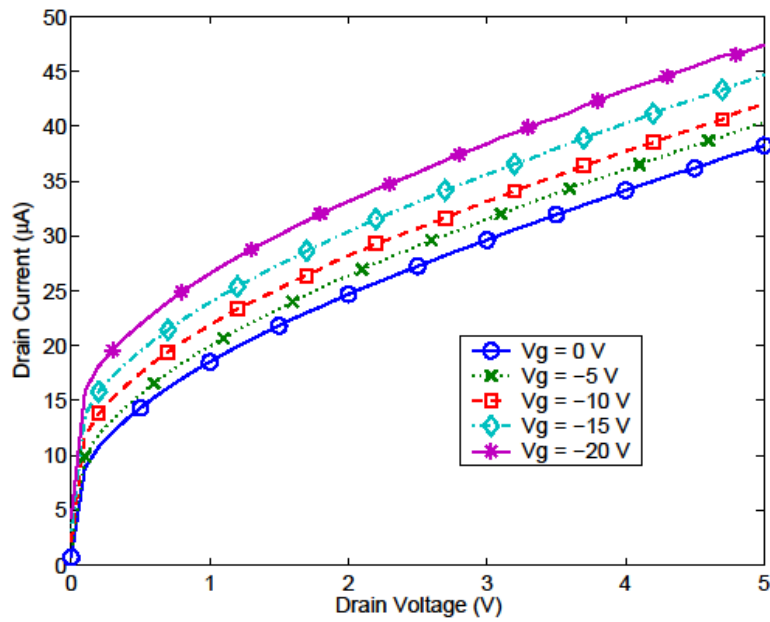
Figure 40. A cross-section of the bottom gate BioFET structure.

A bottom gate BioFET structure similar to that found in the literature, containing DNA: poly(3,4-ethylenedioxythiophene) (PEDOT):CTMA as the semiconducting layer, is fabricated using silicon with a very thin naturally occurring layer of SiO₂ on a silicon wafer instead of a thicker deposited layer of SiO₂ on low electrical resistivity silicon. This structure consists of the gate contact on the unpolished side of a 304.8 μm thick silicon wafer, while the native SiO₂ on the polished side of the silicon wafer acts as the insulating layer. The source and drain are patterned on top of the SiO₂ by sputtering 100 \AA of Cr, for adhesion, followed by 1000 \AA of gold through the same shadow mask, forming a 4.0 mm long and 10.16 mm wide channel. On top of the source and drain, a one micron thick layer of DNA:PEDOT:CTMA is applied by spin-coating to act as the semiconductor.

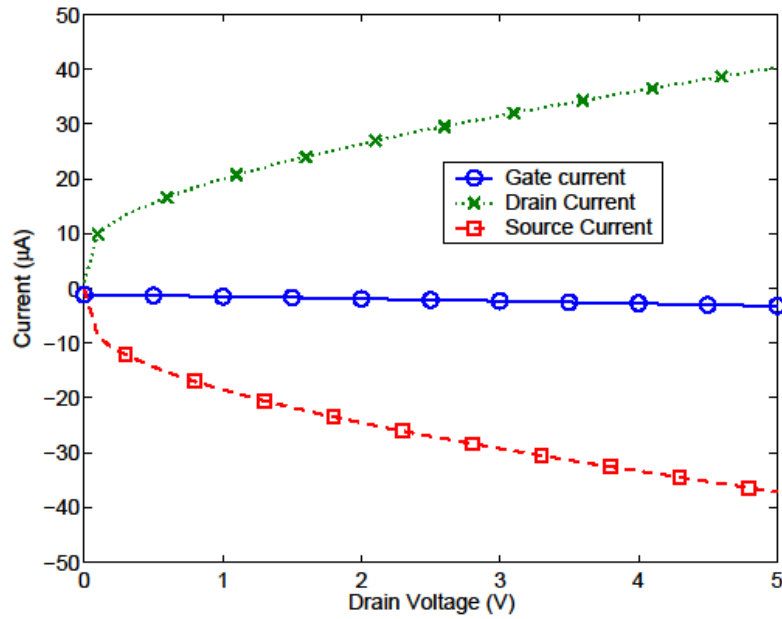
Figure 41 plots the I-V characteristics obtained from a bottom gate BioFET device on a silicon wafer as described above ⁽⁹⁶⁾.

The current compliance limit is set to 0.5 mA on each terminal. This figure shows that for drain voltages from 0.0 to 0.1 V, the drain currents have a steep increase that goes through the origin for all the gate voltages 0.0 to -20.0 V. As the gate voltage increases toward zero, the drain current decreases at positive drain voltages, as one would expect for a depletion mode transistor.

These measurements are of particular interest because the gate currents are substantially lower than the source and drain currents for all drain voltages under all gate bias conditions. The gate, source, and drain currents are plotted as a function of drain voltage with -5.0 V on the gate in Figure 41. This figure shows that the gate current is an order of magnitude smaller than the source or drain current for all drain voltages. It also shows that the source and drain currents are always nearly equal in magnitude and opposite in sign, as expected for a transistor when positive current is defined as current leaving the terminal.



(a)



(b)

Figure 41. (a) Drain current as a function of drain voltage as measured on a bottom gate BioFET on a silicon wafer with a very thin silicon dioxide layer as the gate insulator. (b) Gate, drain and source current is plotted as a function of drain voltage for this device, verifying that the gate current is substantially lower than either the source or drain currents.

Note that positive current is current leaving the terminal.

Both parts of Figure 41 are interesting because together they show that if the gate can be successfully isolated from the source and drain, the gate modulates the drain to source current and transistor behavior is observed.

This data obtained from the bottom gate BioFET described above containing DNA:PEDOT:CTMA shows promise. However, this structure produces higher than expected gate currents. These gate currents are potentially due to the presence of mobile charges in the DNA-biopolymers. Drs. Singh and Sariciftci, collaborators on this research at Johannes Kepler University of Linz, are investigating the use of blocking layers to control these mobile charges in DNA-based devices.

Analyzing the transistor curves presented above, the linear regions show that these BioFETs which are fabricated on a very thin layer of SiO₂ have a calculated electrical resistance that is between 5.4 and 22.9 k Ω . Using a multimeter to measure the sheet resistance of the device yields values that vary dramatically. This is likely due to poor adhesion of the gold source and drain to the very thin layer of SiO₂, and, therefore, one can safely assume that the lower resistance values are more accurate. Making this assumption, the measured resistance of these devices is between 16 and 36 k Ω .

The device mobility for this biopolymer containing FET is determined theoretically from the experimentally obtained current and voltages. Specifically, the drain current equations in the linear and saturation regions, given earlier in this chapter, can be used to determine the linear and saturation mobilities. However, a complicating factor for these calculations is the fact that the mobilities in these regions are not always the same, and often the linear mobility is lower⁽¹²⁴⁾. This means that calculating the mobility in the linear region will only produce a lower boundary for the mobility.

For the data reported here, the threshold voltage cannot be accurately determined. Therefore the drain current equation in the linear region cannot be used to determine the linear region mobility. Instead, using the transconductance, g_m , in the linear region, as defined earlier in this chapter to determine the mobility of the device, the linear mobility is calculated to be 0.018 cm²/(Vs). The mobility of PEDOT:PSS, Baytron P, is known to be 10 cm²/(Vs)⁽¹²⁵⁾. The value obtained for the linear mobility of the FET device is a reasonable value for an insulator doped with a Baytron P conducting polymer as it is reasonable to expect the mobility to be lower than the highest mobility material in the complex. Unfortunately, this value is an overestimate of the mobility of DNA:PEDOT:CTMA, because the width to length (W/L) ratio for the bottom gate device described here is 2.63, and to minimize the effects of fringe currents the W/L ratio should be at least 10.0⁽¹⁰²⁾.

Even without knowing the threshold voltage for the data, the drain current equation in the saturation region, given in Equation 17, can be used to calculate the saturation region mobility. Since there are two unknowns, μ_{sat} and V_t , two equations are needed to solve for the saturation mobility. Therefore, the drain currents corresponding to two different gate voltages at the same drain voltage will be used. Figure 42 shows how the effective saturation mobility, calculated from the drain currents at zero and negative ten volts applied to the gate, varies with drain voltage⁽⁹⁶⁾.

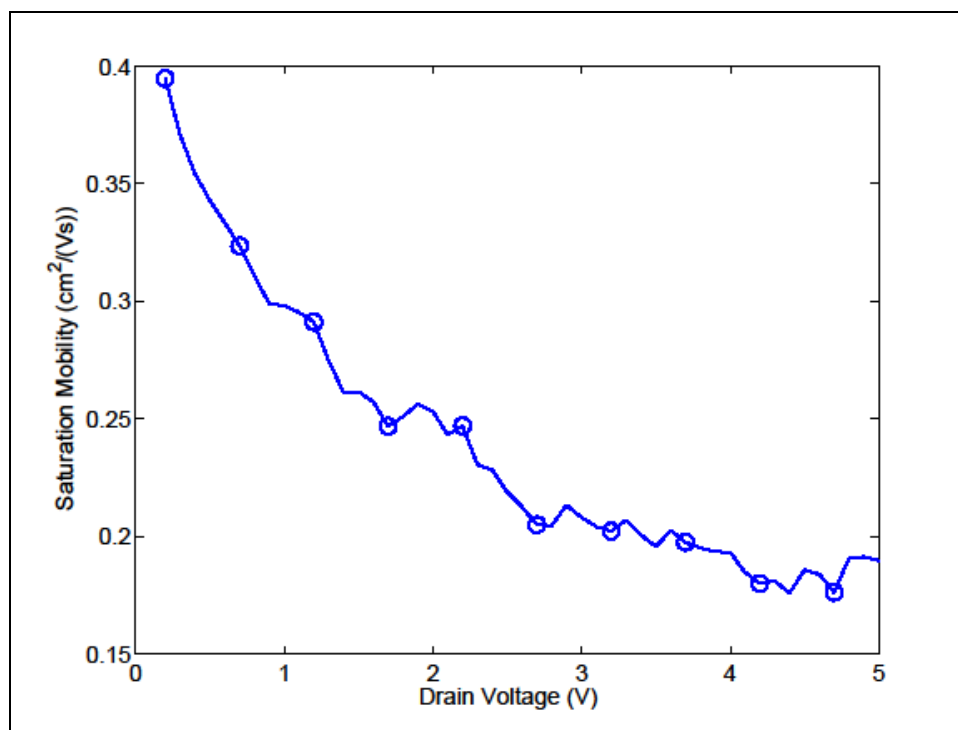


Figure 42. Saturation mobility as a function of drain voltage as calculated from the drain current vs. drain voltage data on a bottom gate BioFET with a very thin layer of native silicon dioxide as the gate insulator.

The data for this plot is calculated using the drain currents associated with gate voltages of 0 and -10 V, when the drain voltage is 0.2 V, obtained from Figure 41.

This figure shows that the saturation mobility decreases with increasing drain voltage in the saturation region of operation for the transistor. Therefore, the maximum saturation mobility occurs at the lowest drain voltage in the saturation region. For the transistor reported above to have low gate currents and produce transistor curves, the effective saturation mobility occurs when the drain voltage is 0.2 V. For gate voltages of 0.0 and -10.0 volts, the maximum saturation mobility is calculated to be $0.45 \text{ cm}^2/(\text{Vs})$.

The mobility values obtained using these methods are overestimates due to the low W/L ratio of the device. Therefore, the true mobility for this material is still unknown. However, the above calculations suggest that the mobility of DNA:PEDOT:CTMA is two orders of magnitude less than the mobility of PEDOT:PSS, the conducting polymer which is combined with DNA to make this semiconductive biopolymer⁽⁹⁶⁾.

Improvements to the BioFET

The same basic structure described earlier continues to be used. Now, a heavily p^+ doped silicon wafer is used as the gate contact, and a 300 nm thick layer of SiO_2 is thermally grown on Si for use as the gate insulator. Cr/Au electrodes that are approximately 100 nm thick are deposited by thermal evaporation on the SiO_2 . These transistors also have a larger W/L ratio, for the source and drain electrodes, of about 5. All of the electrical characterization is carried out under ambient

conditions. Additionally, all I-V measurements are taken with V_{DS} varying from 0 to 20 V, as the thicker gate insulator allows higher voltages to be applied before breakdown occurs.

For devices made using DNA:PEDOT:CTMA, the I-V curves continue to exhibit current amplifier-like behavior as shown in Figure 43.

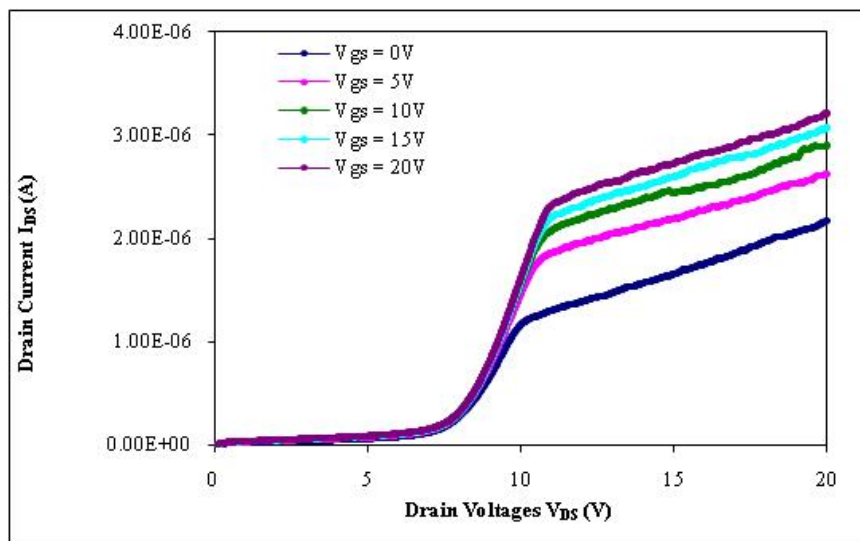


Figure 43. Output characteristics of DNA:PEDOT:CTMA based blends

The measured device parameter (V_{DS} , V_{GS} , and I_{DS}) values for DNA:PEDOT:CTMA containing transistors are comparable to the values obtained for state of the art Pentacene- and Poly (3-Hexylthiophene)- (P3HT-) based field effect organic transistors ⁽¹⁰²⁾.

Field-effect mobility and threshold voltages are calculated using the saturation region current equation for standard MOSFETs, using the steepest slope of the $I_{DS}^{1/2}$ vs. V_{GS} plot with V_{DS} equal to 20 V. The I_{DS} - V_{DS} characteristics are determined for applied V_{DS} ranging from 0 to 20 V with gate biases varying from -10 to 10 V. These results show a slight deviation in the I_{DS} - V_{DS} relationship from the ideal case. The DNA:PEDOT:CTMA containing OFET exhibits high I_{DS} when no gate voltage is applied. Xu and Berger attribute this behavior to the presence of charged impurities in the semiconducting material ⁽¹⁴⁴⁾. DNA:PEDOT:CTMA has a significantly higher overall conductivity than DNA-CTMA due to the blending of DNA with the conductive polymer, PEDOT:PSS.

The increase in drain current, I_{DS} , with an increase in positive gate voltages, V_{GS} , shows enhancement mode behavior with p-type conductivity in DNA:PEDOT:CTMA. A significant offset voltage is measured in the output characteristics of these devices. Though well-behaved saturation characteristics are measured at the output of P3HT based FETs, these devices also produce a slightly lower but significant offset voltage as shown in Figure 44.

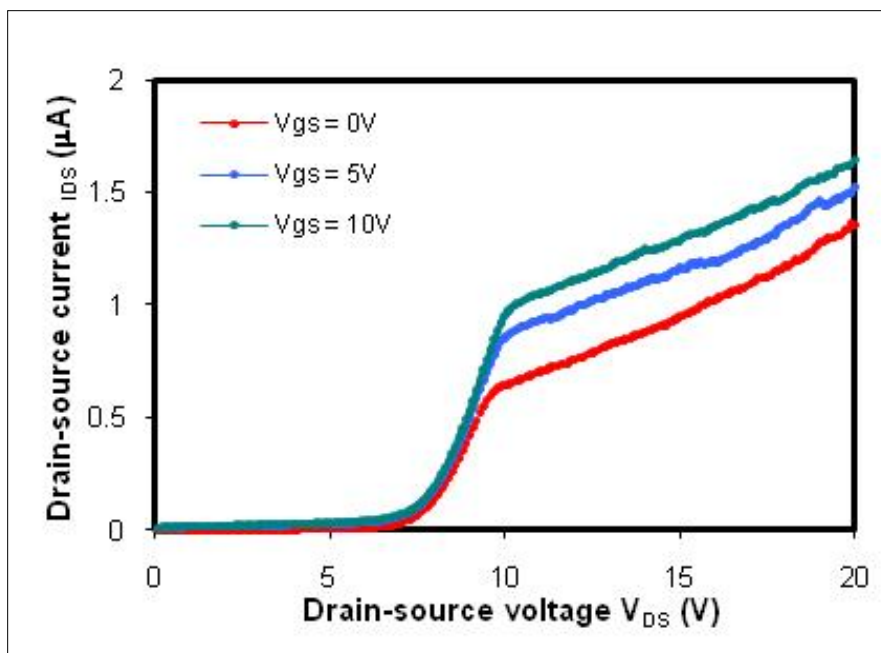


Figure 44. Output characteristics of FETs using P3HT as a semiconducting film

S. P Tiwari *et al.* report an offset voltage on Pentacene based thin film FETs and attributes such behavior to high contact resistance due primarily to the polymer/electrode interface effects and channel dimensions W/L ⁽¹⁴⁰⁾. The BioFET designs described here have $W/L < 10$ which makes the contribution of the contact resistance considerable compared to the channel resistance. This low W/L ratio is most likely responsible for the offset in the drain voltages.

Additionally, the effective free charge carrier mobility is around $8 \times 10^{-4} \text{ cm}^2/(\text{Vs})$ as extracted from the transfer characteristics when V_{DS} is fixed to 20 V. There are several reasons why the approximated mobility for these improved devices is lower than the approximated mobility for the initial device which contained DNA:PEDOT:CTMA as the semiconducting layer. These include the different V_{DS} values at which the mobilities were calculated (recall that it was shown earlier that mobility decreases with increasing drain voltage), a factor of two difference in the W/L ratio for the transistors, and the higher voltage range over which the device data was measured for the improved devices. Each of these factors reduces the transistor mobility and, therefore, the combination of them will further reduce the mobility.

2.3 Development of a BioLED: DNA as an Electron Blocking Layer in Organic Light Emitting Diodes

The field of organic light emitting diodes (OLED) has been growing significantly in recent years due to its applications in high efficiency solid state lighting and high quality flat panel displays ⁽¹³⁰⁾. However, in order for OLEDs to achieve performance levels to rival and exceed their inorganic counterparts, new materials must be developed. There are a number of different material needs in developing OLEDs, such as charge blocking layers (electron and hole), charge transport layers, and emitters. The charge transport and blocking layers must have very specific electrical properties as well as high optical transparency, for efficient photon transfer through the device. As described in this section, genomic DNA derived from salmon has the ideal properties to be present

in an OLED as an electron-blocking layer (EBL). Using DNA as the electron blocking layer (EBL) significantly increases the efficiency of these devices and shows great promise for the future of OLEDs.

2.3.1 Materials Used for the Fabrication of BioLEDs

The following sections review all common materials used in the research of fluorescent type BioLEDs. For all devices, indium tin oxide (ITO) was used for the anode with a work function of 4.7eV, and aluminum (Al) along with a thin layer of lithium fluoride (LiF) was used as the cathode with a work function of 3.1eV.

Emitting Molecules used in Fluorescent Type BioLEDs

The goal of this research was to analyze the performance of DNA-CTMA as a non-emitting material in fluorescent based OLEDs, so a common, well known emitter was chosen. The molecule used for this research was the emitter described in the initial work of Tang and VanSlyke^(137, 138), tris-(8-hydroxyquinoline) aluminum (Alq₃). This material has been widely researched^(108, 91) and emits strongly in the green region. To determine the effectiveness of DNA-CTMA as a non-emitting material in OLEDs, multiple emitting materials were used in separate device structures.

Hole Transport Layers used in Fluorescent Type BioLEDs

The hole transport layer (HTL) used for all devices was poly(3,4-ethylene dioxy-2,4-thiophene)-polystyrene sulfonate, commonly known as PEDOT-PSS, along with the trade name Baytron P from Bayer Corporation. PEDOT-PSS has also been used as a transparent anode on flexible substrates⁽¹⁰⁶⁾. PEDOT-PSS has a highest occupied molecular orbital (HOMO) of 5.2 eV and a lowest unoccupied molecular orbital (LUMO) of 3.5eV. The minimal gap between the 4.7eV work function of ITO and HOMO of 5.2eV makes it a good HTL.

N,N'-diphenyl-N,N'-bis(1-naphthylphenyl)-1,1'-biphenyl-4,4'-diamine (NPB) has a HOMO of 5.25eV and a LUMO of 2.3eV. The close matching of the 5.25eV HOMO of NPB and the 5.2eV HOMO of PEDOT-PSS makes it another excellent HTL. The energy level diagram of a device with PEDOT-PSS and NPB HTLs and Alq₃ as the emitting layer is shown in Figure 45 (Hagen 2006).

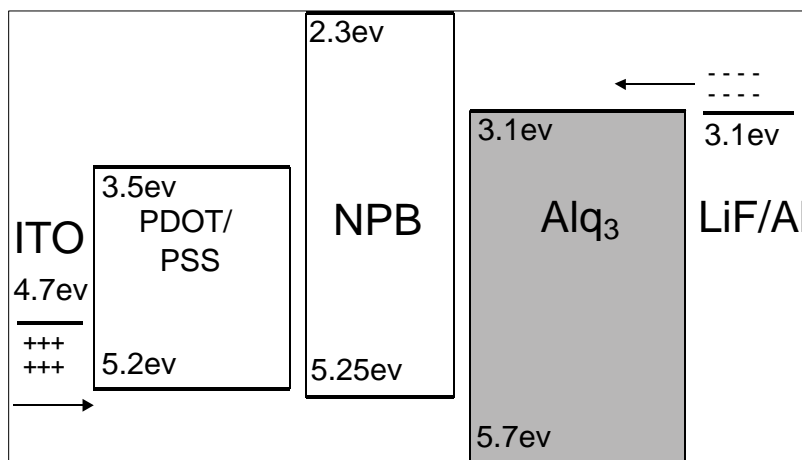


Figure 45. Energy level diagram of fluorescent type OLED with HTLs

Hole Blocking Layer used in Fluorescent Type BioLEDs

Transport layers allow holes and electrons to be efficiently injected into the device. However, the balance of electrons and holes is not always equal. This inequality still allows device emission, but at a much higher current than is necessary. Many of these charges can flow through the device without recombining, which results in a low efficiency. A way of balancing these charges is by using a hole blocking layer (HBL). This layer has a high HOMO value, which acts as a barrier between the emitting layer and the anode. For the BioLED devices, 2,9-Dimethyl-4,7-diphenyl-1,10-phenanthroline (BCP), was used as the HBL. The HOMO value for BCP is 6.7eV, which provides at least a ~1eV barrier for holes to overcome to leak through the device, while it has a LUMO value of 3.2 eV which still allows for efficient electron injection from the electron transport layer (ETL). The advantages of using BCP as a HBL are seen clearly in the energy diagram in Figure 46⁽¹¹⁰⁾.

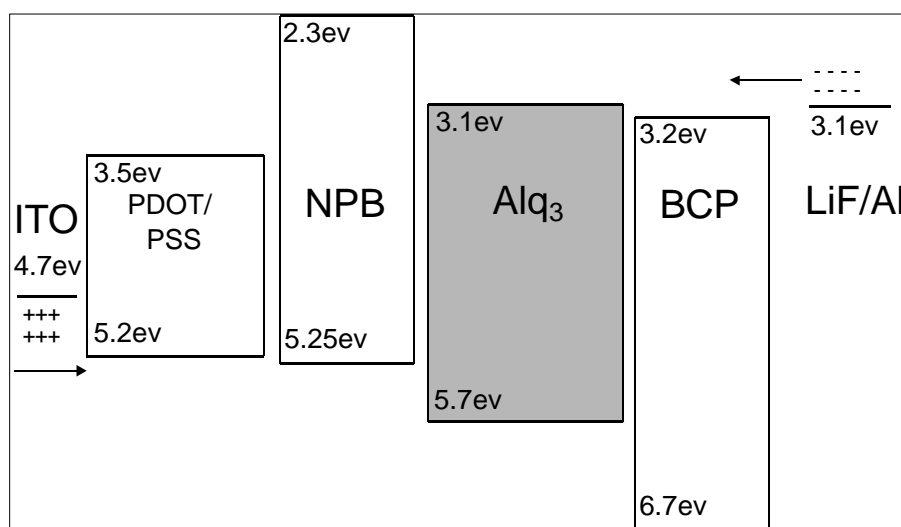


Figure 46. Energy level diagram of fluorescent type OLED with HTLs and HBL

Electron Transport Layer used in Fluorescent Type BioLEDs

Much like the HTL, the electron transport layer (ETL) facilitates the injection of charges into the device, electrons in this case. The LUMO value is key to this material, and must match the work function of the cathode closely. In this case, the emitting material, Alq₃, also happens to have the preferred energy levels of an ETL with a HOMO of 5.7eV and a LUMO of 3.1eV. The resulting energy level diagram for an OLED with HTLs, Alq₃ as the emitting layer, a HBL, and an ETL is shown in Figure 47⁽¹¹⁰⁾ in a typical fluorescent OLED structure.

Electron Blocking Layer used in Fluorescent Type BioLEDs

The heart of this research was the incorporation of DNA-CTMA into common fluorescent type OLED structures as a non-emitting layer. Many devices were fabricated with DNA-CTMA as a host molecule doped with emitting small molecule dyes, but were unsuccessful. DNA-based BioLEDs previously reported^(120, 121) have incorporated DNA-based thin films as hosts for lumophores indicating the feasibility of the concept, but without significant improvement in device performance over conventional OLEDs. Hirata⁽¹¹⁵⁾ have investigated the properties of DNA as a charge transport layer in several device configurations elucidating their properties through their effect on the device current-voltage (I-V) characteristics. None of the previous work

in BioLEDs showed any improvement in device performance by including DNA, nor did any device show performance close to well published OLEDs. By analyzing the unsuccessful BioLEDs fabricated at UC-Nanoelectronics Laboratory using DNA-CTMA as the host layer for the emitter, and closely investigating the paper by Hirata (2004), it became clear that DNA-CTMA may have the properties necessary for an electron blocking layer (EBL). Adamovich et al. first noted the use of EBL layers in OLEDs to prevent electron-hole recombination from occurring in adjacent hole transport layers (HTL) (Adamovich 2002, 2003). DNA-CTMA has excellent optical and electrical properties and has a HOMO of 5.6eV and a LUMO of 0.9eV. The HOMO level matches closely to the HOMO of PEDOT-PSS with only a 0.4eV gap between the two, and the significantly low LUMO provides a large energy barrier to block the flow of electrons, and increase the hole-electron recombination in the emitting layer. The overall structure of the highly efficient green (Alq_3) emitting fluorescent BioLED is shown in Figure 48⁽¹⁰⁹⁾.

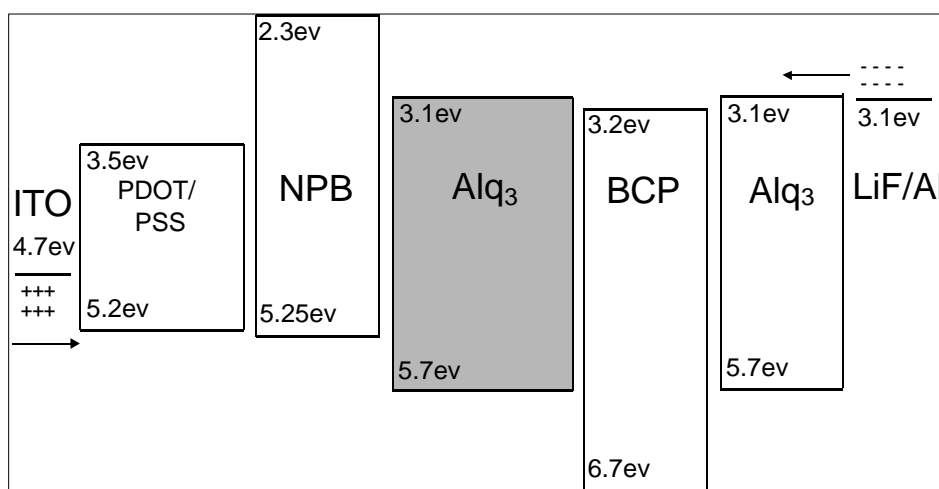


Figure 47. Energy level diagram of OLED with HTLs, HBL and ETL

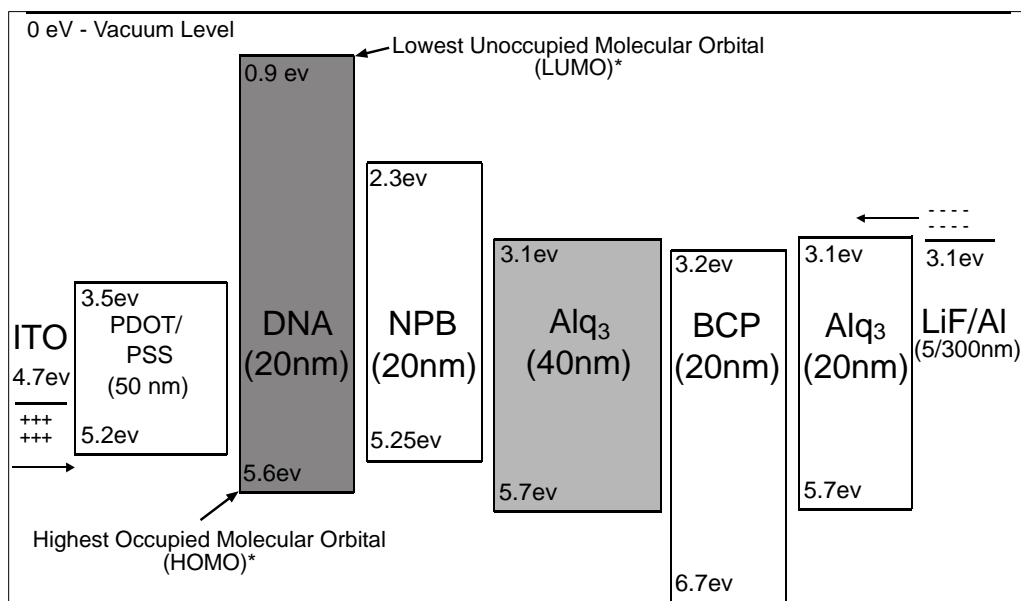


Figure 48. Energy level diagram of Alq_3 emitting BioLED

2.3.2 Fabrication of BioLEDs

Anode Patterning and Deposition

Fabrication of BioLEDs was done using a number of techniques in a clean room laboratory, sputtering, spin coating, and molecular beam deposition (MBD). The devices were built layer by layer, starting with a 2" round transparent glass substrate. These were bottom emitting devices, so they were fabricated starting with the transparent anode, ITO. The substrate was patterned using dry lithography into a unique geometry that resulted in an emitting area of 2mm x 2mm and had large areas for contacting with electrodes. This patterned substrate was then placed into a sputtering chamber where ITO was deposited at 100W power in an Argon plasma at 2 mTorr for 6 minutes. This resulted in a ~40nm transparent film of ITO, which was then thermally annealed at 450°C for 2 minutes to increase transparency and reduce electrical resistivity.

Solvent Based Deposition of Hole Transport and Electron Blocking Layers

The anode patterned device was then cleaned thoroughly in a mixture of solvents (methanol and acetone), followed by rinsing in deionized water and drying with nitrogen. The first layer deposited was the PEDOT-PSS HTL in all device structures. PEDOT-PSS was purchased from Bayer Corporation as Baytron P, which is an OLED grade material, and was diluted with 5 parts isopropyl alcohol to 1 part PEDOT-PSS to aid in film quality. This mixture was filtered using a 0.2 micron PTFE syringe filter and was then ready for spin coating. Spin coating was done using a Laurell spin coater, and the PEDOT-PSS HTL was deposited by dropping the solution onto the substrate and spinning at 2000RPM for 20 seconds. This uniform thin film was then baked in an atmospheric oven at ~130°C, which evaporated all solvents from the film, and further protects the film from solvent attack generated by additional spin coated layers. For all BioLED devices, the next layer deposited was DNA-CTMA as the EBL. For all comparison 'Baseline' devices, this step was omitted, and the remainder of device fabrication remained identical. Low molecular weight (~145K g/mol) DNA-CTMA was dissolved in butanol at a concentration of 1% (by weight of DNA-CTMA). After the solid material was fully dissolved, this solution was filtered with a 0.2 micron PTFE syringe filter, and the solution was ready for spin coating. The desired film thickness of ~20nm required spin coating at 6000 RPM, and this was done for 10 seconds. At this point, the anode, HTL, and EBL (in the case of the BioLED) have been deposited, and the fabrication shifts to MBD.

Molecular Beam Deposition

The remaining layers of the BioLED and Baseline devices were deposited using a SVT Associates MBE system operated at the UC-Nanoelectronics Laboratory. The advantages to using this system include high vacuum deposition at 10^{-8} Torr and well controlled growth conditions using Eurotherm temperature controllers and high quality effusion cells. Another advantage is the large growth chamber which allows for up to three 2" substrates to be deposited simultaneously. This allowed for deposition of the BioLED and Baseline device simultaneously for the most accurate analysis of the benefits of using the DNA-CTMA EBL. Each small molecule material was separately heated up to a set temperature which was calibrated for a set deposition rate. This provided careful control of film thicknesses from run to run. Each of the devices described in the following sections has a slightly different structure based on the desired color output, or emitting layer. All of the film thicknesses reported have been based on the calibrated temperature / deposition rate tables which are constantly updated with the MBE system.

For the green (Alq_3) emitting devices, a 20nm layer of NPB was deposited at a temperature of 265°C as an HTL, and a 40nm layer of Alq_3 was deposited at 230°C as the emitting layer. For the blue (NPB) emitting devices, a 40nm layer of NPB was deposited first, and the 40nm Alq_3 layer in the green emitting device was omitted. Likewise, for the blue-red (NPB-Eu) emitting devices, a 40nm layer of NPB-Eu was obtained by a co-deposition of NPB and Europium (deposited at 240°C), and again the 40nm Alq_3 layer in the green emitting device was omitted.

All of the remaining steps in the device fabrication were identical after deposition of the emitting layer. The next layer deposited was the HBL material BCP at 450°C with a thickness of 20nm. All of the layers up to this point were deposited with a circular mask which leaves the edge of the device free from material deposition for connecting electrodes directly to the anode and cathode of the device. After the HBL was deposited, the substrates were removed from the MBE system, and a second mask was placed over the substrates. This mask has four 'L' shaped patterns which allow the cathode to be deposited resulting in the 2mm x 2mm emitting area. The two final device layers deposited were for the cathode. A very thin layer (~6nm) of LiF was deposited at 730°C, followed by a ~100nm deposition of the Al cathode at 1200°C. The device was complete at this point, as shown in Figure 49 ⁽¹⁰⁹⁾.

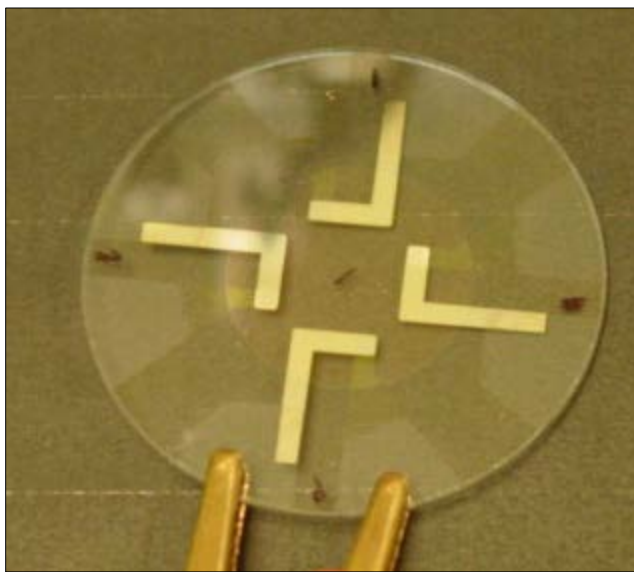


Figure 49. Photograph of finished device

2.3.3 Green (Alq_3) Emitting BioLED Results

The green emitting fluorescent type BioLED structure described in Figure 48 was the first highly successful device. The impact of DNA-CTMA as the EBL was analyzed by fabricating a BioLED device and a Baseline device simultaneously in the MBE system. Each device was tested by applying dc voltage while collecting electrical current and brightness. The voltage and current were controlled by LabView, while the brightness was measured through a Minolta colorimeter. Figure 50 and Figure 51 ⁽¹⁰⁹⁾ show luminance and current density versus voltage (LjV diagram) for the Baseline and BioLED devices, respectively.

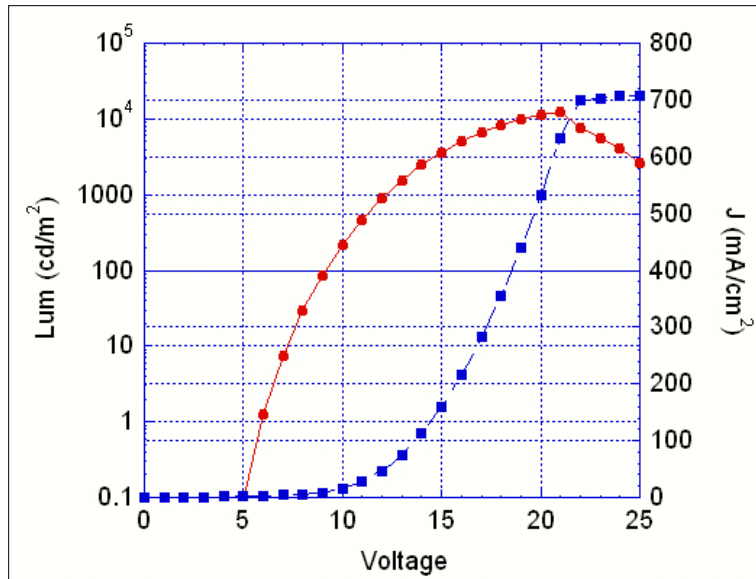


Figure 50. Luminance Current Voltage characteristics for green emitting Baseline device

Both devices were cycled from 0V to 25V, with a maximum luminance of 21,100 cd/m² for the BioLED, and a maximum luminance of 12,400 cd/m² for the baseline device. The emission spectrum of both devices were identical to the characteristic emission of Alq₃. The brightness enhancement of the device by adding a DNA-CTMA EBL is evident in Figures 52 and 53 ⁽¹⁰⁹⁾.

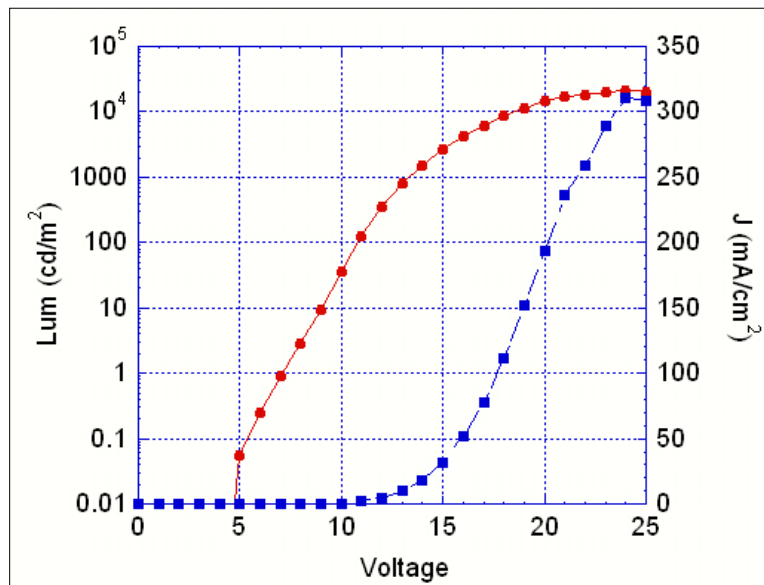


Figure 51. Luminance Current Voltage characteristics for green emitting BioLED device

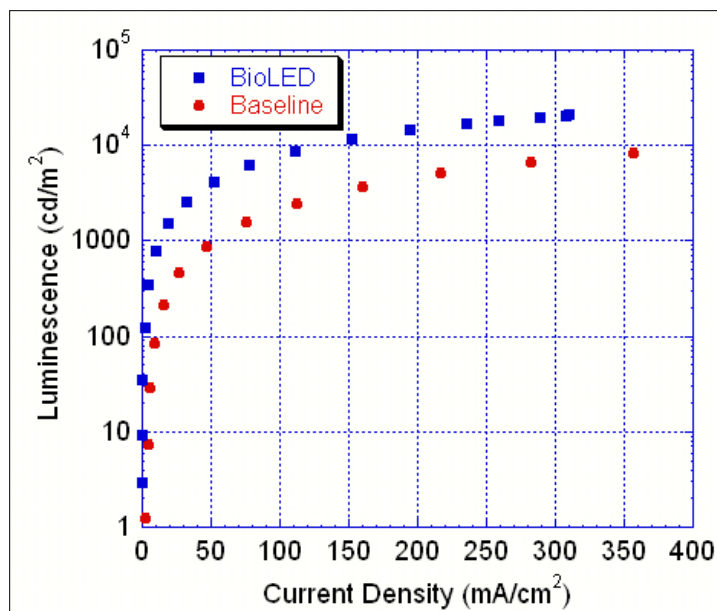


Figure 52. Luminescence versus current density for BioLED and Baseline devices

Figures 49 and 50 also show that the BioLED device achieved the enhanced brightness at a much lower current. Efficiency, as defined previously, describes the number of photons emitted per electrons injected, so it is evident that using DNA-CTMA as the EBL also significantly enhanced the device efficiency. The comparison of efficiency versus applied voltage for both the BioLED and Baseline devices is plotted in Figure 54⁽¹⁰⁹⁾.

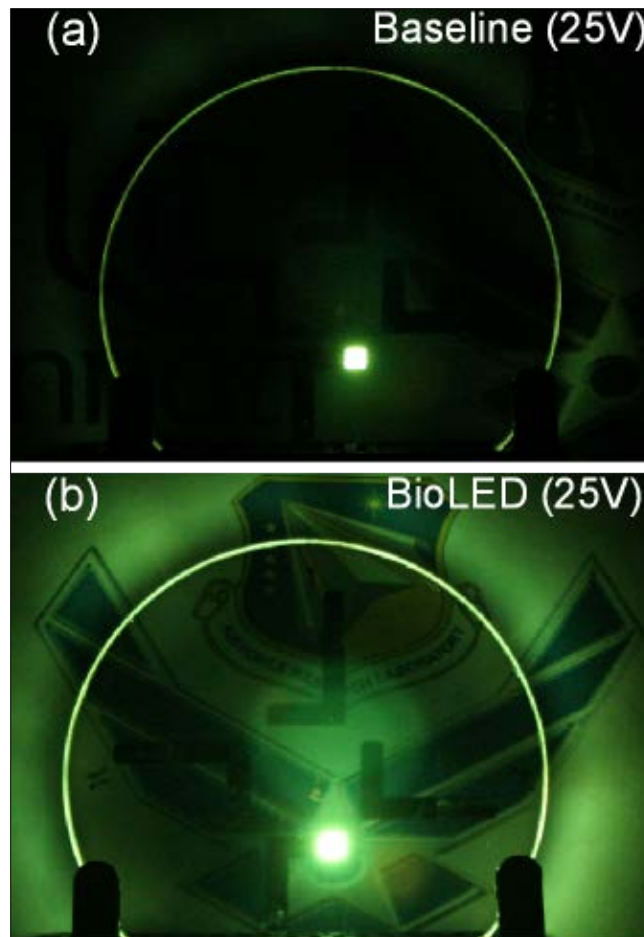


Figure 53. Photographs of green emitting fluorescent type BioLED and Baseline devices in operation

The increase in efficiency for the BioLED device was significant, with $\sim 4\times$ improvement. Operating a device at a set brightness with a low current running through also has an impact on power consumption and possible device lifetime, which is addressed later in this chapter.

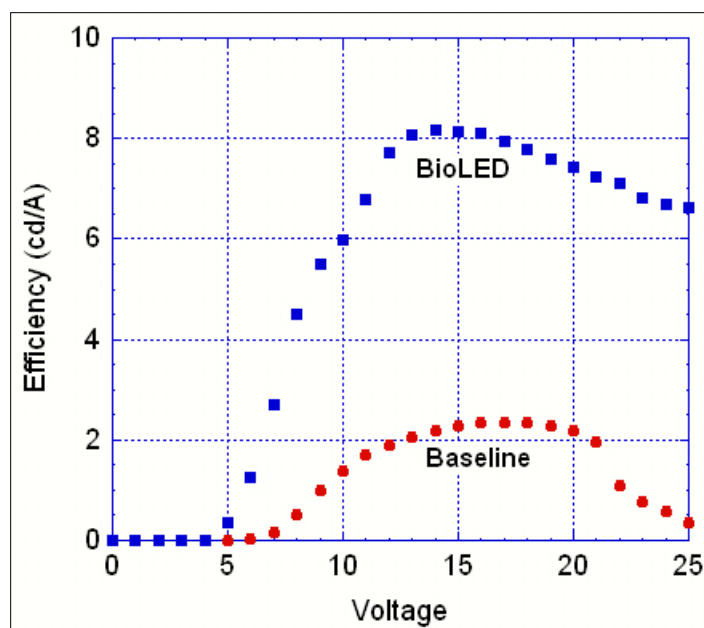


Figure 54. Efficiency versus voltage for green emitting fluorescent type BioLED and Baseline devices

2.3.4 Comparison of DNA-CTMA to other Optoelectronic Polymers

For comparison, OLEDs were fabricated with no EBL ('Baseline' device) and with EBLs using common polymers (PMMA - polymethylmethacrylate or PVK - polyvinyl carbazole).

The energy level diagram previously shown in Figure 48 intuitively shows that DNA-CTMA will act as an EBL in the device. With a DNA LUMO level (Hirata 2004) of 0.9 eV, electrons in the NPB layer will experience an energy barrier of 1.4 eV. The DNA-CTMA HOMO level of 5.6 eV should not inhibit hole transport. Long distance hole transfer has also been reported for DNA in solution⁽¹³⁶⁾. PVK has a LUMO level of 2.3 eV and a HOMO level of 5.8 eV, which does not suggest that the material will effectively block electrons. The PMMA LUMO and HOMO levels are not reported, but the energy gap is estimated at 5.6 eV from the optical absorption of the material. Such a wide energy gap suggests that PMMA could be a charge blocking material. PMMA dissolved in cyclopentanone and PVK dissolved in chlorobenzene were spin deposited to a thickness of ~20nm. The remaining layers were deposited by molecular beam deposition at pressures $\sim 1 \times 10^{-7}$ Torr.

The current density vs. voltage (J-V) curves in forward bias for the green (Alq₃ emitting) OLEDs as a function of EB material are shown in Figure 55. Under reverse bias, a current rectification ratio of $>20\times$ at $\pm 20V$ was measured and no light emission was observed. PVK is a commonly used conductive polymer which acted as a hole transport layer in this device structure as shown by the increase in current as compared to the device with no EB material. Conversely, since PMMA is electrically insulating, the current was greatly reduced when it is used as the EBL material. DNA is reported^(105, 127, 97, Yu 2001) to act as a semiconductor material which accounts for the fact that there was charge transport through the device, but at a lower current than the device without DNA-CTMA. A simple equivalent circuit for the BioLED (DNA EBL) is shown in the insert of Figure 55⁽¹⁰⁹⁾, which isolated the series resistance associated with the DNA layer (R_{DNA}) and the

series resistance ($R_{\text{no-EBL}}$) due to all the other layers as measured in the Baseline (no-EBL) case. By comparing the J-V slope after turn-on for the two devices R_{DNA} of $\sim 300 \Omega$ is calculated. This corresponds to a DNA-CTMA resistivity of $\sim 6 \times 10^6 \Omega\text{-cm}$.

The luminous efficiency of the green (Alq_3) devices with various EBLs is shown as a function of luminance in Figure 56⁽¹⁰⁹⁾. The DNA-CTMA increased the efficiency by a factor of $\sim 2\text{-}10\times$ compared to devices with PVK, PMMA, and no-EB layers.

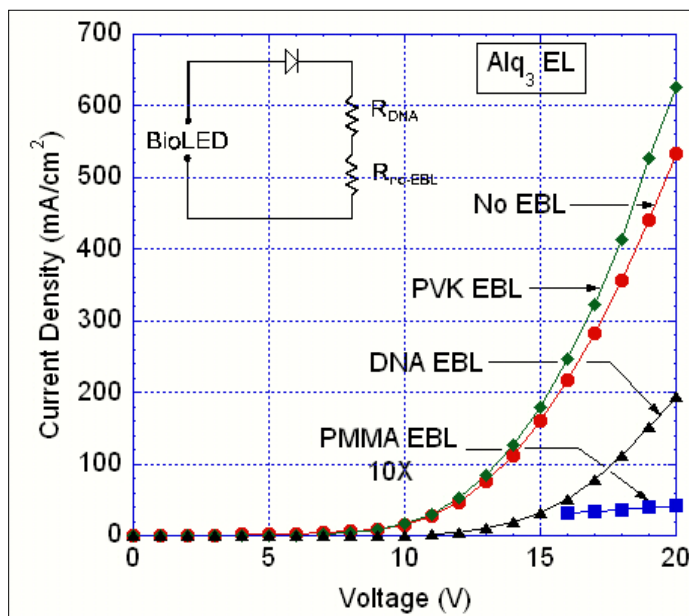


Figure 55. Current density vs. voltage in green Alq_3 LEDs: baseline device, DNA EBL, PVK EBL, PMMA EBL. Inset shows a simple equivalent circuit for the DNA EBL device.

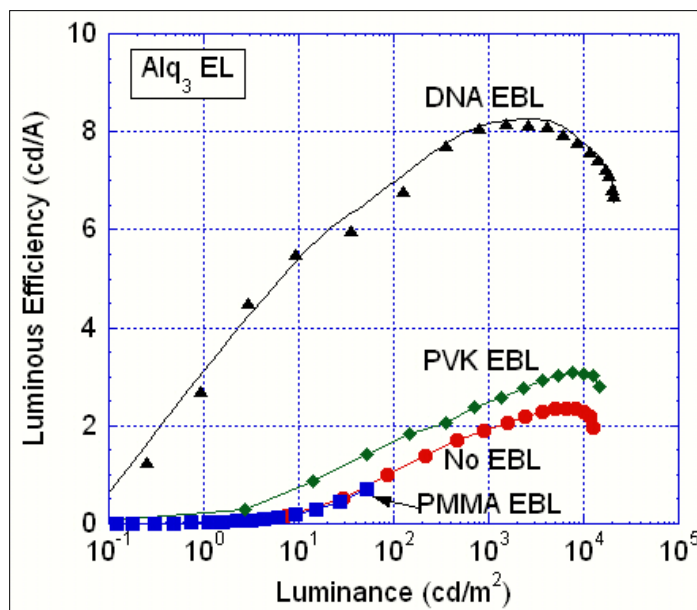


Figure 56. Luminous efficiency vs. luminance in Alq_3 EL devices: baseline device, DNA EBL, PVK EBL, PMMA EBL.

The hypothesis for the performance of the other optoelectronic polymers PMMA and PVK proved to be true in the experiment. PVK, a conductive polymer, allowed more current to run through the device, but the LUMO level of 2.3 did not effectively block electrons thus did not improve device efficiency. PMMA is an electrically insulating material which greatly reduced the current flow in the device. However, it did not effectively block electrons to increase efficiency either, which could be due to the low current flow and/or the actual HOMO and LUMO levels of PMMA. DNA effectively blocks electrons and, because of its low electrical resistivity, does not impede current flow, which makes it unique.

2.3.5 Lifetime of BioLED and Baseline Devices

The efficiency increase of OLEDs using DNA-CTMA as an EBL has been well documented above. This increase should translate into an increase in lifetime of the devices as well, mainly due to the fact that there is a lower current density running through the materials. This theory was tested by analyzing the lifetimes of a BioLED and Baseline device, again grown simultaneously with the common green emitting structure in Figure 47. The devices were set up to operate at an initial brightness of $\sim 100 \text{ cd/m}^2$ with a constant voltage applied. Current and brightness were recorded in 20 minute intervals, and lifetime was defined as the amount of time for the device to decay to 50% of the initial brightness. Since duplicate device testing equipment was not available, the lifetime measurements were done in series. To avoid the impact of any changing conditions, such as humidity, each device was isolated with a plastic cap sealed with a UV curable epoxy in atmospheric conditions. As a conservative approach, the Baseline device was tested first, meaning the BioLED device was exposed to the humid and oxygen rich atmospheric conditions for a longer duration. The lifetime results for the Baseline device are shown in Figure 57 (Hagen 2006). The baseline device had a maximum brightness of 120 cd/m^2 , which was reached very quickly after an increase from 100 cd/m^2 at time = 0. Then the device steadily decayed to the 50% brightness point at ~ 25 hours. Figure 57⁽¹⁰⁹⁾ shows the brightness curves for the BioLED device.

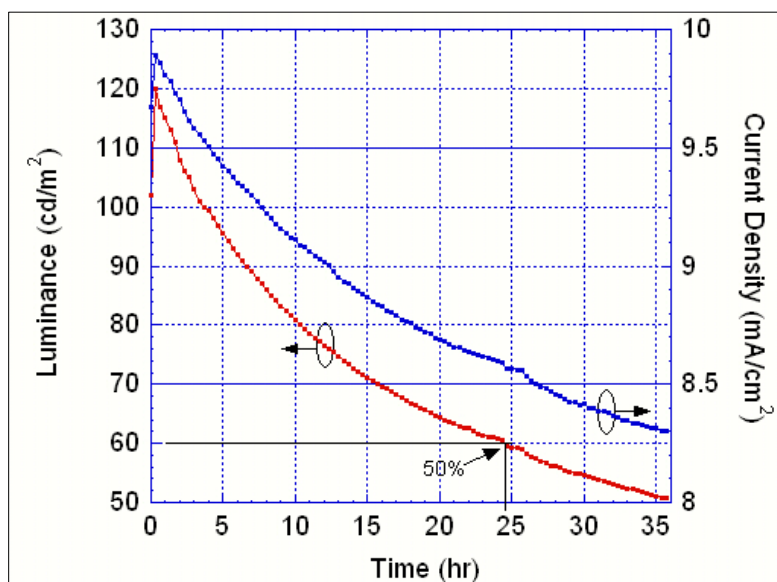


Figure 57. Lifetime curves for Baseline green device: luminance and current density

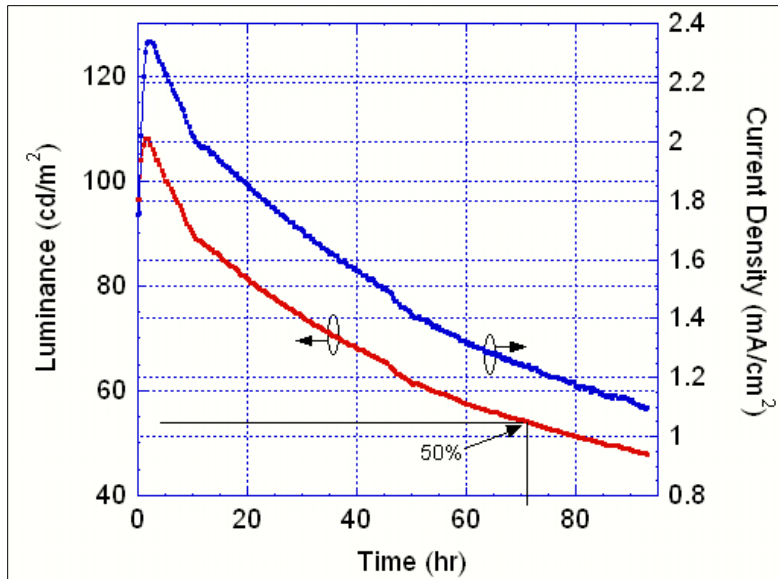


Figure 58. Lifetime curves for BioLED green device: luminance and current density

The BioLED device had an initial brightness of $\sim 110 \text{ cd/m}^2$, which was reached after an initial increase from 100 cd/m^2 at time = 0. The device again steadily decayed to the 50% brightness point, but did not reach this value until ~ 71 hours, which approached a lifetime increase of $3\times$.

The efficiency of both the Baseline and BioLED devices versus time are analyzed in Figure 59⁽¹⁰⁹⁾. The BioLED had an efficiency increase of $\sim 4.5\times$ over the Baseline device, which agreed with the $\sim 3\times$ increase in lifetime, in spite of the additional 48 hours of atmospheric exposure of the BioLED.

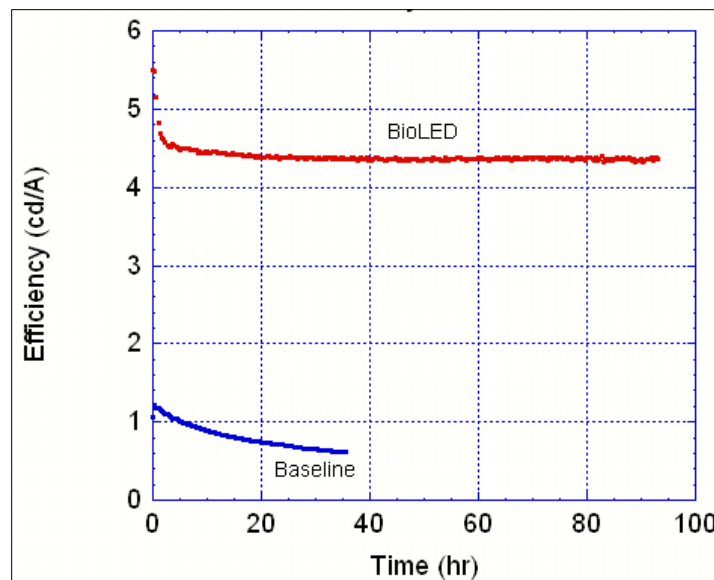


Figure 59. Lifetime efficiency curves: BioLED and Baseline

Phosphorescent Type BioLEDs

Based on the approximate values of the lowest unoccupied Molecular orbital (LUMO) and the highest occupied molecular orbital (HOMO) of the DNA layer and those of adjacent organic layers, we found that a DNA layer acts as a very efficient EBL for fluorescent type OLEDs while not hindering the transport of holes. Therefore, DNA can enhance the probability of exciton formation and eventual photon emission. As stated in the previous sections, the improvement in OLED emission with DNA incorporation has been observed for several fluorescent materials with different HOMO/LUMO levels, including AlQ3 (green emission) and NPB (blue emission). OLEDs that utilize phosphorescent emitting materials can take advantage of excitons in singlet states (which are responsible for light emission in fluorescent materials) and excitons in triplet states. As one might expect from the name “triplet,” there are three times more triplet states available than singlet states. Thus, phosphorescent OLEDs (or PhOLEDs) display much higher brightness and efficiency than fluorescent OLEDs. Recently, we have investigated iridium complexed PhOLEDs that incorporated DNA EBL layers and obtained nearly ideal performance: maximum brightness of nearly 100,000 cd/m² at 13 V (632 mA/cm²); maximum current efficiency of nearly 90 cd/A; and luminous efficiency of 55 lm/W at 5 V (0.11 mA/cm²)⁽¹³⁴⁾. See Figure 60. Assuming Lambertian emission, the measured luminous efficiency converts to approximately 100 percent internal quantum efficiency. This performance is comparable to the best inorganic semiconductor LEDs.

Future prospects

Light-emitting devices based on organic materials clearly have a bright future. Their brightness and efficiency are comparable to their inorganic counterparts. Their Achilles heel has been their limited lifetime, but that has rapidly improved. Because they can be produced in large quantities at reduced cost, OLEDs are accelerating the development of related commercial applications.

Organic materials such as DNA are an attractive possibility for LEDs and many other applications because they are natural, renewable and easily biodegradable. As the photonic and electronic industries strive to become more “green,” these raw materials may play an important role in creating a sustainable future.

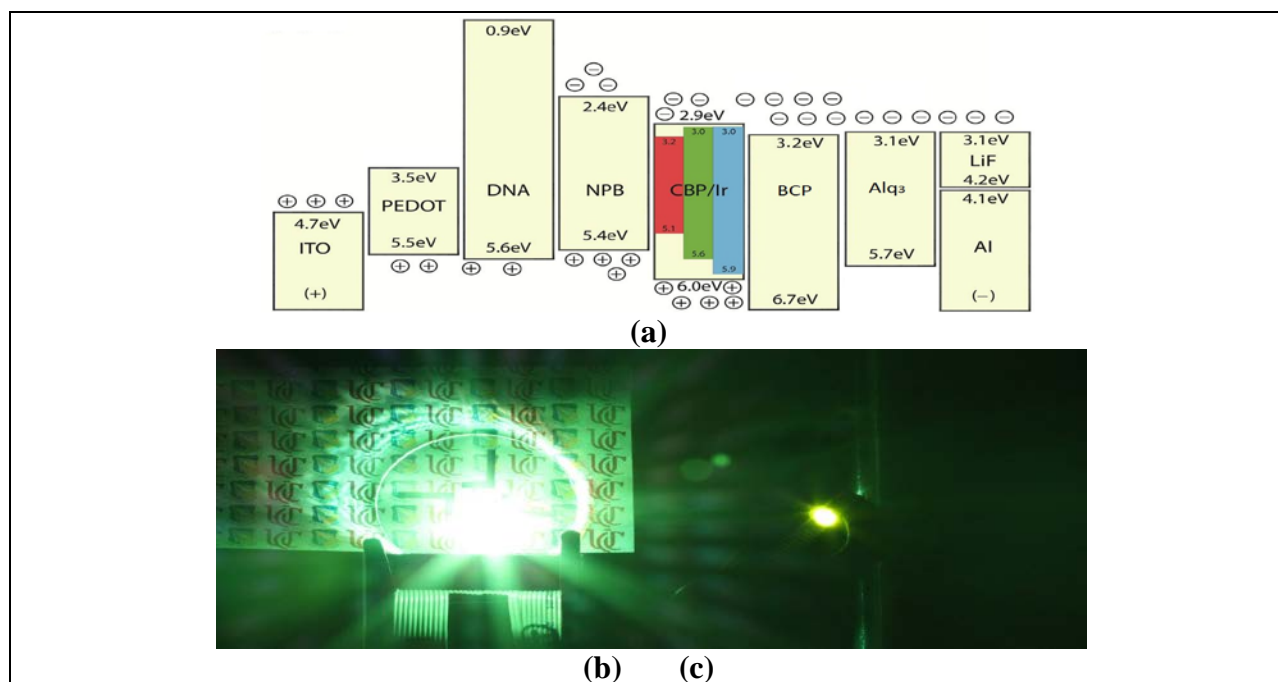


Figure 60. a) Energy level diagram of Iridium complexed emitting BioLED; Photographs of b) Green emitting phosphorescent type BioLED and c) Green emitting inorganic LED in operation

Among biomaterials, DNA, the “molecule of life,” is quite a robust polymer with many useful electronic and photonic properties, including good temperature stability, mechanical robustness and a wide HOMO/LUMO energy gap. In addition, preliminary results indicate that OLEDs that incorporate DNA EBL layers have longer operating lifetimes than devices without DNA. The natural DNA that was used in this effort for device applications is quite abundant and relatively inexpensive. It is also important to search for other natural polymers that can replace the remaining inorganic and synthetic organic materials used in optical devices and to continue to learn about how we can shape the properties of DNA for device use and expand its applications. Perhaps in the future DNA could earn a new nickname: “molecule of light.”

2.4 Conclusions

This chapter describes the first DNA-based thin film modulator, the first FETs using DNA-biopolymers as the semiconducting layer, and the first DNA-containing OLEDs. The results obtained from these devices hold much promise for the future use of DNA-biopolymers in thin film devices. While not all of the results described above are competitive with existing thin film devices, this work lays the groundwork for some exciting future device development using DNA-based thin films.

REFERENCES

- 1 Bartsch, C., Subramanyam, G., Axtell, H., Grote, J., Hopkins, F., Brott, L. and Naik, R., 2007. A New Capacitive Test Structure for Microwave Characterization of Biopolymers “Temperature and Bias Dependant Microwave Dielectric Properties of New Biopolymers”, *Microwave and Optical Technology Letters*, 49(6), pp. 1261-1265
- 2 Cho M. , Lee, U., Kim, Y., Shin, J., Kim, Y., Park, Y., Ju, B., Jin, J. and Choi, D., 2010. Organic Soluble Deoxyribonucleic Acid (DNA) Bearing Carbazole Moieties and Its Blend with Phosphorescent Ir(III) Complexes. *J. Polymer Science Part A-Polymer Chemistry*, 48(9). pp. 1913-1918.
- 3 Grote, J., Heckman, E., Hagen, J., Yaney, P., Diggs, D., Subramanyam, G., Nelson, R., Zetts, J., Zang, D., Singh, B., Sariciftci, N. and Hopkins, F., 2006. DNA- New Class of Polymer. *Proc. SPIE*, 6117: 0J1-0J6.
- 4 Hashim, U., Ehsan, A. and Ahmad, I. 2007. High Purity Polycrystalline Silicon Growth and Characterization, *Chiang Mai J. Sci.*, 34(1). pp. 47-53.
- 5 He, G., Zheng, Q., Prasad, P., Grote, J. Hopkins, F. “Toward Biological Laser: IR Two-Photon Excited Visible Lasing From a DNA-Chromophore-Surfactant Complex”, *Optics Letters*, **31**(3), pp. 359-361, (2006)
- 6 Iqbal, S., Balasundaram, G., Ghosh, S., Bergstrom, D. and Bashir, R., 2005. Direct Current Electrical Characterization of ds-DNA in Nanogap Junctions. *App. Phys. Lett.*, 86: 153901.
- 7 Jin, J-I. and Grote, J., 2012. *Materials Science of DNA*, CRC Press, Taylor and Francis: Boca Raton.
- 8 Kim, S., Kuang, Z., Grote, J., Farmer, B. and Naik, R., 2008. Enrichment of (6,5) Single Wall Carbon Nanotubes Using Genomic DNA, *Nano Letters*, 8(12), pp. 4415-4420.
- 9 Kim, S., Naik, R., Grote, J. and Farmer, B., 2012. Enrichment of Specific Chirality Single Wall Carbon Nonotubes With Genomic DNA, *US Patent*, US 8,273,329 B1.
- 10 Kim, Y., Jung, K., Lee, U., Kim, K., Hoang, M., Jin, J. and Choi, D., 2010. High-Mobility Bio-Organic Field Effect Transistors with Photoreactive DNAs as Gate Insulators, *Appl. Phys. Lett.*, 96(10). 103307.
- 11 Kodama, T. et al., 2009. Heat Conduction Through a DNA-Gold Composite. *Nano Lett.*, 9: p. 2005.
- 12 Krupka, O., El-Ghayoury, A., Rau, I., Sahraoui, B., Grote, J. and Kajzar, F., 2008. NLO Properties of Functionalized DNA Thin Films”, *Thin Solid Films*, 516, pp. 8932-8936.
- 13 Lee, J., Do, E., Lee, U., Cho, M., Kim, K., Jin, J., Shin, D., Choi, S. and Choi, D., 2008. Effect of binding mode on the photoluminescence of CTMA-DNA doped with (E)-2-(2-(4-(diethylamino)styryl)-4H-pyran-4-ylidene)malononitrile, *Polymer*, 49(25), pp. 5417-5423.
- 14 Ner, Y., Grote, J., Stuart, J. and Sotzing, G., 2009. White Luminance from Multi-Dye Doped Electrospun DNA Nanofibers via Fluorescence Resonance Energy Transfer, *Angewandte Chemie*, 48, pp. 1-6.
- 15 Norwood, R., DeRose, C., Himmelhuber, R., Peyghambarian, N., Wang, J., Li, L., Ouchen, F.

- and Grote, J., 2008. Dielectric and Electrical Properties of Sol-Gel/DNA Blends, *Proc. SPIE*, 7403, 74030A
- 16 Samoc, M., Samoc, A. and Grote, J., 2006. Complex Nonlinear Refractive Index of DNA, *Chemical Physics Letters*, 431, pp. 132-134.
- 17 Schuster, G., ed., 2004. DNA Electron Transfer Processes: Some Theoretical Notions. In *Long Range Charge Transfer in DNA II – Topics in Current Chemistry*, 237, p.18, Berlin, Springer Verlag.
- 18 Shockley, W. et al., 1976. The Path to the Conception of the Junction Transistor. *IEEE Trans. Electron Devices*, 23, p. 597.
- 19 Shockley, W., 1949. The Theory of p-n Junctions in Semiconductors and p-n Junction Transistors. *Bell Syst. Tech. J.*, 28, p. 435.
- 20 Singh, B., Sariciftci, S., Grote, J. and Hopkins, F., 2006. Bio Organic-Semiconductor Field-Effect Transistor (BiOFET) Based on Deoxyribonucleic Acid (DNA) Gate Dielectric, *J. Appl. Phys.*, 100, 024514.
- 21 Teal, G. 1976., Single Crystals of Germanium and Silicon-Basic to the Transistor and Integrated Circuit. *IEEE Trans. Electron Devices*, 23, p. 621.
- 22 Warner, R. and Grung, B., 1983. Transistors Fundamentals for the Integrated-Circuit Engineer, Chapter 1. John Wiley & Sons: New York.
- 23 Ahamed, F. and G. Subramanyam 2004. Design of a Si MMIC compatible ferroelectric varactor shunt switch for microwave applications. *Proceedings of the IEEE International Symposium on Applications of Ferroelectrics* 285-288.
- 24 Ausubel, F. et al., eds, 1999. Agarose gel electrophoresis. In *Short Protocols in Molecular Biology Fourth Ed.*, 2.14 – 2.16. New York: John Wiley & Sons, Inc.
- 25 Babcock K. and C. Prater 2004. *Phase imaging: Beyond topography*. Veeco Instruments, Inc., Application Notes.
- 26 Bartsch, C. M. 2007. *Development of a field effect transistor using a DNA-biopolymer as the semiconducting layer*. Ph.D. Dissertation, University of Dayton, Dayton, OH.
- 27 Bartsch, C. M., G. Subramanyam, J. G. Grote, F. K. Hopkins, L. L. Brott, and R. R. Naik. 2007. Dielectric and electrical transport properties of Biopolymers. *Proc. SPIE* 6470: 64700C.
- 28 Bartsch, C. M., G. Subramanyam, J. G. Grote et al. 2007. Bio-organic field effect transistors. *Proc. SPIE* 6646: 66460K.
- 29 Bartsch, C. M., G. Subramanyam, J. G. Grote, F. K. Hopkins, L. L. Brott, and R. R. Naik 2007. A new capacitive test structure for microwave characterization of biopolymers. *Microwave and Optical Technology Letters* 49, 1261.
- 30 Bartsch, C. M., G. Subramanyam, J. G. Grote, F. K. Hopkins, L. L. Brott, and R. R. Naik 2006. Microwave dielectric properties of biopolymers. *Proc. SPIE* 6401: 640107.
- 31 Böttger, H. and V. V. Bryksin 1985. HOPPING CONDUCTION IN SOLIDS. Berlin: Akademie-Verlag.
- 32 Briman, M., N. P. Armitage, E. Helgren et al. 2004. Dipole relaxation losses in DNA.

Nanoletters Lett. 4, 733-736.

33 Cui, P., J. Wu, G-Q Zhang et al. 2008. Hole polarons in poly(G)-poly(C) and poly(A)-poly(T) DNA molecules. *Sci China Ser B-Chem* 51: 1182-1186.

34 Daire, A. 2004. Improving the repeatability of ultra-high resistance and resistivity measurements. *Keithley White Paper*, Keithley Instruments, Inc.: <http://www.keithley.com/support>.

35 Deng, H., V. A. Bloomfield, J. M. Benevides et al. 1999. Dependence of the Raman signature of genomic B-DNA on nucleotide base sequence. *Biopolymers* 50: 656-666.

36 Dutta1, P. and S. K. Mandal 2004. Charge transport in chemically synthesized, DNA-doped polypyrrole. *J. Phys. D: Appl. Phys.* 37: 2908-2913.

37 Eley, D. D. and D. I. Spivey 1962. Semiconductivity of organic substances. *Trans. Faraday Soc.* 58: 411-415.

38 Fink, H.-W. and C. Schönenberger 1999. Electrical conduction through DNA molecules. *Nature* 398: 407-410.

39 Giese, B., J. Amaudrut, A-K. Köhler et al. 2001. Direct observation of hole transfer through DNA by hopping between adenine bases and by tunneling. *Nature* 412: 318-320.

40 Grote, J. G., E. M. Heckman, J. A. Hagen et al. 2006. DNA: new class of polymer. *Proc SPIE* 6117: 61170J.

41 Grote, J. G., E. M. Heckman, D. E. Diggs et al. 2005. DNA-based materials for electro-optic applications: current status. *Proc. SPIE* 5934: 593406.

42 Grote, J. G., E. M. Heckman, J. A. Hagen et al. 2004. Deoxyribonucleic acid (DNA)-based optical materials. *Proc. SPIE* 5621: 16-22.

43 Grote, J. G., J. Hagen, J. Zetts et al. 2004. Investigation of polymers and marine-derived DNA in optoelectronics. *J. Phys. Chem. B* 108: 8584-8591.

44 Grote, J. G., N. Ogata, J. A. Hagen et al. 2003. Deoxyribonucleic acid (DNA)-based nonlinear optics. *Proc. SPIE* 5211: 53-62.

45 Grozema, F. C., L. D. A., Siebbeles, Y. A. Berlin et al. 2002. Hole Mobility in DNA: Effects of Static and Dynamic Structural Fluctuations. *ChemPhysChem* 6: 536-539.

46 Ha, D. H., H. Nham, K-H Yoo et al. 2002. Humidity effects on the conductance of the assembly of DNA molecules. *Chem. Phys. Lett.* 355: 405-409.

47 Hagen, J. A., J. G. Grote, K. M. Singh, R. R. Naik, T. B. Singh, and N. S. Sariciftci 2007. Deoxyribonucleic acid biotronics. *Proc. SPIE* 6470: 64700B-4.

48 Hagen, J., W. Li, A. Steckl, and J. Grote. 2006. Enhanced emission efficiency in organic light-emitting diodes using deoxyribonucleic acid complex as an electron blocking layer. *Appl. Phys. Lett* 88: 171109-1-3.

49 Heckman, E. M. 2006. *The development of an all-DNA-based electro-optic waveguide modulator*. Ph.D. Dissertation, University of Dayton, Dayton, OH.

50 Heckman, E. M., P. P. Yaney, J. G. Grote, and F. K. Hopkins. 2006. Development and

performance of an all-DNA-based electro-optic waveguide modulator. *Proc. SPIE* 6401: 640108.

51 Heckman, E., P. Yaney, J. Grote, F. Hopkins, and M. Tomczak. 2006. Development of an all-DNA-surfactant electro-optic modulator. *Proc. SPIE* 6117: 61170K.

52 Heckman, E. M., J. G. Grote, F. K. Hopkins, and P. P. Yaney. 2006. Performance of an electro-optic waveguide modulator fabricated using a deoxyribonucleic-acid-based biopolymer. *Appl. Phys. Lett.* 89: 181116.

53 Heckman, E., P. Yaney, J. Grote, and F. Hopkins. 2005. Poling and optical studies of DNA NLO waveguides. *Proc. SPIE* 5934: 593408.

54 Heckman, E. M., J. A. Hagen, P. P. Yaney, J. G. Grote, and F. K. Hopkins. 2005. Processing techniques for deoxyribonucleic acid: Biopolymer for photonics applications. *Appl. Phys. Lett.* 87: 211115.

55 Heckman, E. M., J. G. Grote, P. P. Yaney, and F. K. Hopkins. 2004. DNA-based nonlinear photonic materials. *Proc. SPIE* 5516: 47-51.

56 Jin, H-J, J. Park, V. Karageorgiou et al. 2005. Water-stable silk films with reduced β -sheet content. *Adv. Funct. Mater.* 15: 1241-1247; the silk-coated resistivity slides were provided by Fiorenzo Omenetto of Tufts University.

57 Jin, J-I. and Grote, J., 2012. *Materials Science of DNA*, CRC Press, Taylor and Francis: Boca Raton.

58 Kuchel, P. and G. Ralston. 1998. *Schaum's Outline of Theory and Problems of Biochemistry*, McGraw-Hill: New York.

59 Kutnjak, Z., G. Lahajnar, C. Filipic et al. 2005. Electrical conduction in macroscopically oriented deoxyribonucleic and hyaluronic acid samples, *Phys. Rev. E* 71: 041901-1-8.

60 Lakhno, V. D. and N. S. Fialko 2003. Hole mobility in a homogeneous nucleotide chain, *JTEP Lett.* 78: 336-338.

61 Miller, A and B. Abrahams 1960. Impurity conduction at low concentrations. *Phys. Rev.* 120: 745.

62 Okahata, Y., T. Kobayashi, K. Tanaka et al. 1998. Anisotropic electric conductivity in an aligned DNA cast film. *J. Am. Chem. Soc.* 120: 6156-6166.

63 Ortmann, F., K. Hannewald and F. Bechstedt 2009. Charge Transport in Guanine-Based Materials, *J. Phys. Chem.* 113: 7367-7371.

64 Ouchen, F., S. N. Kim, M. Hay et al. 2008. DNA-Conductive polymer blends for applications in Biopolymer based field effect transistors (FETs). *Proc. of SPIE* 7040: 704009-1.

65 Ouchen, F., P. P. Yaney, and J. G. Grote. 2009. DNA thin films as semiconductors for BioFET. *Proc. SPIE* 7403: 74030F.

66 Phillips, D. M., L. F. Drummy, D. G. Conrady et al. 2004. Dissolution and regeneration of bombyx mori silk fibroin using ionic liquids. *J. Am. Chem. Soc.* 126: 14350-14351; solution supplied by Matthew Dickerson and Rajesh Naik of AFRL/RXBN, WPAFB, OH.

67 Porath, D., A. Bezryadin, S. de Vries et al. 2000. Direct Measurement of Electrical Transport Through DNA Molecules. *Nature* 403: 635-637.

- 68 Pozar, D. M. 1998. *Microwave engineering*. New York: Wiley.
- 69 Prater, C., P. Maivald, K. Kjoller, and M. Heaton 2004. *Tappingmode imaging applications and Technology*. Veeco Instruments, Inc., Application Notes.
- 70 Rodger, A. and B. Norden. 1997. DNA-Ligand Interactions. In *Circular Dichroism and Linear Dichroism*, 30-31. New York: Oxford University Press.
- 71 Russell, P., D. Batchelor, and J. T. Thornton 2004. *SEM and AFM: Complementary techniques for high resolution surface investigations*. Veeco Instruments Inc., Application Notes.
- 72 Samoc, A., M. Samoc, J. G. Grote et al. 2006. Optical properties of deoxyribonucleic acid (DNA) polymer host. *Proc. SPIE* 6401: 640106-1-10.
- 73 Seanor, D. A. 1982. *Electrical Properties of Polymers*. Academic Press, Orlando, FL: Chapter 1.
- 74 Serry, F., K. Kjoller, J. Thornton, R. Tench, and D. Cook 2004. *Electric force microscopy, surface potential imaging, and surface electric modification with the atomic force microscope*. Veeco Instruments, Inc., Application Notes.
- 75 Singh 2004. J. Polaron transport mechanism in DNA. *Biomater. Sci. Polymer Edn*, 15: 1533-1544.
- 76 Subramanyam, G., C. M. Bartsch, J. G. Grote et al. 2009. Effect of External Electrical Stimuli on DNA-based biopolymers. *NANO: Brief Reports and Reviews* 4: 69-76.
- 77 Subramanyam, G., E. Heckman, J. Grote et al. 2005. Microwave dielectric properties of marine DNA based polymers. *Microwave and Optical Technology Letters* 46: 278-82.
- 78 Takada, Tadao, K. Kawai, M. Fujitsuka et al. 2006. Rapid long-distance hole transfer through consecutive adenine sequence. *J. Am. Chem. Soc.* 128: 11012-11013.
- 79 Tinoco, I., K. Sauer, J. Wang, and J. Puglisi. 1995. Circular Dichroism of Nucleic Acids and Proteins. In *Physical Chemistry: Principles and Applications in Biological Sciences*, 585-588. Saddle River, NJ: Prentice Hall, Inc.
- 80 Voityuk, A. 2008. Conformations of poly{G}-poly{C} stacks with high hole mobility. *J. Chem. Phys.* 128: 045104-1-6.
- 81 Yaney, P. P., F. Ouchen, and J. G. Grote. 2009. Characterization of polymer, DNA-based, and silk thin film resistivities and of DNA-based films prepared for enhanced electrical conductivity. *Proc. SPIE* 7403: 74030M.
- 82 Yaney, P. P., F. Ahmad, and J. G. Grote. 2008. Raman microprobe spectroscopic studies of solid DNA-CTMA films. *Proc. SPIE* 7040: 70400N.
- 83 Yaney, P. P., E. M. Heckman, and J. G. Grote. 2007. Resistivity and electric-field poling behaviors of DNA-based polymers compared to selected non-DNA polymers. *Proc. SPIE* 6646: 664605.
- 84 Yaney, P. P., E. M. Heckman, A. A. Davis et al. 2006. Characterization of NLO polymer materials for optical waveguide structures. *Proc. SPIE* 6117: 61170W.
- 85 Yoo, K.-H., D. H. Ha, J.-O. Lee et al. 2001. Electrical conduction through poly(dA)-poly(dT) and poly(dG)-poly(dC) DNA molecules. *Phys. Rev Lett.* 87: 198102-1-4.

- 86 Yu, Z. G. and X. Song 2001. Variable range hopping and electrical conductivity along the DNA double helix. *Phys. Rev. Lett.* 86: 6018-6021.
- 87 Yu, Zhou, Yaling Zhou, D. J. Klotzkin et al. 2007. Stimulated emission of sulforhodamine 640 doped DNA distributed feedback (DFB) laser specimens. *Proc. SPIE* 6470: 64700V.
- 88 Zamenhof, S. 1957. Preparation and Assay of Deoxyribonucleic Acid From Animal Tissue. In *Methods in Enzymology*, ed. S. Colowick and N. Kaplan, 696-703. New York: Academic Press.
- 89 Zhang G., L. Wang, J. Yoshida, and N. Ogata. 2001. Optical and Optoelectronic Materials Derived from Biopolymer, Deoxyribonucleic Acid (DNA). *Proc. SPIE* 4580: 337 – 346.
- 90 Zhang G. et al. 2002. Nonlinear Optical Materials Derived from Biopolymer (DNA)-Surfactant-Azo Dye Complex. *Proc. SPIE* 4905: 375–380.
- 91 Adachi, C., Tsutsui, T., Saito, S. 1991. *Optoelectron: Devices Technology* 6: 25.
- 92 Adamovich, V., Brooks, J., Tamayo, A., Alexander, A., Djurovich, P., D'Andrade, B., et al. 2002. High efficiency single dopant white electrophosphorescent light emitting diodes. *New J. Chem* 26: 1171-1178.
- 93 Adamovich, V., Cordero, S., Djurovich, P., Tamayo, A., Thompson, M., D'Andrade, B., et al. 2003. New charge-carrier blocking materials for high efficiency OLEDs. *Organic Electronics* 4: 77-87.
- 94 Ashizawa, S., Y. Shinohara, H. Shindo, Y. Watanabe, and H. Okuzaki. 2005. Polymer FET with a conducting channel. *Synthetic Metals* 153: 41–44.
- 95 Backlund, T. G., H. G. O. Sandberg, R. Osterbacka, H. Stubb, T. Makela, and S. Jussila. 2005. Towards all-polymer field-effect transistors with solution processable materials. *Synthetic Metals* 148: 87–91.
- 96 Bartsch, C. M. 2007. Development of a field-effect transistor using DNA biopolymer as the semiconductor layer. Ph.D Dissertation, University of Dayton.
- 97 Cai, L., Tabata, H., Kawai, T. 2000. Self-assembled DNA networks and their electrical conductivity. *Appl. Phys. Lett.* 77: 3105-3106.
- 98 Covington, J. A., J. W. Gardner, D. Briand, and N. F. de Rooij. 2001. A polymer gate FET sensor array for detecting organic vapours. *Sensors and Actuators B: Chemical* 77: 155–162.
- 99 Covington, J. A., J.W. Gardner, and J. V. Hatfield. 1999. Conducting polymer FET devices for vapor sensing. *Smart Structures and Materials 1999: Smart Electronics and MEMS.* 3673: 296–307.
- 100 Deen, M. J. and M. H. Kazemeini. 2005. Photosensitive polymer thin-film FETs based on poly(3-octylthiophene). *Proceedings of the IEEE* 93: 1312–1320.
- 101 Deen, M.J., M. H. Kazemeini, Y. M. Haddara, et al. 2004. Electrical characterization of polymer-based FETs fabricated by spin-coating poly(3-alkylthiophene)s. *Electron Devices, IEEE Transactions on*, 51: 1892–1901.
- 102 Dimitrakopoulos, C. D. and P. R. L. Malenfant. 2002. Organic thin film transistors for large area Electronics. *Advanced Materials* 14: 99–117.
- 103 Ebisawa, F., T. Kurokawa, and S. Nara. 1983. Electrical properties of

polyacetylene/polysiloxane interface. *Journal of Applied Physics*. 56: 3255-3259.

104 Edman, L., J. Swensen, D. Moses, and A. J. Heeger. 2004. Toward improved and tunable polymer field-effect transistors. *Appl. Phys. Lett* 84: 3744–3746.

105 Fink, H., Schonenberger, C. 1999. Electrical conduction through DNA molecules. *Nature* 398: 407-410.

106 Gao, C., X. Zhu, J.-W. Choi, and C. H. Ahn. 2003. A disposable polymer field effect transistor (FET) for pH measurement. *Solid State Sensors Actuators and Microsystems (Transducers '05), The 12th International Conference on*. 2: 1172–1175.

107 Grote, J., J. Zetts, R. Nelson, et al. 2001. Effect of conductivity and dielectric constant on the modulation voltage for optoelectronic devices based on nonlinear optical polymers. *Optical Engineering* 40: 2464.

108 Gu, J., Kawabe, M., Masuda, K., Namba, S. 1977. Electroluminescence of anthracene with powdered graphite electrodes and ambient gas effects on the electrodes. *J. Appl. Phys.* 48: 2493-2495.

109 Hagen, J. 2006. Enhanced luminous efficiency and brightness using DNA electron blocking layers in bio-organic light emitting diodes. *Ph.D Dissertation, University of Cincinnati*.

110 Hagen, J., Li, W., Steckl, A., Grote, J. 2006. Enhanced emission efficiency in organic light-emitting diodes using deoxyribonucleic acid complex as an electron blocking layer. *Appl. Phys. Lett* 88: 171109.

111 Heckman, E. 2006. The development of an all-DNA-based electro-optic waveguide modulator. *Ph.D Dissertation, University of Dayton*.

112 Heckman, E., P. Yaney, J. Grote, F. Hopkins. 2005. Poling and optical studies of DNA NLO waveguides. *Proc. SPIE* 5934: 593408.

113 Heckman, E., P. Yaney, J. Grote, F. Hopkins, and M. Tomczak. 2006. Development of an All-DNA-surfactant electro-optic modulator. *Proc. SPIE* 6117: 61170K.

114 Heckman, E., Grote, J., Hopkins, F. and Yaney, P. 2006. Performance of an electro-optic waveguide modulator fabricated using a deoxyribonucleic-acid-based biopolymer. *Appl. Phys. Lett.* 89: 181116.

115 Hirata, K., Oyamada, T., Imai, T., Sasabe, H., Adachi, C., Kimura, T. 2004. Electroluminescence as a probe for elucidating electrical conductivity in a deoxyribonucleic acid-cetyltrimethylammonium lipid complex layer. *Appl. Phys. Lett.* 85: 1627-1630.

116 Jin, J-I. and Grote, J. 2012. *Materials Science of DNA*, CRC Press, Taylor and Francis: Boca Raton.

117 Kang, G. W., K. M. Park, J. H. Song, C. H. Lee, and D. H. Hwang. 2005. The electrical characteristics of pentacene-based organic field-effect transistors with polymer gate insulators. *Current Applied Physics* 5: 297–301.

118 Kasumov, A., Kociak, M., Gueron, S., Reulet, B., Volkov, V.T., Klinov D.V., et al. 2001 Proximity-Induced Superconductivity in DNA. *Science* 291: 280-282.

119 Kazanskaya, N., A. Kukhtin, M. Manenkova, N. Reshetilov, L. Yarysheva, O. Arzhakova, A.

- Volynskii, and N. Bakeyev. 1996. FET-based sensors with robust photosensitive polymer membranes for detection of ammonium ions and urea. *Biosensors and Bioelectronics* 11: 253–261.
- 120 Kobayashi, N., Umemura, S., Kusabuka, K., Nakahira, T., Takashi, H. 2001. An organic red-emitting diode with a water-soluble DNA-polyaniline complex containing $\text{Ru}(\text{bpy})_3^{2+}$. *J. Mater. Chem.* 11: 1766-1768.
- 121 Koyama, T., Kawabe, Y., Ogata, N. 2002. Electroluminescence as a probe for electrical and optical properties of deoxyribonucleic acid. *Proc. SPIE* 4464: 248-255.
- 122 Krishna, T. V., J. R. Jessing, D. D. Russell, et al. 2003. Modeling and design of polythiophene gate electrode chemFETs for environmental pollutant sensing. *University/Government/Industry Microelectronics Symposium, Proceedings of the 15th Biennial* 271–274.
- 123 Lee, S. M., S. J. Uhm, J. I. Bang, et al. 2005. A field effect transistor type gas sensor based on polyaniline. *Solid-State Sensors, Actuators and Microsystems (Transducers '05), The 13th International Conference on.* 1935–1938.
- 124 Newman, C. R., C. D. Frisbie, D. A. daSilvaFilho, J. L. Bredas, P. C. Ewbank, and K. R. Mann. 2004. Introduction to organic thin film transistors and design of n-channel organic semiconductors. *Chemistry of Materials* 16: 4436–4451.
- 125 Park, J. H., O. Waldmann, F. C. Hsu, et al. 2003. Fabrication and IV characteristics of PEDOT-PSS based field effect devices and their applications to electric circuits. *American Physical Society Annual Meeting.*
- 126 Peng, X., G. Horowitz, D. Fichou, and F. Garnier. 1990. All organic thin film transistors made of alpha-sexithienyl semiconducting and various polymeric insulating layers. *Applied Physics Letters* 57: 2013-2015.
- 127 Porath, D., Bezryadin, B., de Vries, S., Dekker, C. 2000. Direct measurement of electrical transport through DNA molecules. *Nature* 403: 635-638.
- 128 Rost, H., J. Ficker, J. S. Alonso, L. Leenders, and I. McCulloch. 2004. Air-stable all-polymer field effect transistors with organic electrodes. *Synthetic Metals* 145: 83–85.
- 129 Sakanoue, T., E. Fujiwara, R. Yamada, and H. Tada. 2004. Visible light emission from polymer based field-effect transistors. *Applied Physics Letters* 84: 3037–3039.
- 130 Service, R. 2005. Organic LEDs Look Forward to a Bright, White Future. *Science* 310: 1762-1763.
- 131 Sedra, A. S. and K. C. Smith. 1998. *Microelectronic circuits*. New York: Oxford University Press.
- 132 Singer K.D., M. G. Kuzyk, and J.E. Sohn. 1987. Second-order nonlinear-optical processes in orientationally ordered materials: relationship between molecular and macroscopic properties. *Journal of the Optical Society of America B* 4: 968-976.
- 133 Singh, J. 2001. *Semiconductor devices: basic principles*. New York: Wiley.
- 134 Steckl, A., Spaeth, H., You, H., Gomez, E. and Grote J. 2011. *Optics and Photonics News* 22(7):35-39.

- 135 Swensen, J. S., C. Soci, and A. J. Heeger. 2005. Light emission from an ambipolar semiconducting polymer field-effect transistor. *Applied Physics Letters* 87: 253511–3, 2005.
- 136 Takada, T., Kawai, K., Fujitsuka, M., Majima, T. 2004. Direct observation of hole transfer through double-helical DNA over 100Å. *PNAS* 101: 14002-14006.
- 137 Tang, C., VanSlyke, S. 1987. Organic electroluminescent diodes. *Appl. Phys. Lett.* 51: 913-915.
- 138 Tang, C. VanSlyke, S., Chen, C. 1989. Electroluminescence of doped organic thin films. *J. Appl. Phys.* 65: 3610-3616.
- 139 Teng C. C. and H. T. Man. 1990. Simple reflection technique for measuring the electro-opto coefficient of poled polymers. *Appl. Phys. Lett* 56: 1734.
- 140 Tiwari, S. P., E.B. Namdas, V. Ramgopal Rao, D. Fichou, and S. G. Mhaisalkar. 2007. Solution-processed n-type organic field-effect transistors with high ON/OFF current ratios based on fullerene derivative. *IEEE Electron Device Letters* 28: 880–883.
- 141 Tsumura, A., H. Koezuka, and T. Ando. 1986. Macromolecular electronic device: field effect transistor with a polythiophene thin film. *Applied Physics Letters* 49: 1210-1212.
- 142 Uemura, S., M. Yoshida, S. Hoshino, T. Kodzasa, and T. Kamata. 2003. Investigation for surface modification of polymer as an insulator layer of organic FET. *Thin Solid Films* 438-439: 378–381.
- 143 Wang, W., D. Chen, H. Fetterman, Y. Shi, W. Steier and L. Dalton. 1994. Traveling wave electro-optic phase modulator using cross-linked nonlinear optical polymer. *Applied Physics Letters* 65: 929-931.
- Weimer, P. K. 1962. An evaporated thin film triode. *Proc. IRE-AIEE* 50: 1462.
- 144 Xu, Y. and P. R. Berger. 2004. High electric-field effects on short-channel polythiophene polymer field-effect transistors. *Journal of Applied Physics* 95: 1497-1502.
- 145 Yamamoto, T., T. Yasuda, Y. Sakai, and S. Aramaki. 2005. Ambipolar field-effect transistor (FET) and redox characteristics of a π -conjugated thiophene/1,3,4-thiadiazole CT-type copolymer. *Macromolecular Rapid Communications* 26: 1214–1217.
- 146 Yaney, P., E. Heckman, A. Davis, et al. 2006. Characterization of NLO polymer materials for optical waveguide structures. *Proc. SPIE* 6117: 61170W.
- 147 Yariv, A. and P. Yeh. 1984. *Optical Waves and Crystals*. New York: Wiley.
- 148 Yoshida, M., S. Uemura, T. Kodzasa, T. Kamata, M. Matsuzawa, and T. Kawai. 2003. Surface potential control of an insulator layer for the high performance organic FET. *Synthetic Metals* 137: 967–968.
- 149 Dutta, S. and K. S. Narayan. 2004. Gate-voltage control of optically-induced charges and memory effects in polymer field-effect transistors. *Advanced Materials* 16: 2151–2155.

LIST OF ACRONYMS, ABBREVIATIONS, AND SYMBOLS

<u>Acronym</u>	<u>Definition</u>
DNA	Deoxyribonucleic Acid
NLO	Nonlinear Optics
EO	Electro-Optic
A-T	Adenine-Thymine
G-C	Guanine-Cytosine
PEG	Polyethylene Glycol
CTMA	Hexadecyltrimethyl Ammonium Chloride
PMMA	Polymethylmethacrylate
SWNTs	Single Walled Carbon Nanotubes
CIST	Chitose Institute of Science and Technology
PPIF	poly(phenyl isocyanate)-co-formaldehyde
PEDOT:PSS	poly(3,4-ethylenedioxythiophene) poly(styrenesulfonate)
PTFE	Polytetrafluoroethylene
CD	Circular Dichroism
TGA	Thermogravimetric Analysis
DSC	Differential Scanning Calorimetry
CPW	Coplanar Waveguide
S Parameters	Scattering Parameters
ξ_r	Relative Dielectric Constant
$\tan \delta$	Loss Tangent
AWR	Applied Wave Research's
LRRM	Line-Reflect-Reflect-Match
BST	Barium Strontium Titanate
EFM	Electric Force Microscopy
AFM	Atomic Force Microscopy
APC	Amorphous Polycarbonate
P4VP	Poly 4-vinylphenol
PVP	Poly(vinylpyrrolidone)
DR1	Disperse Red 1
kDa	kilo-Dalton
Si	Silicon
ITO	Indium Tin Oxide
DSC	Differential Scanning Calorimetry
MW	Molecular Weight
FET	Field Effect Transistor

LIST OF ACRONYMS, ABBREVIATIONS, AND SYMBOLS (cont'd)

<u>Acronym</u>	<u>Definition</u>
MISFET	Metal-Insulator-Semiconductor Field Effect Transistor
OFET	Organic Field Effect Transistor
TFT	Thin Film Transistor
PS	Polystyrene
PVA	Polyvinyl Alcohol
PVC	Polyvinyl Chloride
CYEPL	Cyanoethylpulluan
CMOS	Complimentary Metal-Oxide-Semiconductor
BioFET	Biologically-based Field Effect Transistor
P3HT	Poly(3-Hexylthiophene)
OLED	Organic Light Emitting Diode
EBL	Electron-Blocking Layer
Al	Aluminum
LiF	Lithium Fluoride
Alq ₃	tris-(8-hydroxyquinoline) aluminum
HTL	Hole Transport Layer
LUMO	Lowest Unoccupied Molecular Orbital
NPB	N-propyl Bromide
HBL	Hole Blocking Layer
ETL	Electron Transport Layer
MBD	Molecular Beam Deposition
HOMO	Highest Occupied Molecular Orbital
phOLED	Phosphorescent Organic Light Emitting Diode